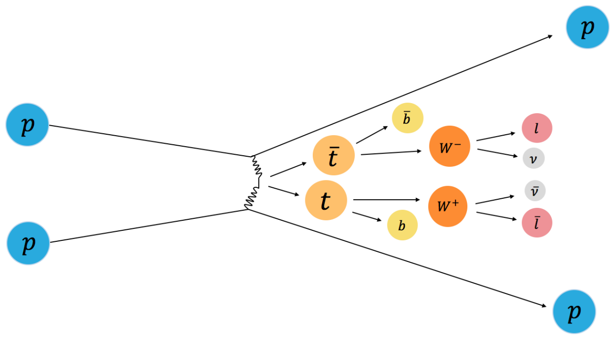

Search for exclusively produced top quark pairs at the LHC

Beatriz Ribeiro Lopes

Thesis to obtain the Master of Science Degree in

Engineering Physics

Supervisor(s): Prof. Michele Gallinaro
Prof. João Manuel Coelho dos Santos Varela

Examination Committee

Chairperson: Prof. Jorge Manuel Rodrigues Crispim Romão
Supervisor: Prof. Michele Gallinaro
Members of the Committee: Dr. Pedro Manuel Vieira de Castro Ferreira da Silva
Dr. Filipe Manuel Almeida Veloso

October 2019

Para a minha mana.

Acknowledgments

First of all, I would like to express my sincere thanks to my supervisors: Michele Gallinaro, for his constant support and enthusiasm, for the enlightening physics discussions and for always pushing me forward and encouraging me to produce new results; and João Varela, for giving me the opportunity to work with the LIP-CMS team and for helping me whenever I needed.

I would also like to thank Pedro Silva for guiding me through the whole journey. Thanks to him, I was able to have a great experience at CERN and to start this analysis. Without his availability, knowledge and dedication, this project would not have been possible.

I also thank Jonathan Jason Hollar, for the never-ending enthusiasm, for always being the first to respond to my emails, for being there at every meeting, and for being my on-call PPS expert.

Working in the LIP-CMS group was a very rewarding experience. I would like to thank everyone in the team for all the useful feedback, and for providing a welcoming work environment. I would also like to thank everyone at LIP for the support, including the LIP secretariat and IT group.

I also feel extremely grateful to all the Master and PhD students at LIP I had the pleasure to have working alongside me. Namely, I want to thank Júlia Silva and Glória de Sá Pereira, for the 5-year adventure. I also want to thank Ana Luísa Carvalho, Diogo Bastos, João Gonçalves, Mariana Araújo, Oleksii Toldaiev and Ricardo Barrué for all the help, friendship, and for making my days at LIP cheerful and fun, even when the deadlines were tight and there was so much to do.

I also thank Giles Strong for taking the time to introduce me to his Neural Networks package, *lumin*, which I regrettably didn't have enough time to include in my thesis work.

I thank the summer student I had the pleasure to supervise, Miguel Guerreiro, for all the insightful questions that helped me understand my work better, as I had to explain it to someone else.

I am grateful to my professors at IST, in particular, the ones from experimental courses, who are in part responsible for sparking my interest in experimental physics. I also feel the need to thank my Physics and Mathematics teachers from high school, Prof. Helena Melo and Prof. Maria do Carmo Pedreiro, for encouraging me and my passion for science.

I want to thank my boyfriend, Dinis, for being an inexhaustible source of love and joy, and for making even the most exhausting day feel bright. Finally, I want to express my profound gratitude to my family, for unconditionally supporting me and my choices.

Resumo

Esta tese foca-se na procura de produção exclusiva de pares de quarks top, no LHC no CERN. Este processo, embora extremamente raro, é previsto pelo Modelo Padrão (MP) da Física de Partículas, e espera-se que seja sensível a acoplamentos anómalos do quark top com o fotão, podendo ser usado na procura de nova física.

A secção eficaz prevista no MP é da ordem de 1fb, o que poderá ultrapassar a atual capacidade de deteção do LHC. No entanto, alguns modelos de extensão do MP preveem que este valor seja superior.

Para a procura, foram utilizados dados colectados em 2017 pelo Compact Muon Solenoid (CMS), incluindo informação colectada pelo Precision Proton Spectrometer (PPS), um detetor de protões situado a 200m do CMS. É feito um estudo da aceitância e desempenho deste detetor. A análise é feita estabelecendo correspondências entre dados centrais do CMS e traços medidos no PPS. Como primeiro passo, fez-se uma seleção com base em cortes em algumas variáveis, tendo sido definidas regiões de controlo e de sinal. Esta definição permitiu estabelecer um limite superior esperado para a secção eficaz do processo em estudo, de $1.1^{+1.1}_{-0.5}$ pb. O limite observado nos dados, para este caso, foi 7.2 pb. A análise é em seguida melhorada utilizando técnicas de Análise Multi-variável, que permite baixar o limite esperado para $0.9^{+0.7}_{-0.4}$ pb, e o observado para 1.4 pb. Trata-se do primeiro resultado experimental de procura de produção exclusiva de pares de quarks top.

Palavras-chave: pares de quarks top, produção exclusiva, CMS, PPS, LHC, Física de partículas

Abstract

This thesis focuses on the search for exclusively produced top quark pairs at the Large Hadron Collider (LHC). This process, although quite rare, is expected to be sensitive to anomalous couplings of the top quark with the photon, and thus can be used to look for new physics. The expected Standard Model cross-section is of the order of 1fb, which might be beyond the current detecting capabilities of the LHC, however some Beyond the Standard Model (BSM) theories predict its enhancement.

For the search, data collected in 2017 by the Compact Muon Solenoid (CMS) are used, including information collected by the Precision Proton Spectrometer (PPS), a forward proton detector located about 200 m from CMS. A study on the acceptance and performance of the latter detector is performed. Data collected in the central CMS detector and tracks recorded by the PPS detector are matched. As a first step, a cut-based selection is performed, and signal and control regions are defined. This approach allowed setting an expected upper limit for the cross-section of this process, of $1.1^{+1.1}_{-0.5}$ pb. The observed limit is 7.2 pb. The search is then improved by using a Multivariate Analysis approach, which brought the expected limit down to $0.9^{+0.7}_{-0.4}$ pb, and the observed cross-section upper limit to 1.4 pb. This is the first experimental result concerning the search for exclusive production of top quark pairs, and the first upper limit set using PPS data.

Keywords: top quark, Central Exclusive Production, CMS, PPS, LHC, Particle Physics

Contents

Acknowledgments . . . iii
Resumo . . . iv
Abstract . . . v
List of Tables . . . viii
List of Figures . . . x
Nomenclature . . . xv
List of Acronyms . . . xv

List of Acronyms **xvi**

1 Motivation and outline **2**

2 Introduction **5**

2.1 The Standard Model of Particle Physics . . . 5

2.1.1 Quarks and leptons . . . 7

2.1.2 Production of top quark pairs . . . 7

2.1.3 Exclusive production . . . 8

2.2 Beyond the Standard Model . . . 9

2.2.1 Anomalous couplings . . . 10

2.3 Objectives . . . 11

3 Experimental considerations **12**

3.1 Collider Physics . . . 12

3.2 The Large Hadron Collider . . . 13

3.2.1 Compact Muon Solenoid . . . 15

3.2.2 Precision Proton Spectrometer (PPS) . . . 17

3.3 Some kinematics definitions in CMS and PPS . . . 20

4 State of the art **22**

4.1 Inclusive $\mathrm{t\bar{t}}$ . . . 22

4.2 Exclusive dileptons . . . 23

5 Analysis Tools **26**
5.1 Data and simulation samples . . . 26
5.1.1 Data samples . . . 26
5.1.2 Simulation samples . . . 27
5.2 Exclusive $t\bar{t}$ analysis . . . 28
5.2.1 Cut-based analysis . . . 30
5.2.2 Multivariate analysis . . . 30
5.2.3 Method employed in the statistical analysis . . . 32

6 Analysis **35**
6.1 Event selection . . . 35
6.1.1 Central detector selection . . . 35
6.1.2 PPS detector selection . . . 40
6.1.3 Matching the central and the forward kinematics . . . 42
6.2 Determination of Roman Pots acceptance . . . 47
6.3 Selection using BDT classifier . . . 49
6.4 Determination of $\sigma(pp \rightarrow t\bar{t}pp)$ through a statistical analysis . . . 51
6.4.1 Cut-based selection . . . 51
6.4.2 BDT-based selection . . . 52
6.4.3 Systematic uncertainties used in the statistical analysis . . . 53

7 Results **55**
7.1 Statistical analysis - Cut-based approach . . . 55
7.2 Statistical analysis - BDT approach . . . 57
7.3 Comparison between methods and discussion . . . 57

8 Conclusions **60**
8.1 Achievements . . . 60
8.2 Future Work . . . 60

Bibliography **62**

A List of triggers used in the analysis **67**

B Extra plots **68**

C PPS optical corrections **71**

List of Tables

5.1 MC samples from the RunIIFall17MiniAODv2-PU2017_12Apr2018_94X_mc2017_realistic_v14 production used in this analysis, and the corresponding process and cross section values. 27

6.1 Yields of expected and observed events, at pre-selection level, as well as after selecting events outside the Z peak region, and after requiring ≥1b-tagged jet. The uncertainties shown for the MC include the statistical uncertainty only. 42

6.2 Yields of expected and observed events outside the Z peak region with ≥1b-tagged jet, after selecting $M_{lb} < 160$ GeV, $H_T = 0$ and $m_{RP} \in [300, 600]$ GeV. The uncertainties shown for the MC include the statistical uncertainty only. 42

6.3 Comparison of the means and standard deviations of the fit to ($y_{t\bar{t}}$ reconstructed - $y_{t\bar{t}}$ generated), before and after using the regression technique, and the improvement obtained. 46

6.4 Comparison of the means and standard deviations of the fit to ($M_{t\bar{t}}$ reconstructed - $M_{t\bar{t}}$ generated)/$M_{t\bar{t}}$ generated, before and after using the regression technique, and the improvement obtained. 47

6.5 RP acceptance: number of events surviving the cut requiring PPS tracks to fall within the RP acceptance, and their corresponding fractions. 49

6.6 Training parameters of the BDT. 49

6.7 Yields for signal and control regions, for different background contributions, for signal and for observed data. The expected yields for signal are normalised to a cross-section of 1 pb. Exactly one track on each side of PPS is required. Only the statistical uncertainty is being represented. 52

6.8 Yields in the signal and control region, for different background contributions, for signal and for observed data, using a cut on the BDT output of 0.2. The expected yields for signal are normalised to a cross-section of 1 pb. Only the statistical uncertainty is being represented. 53

6.9 Systematic uncertainties used in the analysis. 54

7.1 Post-fit nuisances for background-only and signal+background hypotheses (values not compatible with 0 may indicate inconsistencies in the fit). 56

7.2 Post-fit nuisances for background-only and signal+background hypotheses, excluding the DY control region (values not com-patible with 0 may indicate inconsistencies in the fit). . 57

A.1 Triggers used in the selection of the events. 67

List of Figures

2.1 Scheme of the fundamental particles described by the Standard Model, showing the spin, charge and approximate values for the mass of each particle, obtained experimentally. . . 6

2.2 Feynman diagrams for top quark pair production at hadron colliders. 7

2.3 Branching fractions for each of the $t\bar{t}$ decay modes. 8

2.4 Total $t\bar{t}$ production cross-section, measured by several high-energy experiments, and compared with theoretical predictions (from the review on top quark physics in [4]). 8

2.5 Exclusive $t\bar{t}$ production diagrams, via $\gamma\gamma$ fusion (left) and gg fusion (right). 9

2.6 The total cross-section of $pp \rightarrow t\bar{t}pp$ through $\gamma\gamma$ fusion, as a function of the anomalous top quark anomalous moments $\hat{a}_V$ and $\hat{a}_A$. The curves show the sensitivity for different acceptances of the proton detectors (for the PPS detector described in the next section, the red line is the most accurate prediction, from [5]. 10

3.1 Scheme of the Large Hadron Collider, showing the location of different experiments, adapted from [15]. 14

3.2 LHC Project Schedule, including the schedule for the High-Luminosity LHC phase [20]. . 14

3.3 Transverse cut of the CMS detector, depicting the trajectory and detection of different particles, from [22]. 15

3.4 Schematic description of CMS geometry and coordinates. The z-axis corresponds to the beam axis, the y-axis is vertical and pointing upwards, and the x-axis horizontal, perpendicular to the beam and point towards the centre of LHC. Adapted from [22]. . . . 15

3.5 z –R transverse section of the CMS detector. The interaction point is located at (0,0) [24]. 16

3.6 Scheme of one arm of CMS, showing the direction of the ingoing and outgoing beams (red and blue arrows) and the approximate position of the RP stations. Stations labelled ”near” are equipped with silicon strips, while those labelled ”far” have pixel detectors (in 2017). 17

3.7 Drawing of a tracking RP station, from [28]. 18

3.8 Scheme showing the convention used in this thesis in terms of numbering of RP stations. 18

3.9 Efficiency of track reconstruction in PPS as a function of the number of interaction vertices (pileup - <PU>), for the detectors in sector 45, from [30]. For sector 56 the picture is very similar. 19

3.10 Pixel detectors track multiplicity (per event) in 2017 data, for RP stations 023 (left) and 123 (right). . . . 19
3.11 Fractional momentum loss (ξ) of protons reconstructed from RP stations 023 (left) and 123 (right), in 2017 data. . . . 19
3.12 Total integrated luminosity recorded by the CMS and PPS experiments in 2017, from [30]. 20

4.1 Distributions of the number of jets and number of b-tagged jets, for data and simulation, for events passing the selection, with an electron and muon in the final state. . . . 23
4.2 Feynman diagrams for central production of dilepton pairs by $\gamma\gamma$ fusion. Left: none of the protons is dissociated, Center: one proton suffers dissociation and the other is kept intact, Right: both protons are dissociated. . . . 24
4.3 Dimuon (left) and dielectron (right) invariant mass (top) and rapidity (bottom), after all central-detector criteria are applied, in pp collisions at 13 TeV. The ratio between data and all simulated events (simulated signal + background) is shown in the lower panel of each plot. From [35]. . . . 25
4.4 Comparison between the ξ obtained in the central system, for selected events, and the ξ from the RPs tracks, for both arms of PPS, from [35]. . . . 25

5.1 Feynman diagram of the exclusive $\mathrm{t\bar{t}}$ dilepton channel. . . . 28
5.2 Feynman diagram for Drell-Yan production. . . . 29
5.3 Simulated distributions of the transverse momentum of the $\mathrm{t\bar{t}}$ pairs for elastic-elastic, inelastic-elastic (elastic-inelastic) and inelastic-inelastic contributions to the exclusive $\mathrm{t\bar{t}}$process, from [8]. The "LUX-like" label in the picture refers to the LUX framework, that models the photon content inside the proton, and was used to compute these distributions [46]. . . . 30
5.4 Scheme showing the structure of a BDT. The variables x_i are then used to perform the cuts. . . . 31
5.5 Scheme depicting the concept of overtraining. On the left, a seemingly reasonable cut is applied on a 2-d distribution to separate signal and background. On the right, the cut which is applied reflects the specific characteristics of the dataset, and is unlikely to perform well when applied to a different one (overtraining). . . . 32

6.1 Left: Comparison between the M_{lb} calculated using the minimum mass value (x axis) and using the minimum $\Delta R(l, b)$ (y axis). Right: Events for which both methods yield the same resut. . . . 36
6.2 Distribution of the invariant mass of the dilepton system after selecting 2 leptons. Top left: ee, top right: $\mu\mu$, bottom centre: $e\mu$ channel. . . . 37
6.3 Distribution of the invariant mass of the dilepton system after selecting 2 leptons and ≥1 b and requiring $M_{lb} < 160$ GeV, for the $e\mu$ channel. The signal is normalised to a cross-section of 1 fb and multiplied by 1000, to make it visible in the distribution. . . . 37

6.4 Distribution of the number of b-tagged jets after selecting 2 leptons. Top left: ee, top right: $\mu\mu$, bottom centre: $e\mu$ channel. The signal is normalised to a cross-section of 1 fb and multiplied by 1000, to make it visible in the distribution. 38
6.5 Hadronic activity distributions obtained after requiring 2 leptons, 1 jet, 1 b-jet, M_{lb} <160 GeV and opposite flavour leptons. The hadronic recoil h (left) and H_T (right) are shown. The signal is normalised to a cross-section of 1 fb and multiplied by 1000, to make it visible in the distributions. 39
6.6 Distribution of the ΔR between the two leptons, after selecting 2 leptons and ≥1 b and requiring $M_{lb} < 160$ GeV, for the $e\mu$ channel. The signal is normalised to a cross-section of 1 fb and multiplied by 1000, to make it visible in the distribution. 39
6.7 Distribution of the fractional momentum loss (ξ) of the protons detected in the pixels, for RP023 (left) and RP123 (right), for data and signal simulation. The orange lines represent the fiducial cuts due to detector acceptance. 40
6.8 Distribution of the reconstructed mass (left) and rapidity (right) of the two-proton system in the RPs, when requiring 2 leptons of opposite flavour, 1 jet, 1 b-jet, low mass of the lepton/b-jet system, and 1 track on each side of PPS. 41
6.9 Scheme showing the procedure for computing the fake rate. For a given number of simulated events, one generates a random number of tracks in each arm of PPS, according to the data distributions. Then, for each track, a random ξ value is generated (also according to the probability of the distributions). The pp mass (M_{RP}) is then reconstructed from the two random tracks in the two opposite PPS arms, and the fraction of times that it falls within the [300,600] GeV range yields the fake rate. 43
6.10 Distributions of the invariant mass of the $\mathrm{t\bar{t}}$ pair at generator level versus the one reconstructed by the algorithm were produced for ee (top left), $\mu\mu$ (top right) and $e\mu$ (bottom left) samples. On the bottom right plot, the difference between the generated and reconstructed mass is shown, for all channels together. A Gaussian function is fitted, and a resolution of 15.5 ± 0.5% is obtained. 44
6.11 Distributions of the rapidity of the $\mathrm{t\bar{t}}$ pair at generator level versus the one reconstructed by the algorithm were produced for ee (top left), $\mu\mu$ (top right) and $e\mu$ (bottom left) samples. On the bottom right plot, the difference between the generated and reconstructed rapidity is shown, for all channels together. A Gaussian function is fitted and a standard deviation of 0.228 ± 0.006 is obtained. 45
6.12 Resolution of the mass (left) and rapidity (right) reconstruction - blue: using the algorithm, red: using the algorithm + regression technique 46
6.13 Comparison of the $M_{\mathrm{t\bar{t}}}$ (top) and $y_{\mathrm{t\bar{t}}}$ (bottom) centrally reconstructed and those measured by PPS, for simulated signal events: before regression (left) and after regression (right). . 47
6.14 2D distributions of the mass (m_{RP}) versus rapidity (y_{RP}) of the $\mathrm{t\bar{t}}$ system in the signal sample, for the $e\mu$ final state (results are similar for other final states) after requiring 2 leptons (top), and after requiring also that the tracks are within the RP acceptance (bottom). 48

6.15 Correlation matrices, showing the linear correlation coefficient between all pairs of variables, for signal and background (see text). The correlation coefficients are shown in percentage, from -100 to 100, where 0 means no observed correlation, 100 means fully correlated and -100 means fully anti-correlated. 50
6.16 Comparison between training and test samples, in terms of the response of the BDT classifier, in order to check for agreement between samples and evaluate if there was overtraining. The training and testing are done using the simulated signal and $t\bar{t}$ background samples. The disagreements found in the signal samples are caused by the very low statistics. 51
6.17 Output of the BDT classifier, when applied to the full data and MC samples (all decay channels, ee, $e\mu$ and $\mu\mu$, together). One can observe the separation between signal and background works as expected, with signal events clustering at larger BDT output values and background events in lower BDT output values. The signal is normalised to a cross-section of 1 fb and multiplied by 1000, to make it visible in the distribution. 52
6.18 Ratio of expected $S/\sqrt{B}$ in the SR as a function of the applied cut in the BDT output. The expected signal yields are normalised to a cross-section of 1 pb. 53

7.1 (a) Contour of the likelihood for the scale factor for inclusive $t\bar{t}$ and DY processes which are fit using the dedicated control regions. The point marks the fitted values. (b) Likelihood scan results for the signal at expectation level for a $\sigma = 1.1$ pb scenario. The lines intersect the likelihood at the boundaries of the 68% and 95% confidence intervals (CI). 56
7.2 (a) Contour of the likelihood for the scale factor for inclusive $t\bar{t}$ and DY processes. The point marks the fitted values. (b) Likelihood scan results for the signal at expectation level for a $\sigma = 1.1$ pb scenario, excluding the DY control region. The lines intersect the likelihood at the boundaries of the 68% and 95% CI. 57
7.3 (a) Contour of the likelihood for the scale factor for inclusive $t\bar{t}$ and DY processes. The point marks the fitted values. (b) Likelihood scan results for the signal at expectation level for a $\sigma = 0.8$ pb scenario, excluding the DY control region. The line intersects the likelihood at the boundaries of the 68% CI. 58
7.4 Statistical and systematic uncertainties in the measurement of $M_{t\bar{t}}$, from [61], as a function of the value of $M_{t\bar{t}}$. 59

B.1 Distribution of the number of light (not b-tagged) jets (left) and the missing transverse energy (right), after selecting 2 leptons and ≥1 b and requiring $M_{lb} < 160$ GeV, for the $e\mu$ channel. 69
B.2 Distribution of the M_{lb} (mass of one of the lepton b-jet associations), after selecting 2 leptons and ≥1 b and requiring $M_{lb} < 160$ GeV, for the $e\mu$ channel. 69
B.3 Distributions for signal (blue) and background (red), of the 13 variables which were found to most discriminating between signal and inclusive $t\bar{t}$ background, for the training sample used in the BDT classifier. 70

C.1 Plots showing the difference between the ξ values before and after applying the most recent optical corrections, for the different IHC crossing angles considered. ”45” refers to LHC sector 45, or the negative arm as it is described in this thesis, while ”56” refers to sector 56 or the positive arm. 71

C.2 Distribution of the pp mass as reconstructed from PPS tracks, in data, before (black) and after (red) applying the optical corrections. The light blue area shows the exclusive $t\bar{t}$ region chosen for the analysis. It is visible that the number of events within this region is increased by 60% when moving to the new alignments. This is a large difference, and that is why the whole analysis was rerun to include the corrections. 72

List of Acronyms

BDT Boosted Decision Trees.

BSM Beyond the Standard Model.

CEP Central Exclusive Production.

CERN European Organization for Nuclear Research.

CMS Compact Muon Solenoid, LHC experiment.

CP Charge-parity.

DY Drell-Yan process.

EDM Electric dipole moment.

EFT Effective Field Theory.

FOM Figure of Merit.

K-S Kolmogorov-Smirnov Test.

HLT High Level Trigger.

LHC Large Hadron Collider.

LO Leading order.

MDM Magnetic dipole moment.

NNL Next-to-next-to-leading order.

NP New Physics.

PPS Precision Proton Spectrometer, a CMS forward detector.

QCD Quantum Chromodynamics.

QED Quantum Electrodynamics.

RP Roman Pot, movable near-beam devices that contain the detectors from PPS.

SM Standard Model of Particle Physics.

TMVA ROOT’s Toolkit for Multivariate Analysis.

TOTEM TOTal cross section, Elastic scattering and diffraction dissociation Measurement at the LHC.

> “ *[Science] must be done for itself, for the beauty of science, and then there is always the chance that a scientific discovery may become like the radium, a benefit for humanity.* ”

Marie Curie

Chapter 1

Motivation and outline

Science moves forward when people ask the right questions, the most fundamental ones. One of these fundamental questions has been, and still is, ”what is everything made of?”. Coming up with answers for this question is precisely the focus of Particle Physics. Remarkable progress has been made in this field in the past century, both in the theoretical and experimental fronts, which lead to the development and testing of a rather successful theory, called the Standard Model (SM) of Particle Physics.

This model describes a set of fundamental particles and their interactions, and is capable of making predictions that can be experimentally tested. Since 2012, all particles predicted by the SM have been observed, but physicists are aware that this is not the final answer.

The SM does not provide a suitable candidate for Dark Matter, which is known to exist from astronomical measurements. It also fails to explain other phenomena, such as the matter-antimatter asymmetry present in our universe and the origin of neutrino masses. It is also not clear how it can accommodate General Relativity, the theory of gravitation. Hence, the effort on the theoretical side has been to develop mathematically consistent models that may work as possible extensions of the SM, and which would be able to solve the existing problems.

On the experimental side, there are two main approaches. The first is to make precision measurements of processes involving SM particles. If deviations from the predictions are observed with enough significance, they can provide strong hints for the presence of New Physics (NP). Precision measurements are also important to help exclude some Beyond the Standard Model (BSM) scenarios. In order to achieve higher precision, higher statistics is required. The second approach is to directly search for NP particles being produced in particle collisions, by looking for a resonant production, that would show as an accumulation of events at a well defined mass value. This approach requires access to higher energies.

The SM includes matter particles, called fermions, and force mediators for the strong, weak and electromagnetic interactions, called gauge bosons. It also includes the Higgs boson, which appears in the model as a consequence of a mechanism (the Higgs mechanism) that attributes mass to some of the particles. The matter particles include six types (called flavours) of quarks: up, down, charm, strange, top and bottom. The up and down quarks make up the protons and neutrons that constitute the matter we see. The top quark, discovered in 1995, is the heaviest known particle, and the measurement of its properties is still ongoing. It is nowadays considered one of the most promising ways to look for BSM physics, since the Large Hadron Collider (LHC), at CERN, has been providing large samples of top quark events, and so there is now the chance to perform a variety of precision measurements that were not possible before. An example of precision measurements is probing the couplings between the top and other SM particles, which are predicted to be small, and deviations from the predictions are hints to NP.

The goal of this thesis is to perform a physics analysis to search for the production of pairs of top quarks, as the result of the interaction of high-energy photons. This production is expected to occur with low probability when colliding protons at the energies achieved at the LHC.

I will focus on data collected by the Compact Muon Solenoid (CMS) at the LHC in 2017. The exact process I will be looking for is the one in which two protons collide, exchanging high-energy photons that produce a top anti-top quark pair, and stay intact, i.e., $\mathrm{pp} \rightarrow \mathrm{t\bar{t}pp}$. Since the occurrence of this process can be very precisely modelled theoretically, and no observation of it has been reported yet, deviations from the predictions can be strong hints of New Physics. Additionally, the process is expected to be sensitive to possible anomalous couplings between the photon and the top quark, that is, to the possibility that the strength of the interaction between these particles is not merely the one predicted by the SM but has other contributions.

For the analysis, I will take advantage of a recently installed detector, the Precision Proton Spectrometer (PPS), which was designed to detect protons that remain intact after the collisions at CMS. The main objectives of this work are to develop an analysis which reveals whether CMS (and the LHC) has enough sensitivity to detect this process, and set quantitative limits on its production.

In chapter 2, I present an introduction to Particle Physics and the Standard Model. I focus on the production of top quark pairs, and discuss the concept of exclusive production and its potential in the search for BSM physics. In the third chapter, I introduce the physics behind Particle Colliders, and describe the LHC, CMS and PPS experiments. In the fourth chapter, the state of the art is discussed. Previous measurements on top quark pair production are presented and interpreted. The first physics result using PPS is also presented, and the methods used in the analysis are described, since they served as a starting point for my work.

In the fifth chapter, I present and motivate the tools used in the analysis. Namely, I list the data and simulation samples which were used, and I present the computational and mathematical tools that were necessary for the analysis. The sixth chapter describes the analysis process itself, step-by-step, including event selection, plots for the most relevant distributions, background determination and considerations on detector acceptance.

In the seventh chapter, the results of the statistical analysis are shown. The results obtained through a cut-based analysis are presented first. Sequentially, the results for a Multivariate Analysis (MVA) approach approach are shown, and a comparison between the two is drawn. Limits are set on the cross-section of the signal process, for both approaches.

In the last chapter, I summarise my work, presenting the most relevant achievements and conclusions, and leave some notes on future approaches that can be pursued regarding this search.

Chapter 2

Introduction

The Standard Model (SM) of Particle Physics describes all the known fundamental particles, as well as their interactions. In section 2.1, an overview of the theory is presented. A special focus is given to the top quark, its production and decay modes. In section 2.1.3, the concept of exclusive production is discussed from a theoretical viewpoint. Finally, I present some beyond the SM considerations, in particular the concept of anomalous couplings and how this process can be sensitive to them. I list the objectives of this thesis work in the last section of this chapter.

2.1 The Standard Model of Particle Physics

The Standard Model (SM) is one of the most successful physics theories ever built, being the product of decades of theoretical and experimental work, starting in the last half of the twentieth century.

It is a quantum field theory, which means it lies on the concept of quantum fields that permeate the entire Universe. The so-called fundamental particles then appear as excitations of these quantum fields.

The known fundamental particles are schematically described in figure 2.1, which shows for each particle a set of properties (essentially mass, spin and electric charge).

As shown in the figure, the particles can be divided into matter particles, or fermions, and gauge bosons. In the first group, particles have half-integer spin and are known as quarks and leptons. The gauge bosons have integer spin and mediate three of the four known fundamental interactions: the gluon mediates the strong force - described by Quantum Chromodynamics (QCD), the photon mediates the electromagnetic interaction, and the W and Z bosons mediate the weak force. The latter two forces are often grouped in one interaction, known as the electroweak (EW) force, described by Quantum Electrodynamics (QED).

Additionally, the theory includes one scalar (spin 0) boson, known as the Higgs boson, predicted in 1964 and discovered experimentally in 2012 by both ATLAS and CMS collaborations at the Large Hadron Collider, CERN [1, 2]. This boson interacts with all the particles that have mass and is responsible for this mass, through a process called the Higgs mechanism.

These fields and interactions between them can be better understood using the Lagrangian formal-

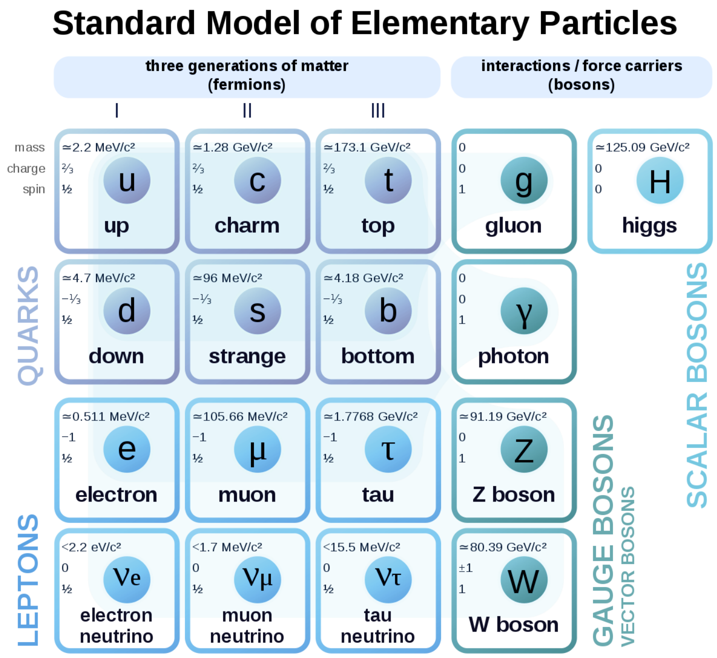

Figure 2.1: Scheme of the fundamental particles described by the Standard Model, showing the spin, charge and approximate values for the mass of each particle, obtained experimentally.

ism. The SM Lagrangian ($\mathcal{L}_{SM}$) includes the following terms:

$$\mathcal{L}_{SM} = -\frac{1}{4}G^k_{\mu\nu}G_k^{\mu\nu} - \frac{1}{4}W^a_{\mu\nu}W_a^{\mu\nu} - \frac{1}{4}B_{\mu\nu}B^{\mu\nu} + i\bar{\psi}\not{D}\psi + \bar{\psi}_{L_i}y_{ij}\psi_{R_j}\phi + |D_\mu\phi|^2 - V(\phi) \tag{2.1}$$

where $G^k_{\mu\nu}$ denotes the SU(3)$_C$ field-strength tensor, $W^a_{\mu\nu}$ the SU(2)$_L$ field strength tensor, and $B_{\mu\nu}$ the corresponding U(1)$_Y$ tensor. The gauge bosons corresponding to these tensors are, respectively, G^k_μ, W^a_μ and B_μ. The first three terms of the Lagrangian describe the self-interactions of these gauge bosons. The names SU(3), SU(2) and U(1) refer to symmetry groups, and the subscript C denotes colour (the property that governs the strong interaction), L refers to the left weak isospin and Y is the hypercharge. We say that the SM is ruled by the SU(3)$_C$ × SU(2)$_L$ × U(1)$_Y$ gauge theory.

The fourth term of the Lagrangian includes both the propagation of fermion fields ψ and their interactions with gauge bosons. The term can be expanded using the definition $\not{D} = \gamma^\mu D_\mu$, where

$$D_\mu = \partial_\mu - ig_s t_k G^k_\mu - igT_a W^a_\mu - ig'\frac{Y}{2}B_\mu \tag{2.2}$$

The g_s, g and g' are the coupling constants which quantify the strength of the interactions, for SU(3)$_C$, SU(2)$_L$ and U(1)$_Y$, respectively.

The last three terms in the Lagrangian are related to interactions of the Higgs boson with other particles, which are beyond the scope of this thesis.

2.1.1 Quarks and leptons

The fermions are divided into quarks and leptons. Leptons are organised in three families - electrons, muons and taus. These particles interact electromagnetically and weakly, but not through the strong force, since they do not carry a colour quantum number. For each of these leptons, there is a corresponding neutrino, which interacts only weakly.

The quarks, however, carry colour, and interact through all three of these fundamental forces. There are six types of quarks, with large mass differences between them, and we call these types flavours.

The term concerning the coupling between each quark and the photon, which will be needed in section 2.1.3, is:

$$\mathcal{L}_{photon-q} = -g' Q_q \bar{\psi_q} \gamma^{\mu} \psi_q A_{\mu} \tag{2.3}$$

where Q_q denotes the electric charge of the quark, and A_{μ} the photon field.

2.1.2 Production of top quark pairs

Being the heaviest of SM particles, and the second last to be discovered, in 1995 [3], the top quark is of special interest, for being potentially more sensitive to deviations from the SM. It has an electric charge $+\frac{2}{3}$e and a mass $m_{top} = 173.0 \pm 0.4$ GeV [4], nearly in the same order of the electroweak symmetry breaking energy scale.

At hadron colliders, quarks are produced mainly in the form of high-energy quark anti-quark ($q\bar{q}$) pairs, where the quark and anti-quark each produce a shower of quarks and gluons, which then combine into hadrons (colour singlet states of quarks and gluons), through a process called hadronisation. These hadrons form within a short spatial distance around the initial quark, that can be reconstructed in what is called a "jet". However, this is not the case for the top quark that, due to the very short lifetime, decays before hadronization can occur. The top quark is also produced mainly in $t\bar{t}$ pairs, through the processes in figure 2.2, but being heavier than the W boson, it is the only quark that decays semi-weakly, into a real W boson and a b quark.

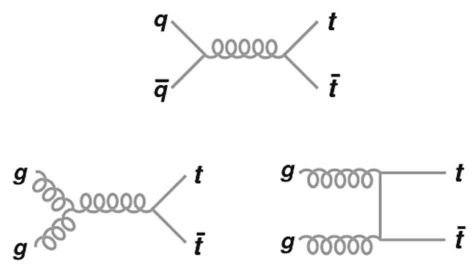

Figure 2.2: Feynman diagrams for top quark pair production at hadron colliders.

The decay process mentioned above (t→Wb) happens almost exclusively in the SM (branching ratio > 99% [4]). The $t\bar{t}$ decay channels are then labelled according to how the W bosons decay: the *all-jets channel* (when both W bosons decay to $q\bar{q}$ pairs which then hadronise), the *lepton+jets* channel (when

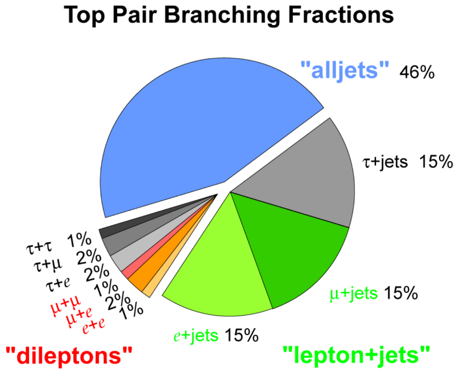

Figure 2.3: Branching fractions for each of the $t\bar{t}$ decay modes.

one W decays to a $q\bar{q}$ pair and the other to a lepton and the corresponding neutrino) and the *dilepton* channel (when both W bosons decay each into a lepton and the corresponding neutrino). The branching fractions for these decay channels are illustrated in figure 2.3.

The production cross-section of top quark pairs, as a function of the center-of-mass energy ($\sqrt{s}$), is shown in figure 2.4. The points show the cross-section measurements done over the years by several different experiments, compared with the theoretical predictions for proton-proton and proton-antiproton collisions.

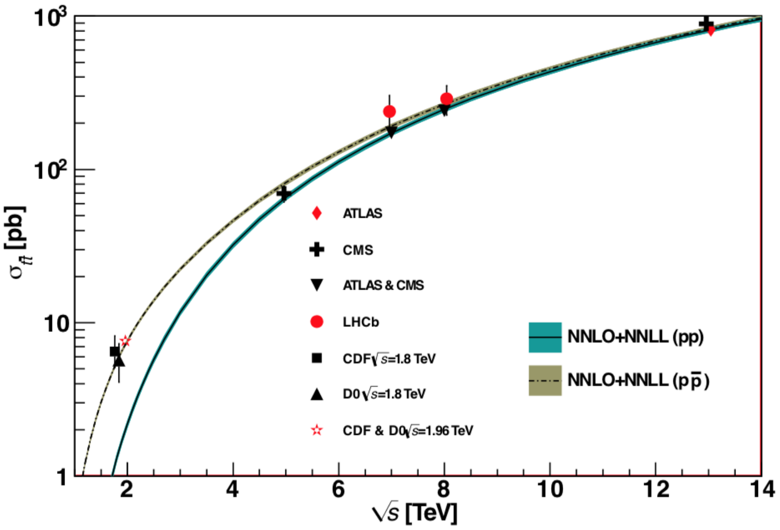

Figure 2.4: Total $t\bar{t}$ production cross-section, measured by several high-energy experiments, and compared with theoretical predictions (from the review on top quark physics in [4]).

2.1.3 Exclusive production

In a proton-proton collision, some of the quarks and gluons from one of the protons will interact with those from the other proton at high-energy, causing, in general, the disruption of the initial protons. In some collisions, however, these protons may exchange either energetic gluons or photons, which combine producing new particles, while either one or both of the initial protons are kept intact. We call these exclusive processes (or semi-exclusive, in case only one of the protons remains intact).

This kind of process is rare but extremely interesting if one can have experimental access to the energy of the escaping proton(s). That is the case at the CMS experiment in the LHC, with the Precision Proton Spectrometer described in the next section. Such collisions provide very clean experimental signals and are a very promising way to search for a possible BSM signal [5].

In this work, we are interested in the central exclusive production (CEP) of top quark pairs by either photon or gluon fusion, as shown in figure 2.5. The SM prediction for the cross-section (quantum mechanical measure of the probability of occurrence) is extremely low, $\mathcal{O}(1\ \mathrm{fb})$ for photo-production [6, 7], but if identified in data it offers the possibility of determining the $\mathrm{t\bar{t}}$ production threshold with a better resolution than that which can be achieved based on the reconstruction of the final states of the decay [8].

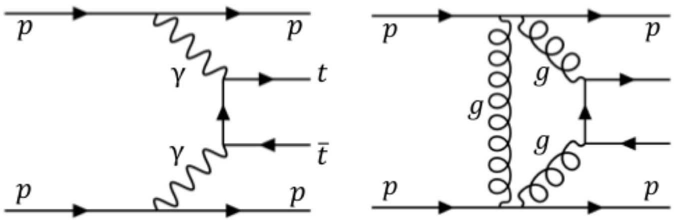

Figure 2.5: Exclusive $\mathrm{t\bar{t}}$ production diagrams, via $\gamma\gamma$ fusion (left) and gg fusion (right).

Besides, if new physics is present, the low cross-section could be significantly enhanced, either in the production of $\mathrm{t\bar{t}}$ (due to couplings of the top quark with BSM particles) or in the production of similar final states containing at least two leptons [9–12].

A reason why this search is interesting is that this process is expected to be very sensitive to top anomalous couplings (couplings which are expected to be null in the SM). Unlike other quarks, most of the top quark couplings are not yet thoroughly studied, and SM predictions still have to be tested more.

2.2 Beyond the Standard Model

The SM, although successful, is known not to be the full picture. There is evidence from astronomical measurements for the existence of an additional type of weakly-interacting matter - dark matter, and the SM does not provide a suitable candidate for this. Moreover, it does not incorporate General Relativity, therefore not describing the gravitational interaction. There is also a strong possibility that the CP violation (violation of charge-parity symmetry) in the SM is insufficient to explain the observed matter-antimatter asymmetry of the Universe. The theory also fails to explain the origin of neutrino masses. These loose ends of the theory motivate new theoretical models and experimental searches for BSM physics [13].

There are two main experimental approaches when looking for BSM physics. One is to start with a theoretical model and perform a direct search for the BSM particles predicted by this model, e.g. Supersymmetry, also called SUSY. The other is searching for deviations from the SM in data, which can point to where the scale of new physics is, e.g. anomalous couplings or Effective Field Theory (EFT).

2.2.1 Anomalous couplings

In [5], Fayazbakhs et al. investigate the possibility of exploring the top quark electric and magnetic moments through $\mathrm{pp} \rightarrow \mathrm{p}\gamma\gamma\mathrm{p} \rightarrow \mathrm{pt\bar{t}p}$ production at the LHC. They perform analytic calculations and a numerical analysis on the sensitivity that such a process would have to anomalous couplings of the top quark with the photon.

For the analytic calculations, the effective Lagrangian approach is used. It is a widely accepted framework where new higher-dimension interaction terms are added to the Lagrangian. The effective Lagrangian has the form:

$$\mathcal{L}_{eff.} = -g' Q_t \bar{\psi}_t \Gamma_e^{\mu} \psi_t A_{\mu}, \quad \text{where} \quad \Gamma_e^{\mu} = \gamma^{\mu} + \frac{i}{2m_t}(\hat{a}_V + i\hat{a}_A \gamma^5)\sigma^{\mu\nu}k_{\nu} \tag{2.4}$$

The form factors $\hat{a}_V$ and $\hat{a}_A$ are the anomalous coupling factors and correspond to the top quark anomalous electric and magnetic dipole moments (EDM and MDM, respectively). The $\hat{a}_A$ term introduces a $\gamma^5\sigma^{\mu\nu}$ term, where $\sigma^{\mu\nu} = i[\gamma^{\mu}, \gamma^{\nu}]/2$, which breaks CP symmetry, so this term determines the strength of a possible CP violation, which might originate from new physics. In case no anomalous couplings exists, this Lagrangian reduces to the SM form of equation 2.3.

The cross-section of this process is then calculated, and a numerical analysis is performed. The dependence of the cross-section on these anomalous moments is studied. The results are presented for $\sqrt{s} = 14$TeV in figure 2.6.

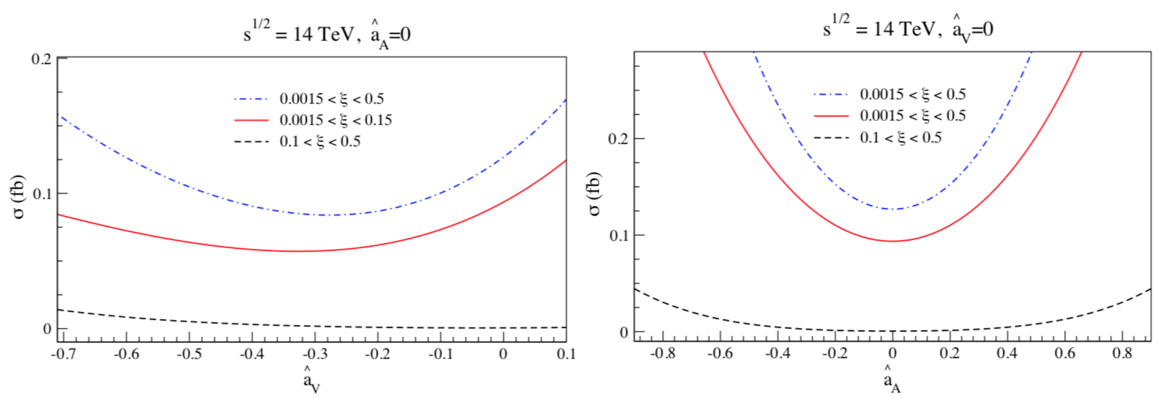

Figure 2.6: The total cross-section of $\mathrm{pp} \rightarrow \mathrm{t\bar{t}pp}$ through $\gamma\gamma$ fusion, as a function of the anomalous top quark anomalous moments $\hat{a}_V$ and $\hat{a}_A$. The curves show the sensitivity for different acceptances of the proton detectors (for the PPS detector described in the next section, the red line is the most accurate prediction, from [5].

The SM predictions for the top quark MDM and EDM are presented in Section 2 of [14]. The MDM is large enough so that it could be potentially measured with enough data. The EDM, however, is extremely small in the SM, so any measurement not compatible with 0 within the uncertainties would be a solid indicator that new physics is present. Therefore, more sensitivity is expected to the top quark EDM with respect to the MDM in this process. It is shown that it should be possible to set improved bounds for both quantities using LHC data.

2.3 Objectives

This work will focus on the search for the production of exclusive top quark pairs, $\mathrm{pp} \rightarrow \mathrm{t\bar{t}pp}$, at the LHC, with the $\mathrm{t\bar{t}}$ decaying through the dilepton channel. The goal is to develop an analysis which combines data from the central detector of CMS with information from the Proton Precision Spectrometer (PPS), using data taken in 2017. Namely, I will develop a selection strategy, based on the work in [21], which allows the separation between signal and the dominant backgrounds, and implement a statistical analysis to set an upper limit on the cross-section of this process. Then, the goal is to develop a classifier using Boosted Decision Trees (BDT), in order to improve the signal from background separation and verify if this allows me to reduce the upper limit for the cross-section. A secondary goal is to improve the reconstruction of the $\mathrm{t\bar{t}}$ system in the dilepton channel, to allow a better comparison between the central (CMS) and forward (PPS) information.

Chapter 3

Experimental considerations

3.1 Collider Physics

Particle physics experiments are mainly performed using high-energy particle accelerators. Accelerators can be used in two types of experiments: (i) fixed-target experiments, where one beam of particles is accelerated towards a stationary target; (ii) collider experiments, in which two beams, accelerated in opposite directions, are brought into collision [13].

In particle accelerators, an important parameter is the centre-of-mass energy, $\sqrt{s}$. The higher this energy, the more massive particles can be produced. This quantity is calculated as the square root of the Lorentz invariant s, from the energy and momentum of the colliding particles:

$$s = (E_1 + E_2)^2 - |\vec{p_1} + \vec{p_2}|^2 \tag{3.1}$$

using natural units, c=1. Particle accelerators work with charged particles, since it is possible to accelerate them stably by applying strong magnetic fields.

Apart from reaching high-energies, it is crucial in a particle accelerator that it produces a great number of collisions per unit time, so that there exists enough statistics to make precision measurements, on the one hand, and to observe extremely rare processes, on the other. The quantity which measures this rate is called the instantaneous luminosity, $\mathcal{L}$.

In a collider, particles are usually grouped in bunches that collide at a given frequency (f) at interaction points, which are surrounded by detectors. If this is the case, one can calculate the instantaneous luminosity, by knowing the number of particles in each bunch (n_1 and n_2), and the root-mean-square (rms) horizontal and vertical beam sizes σ_x and σ_y:

$$\mathcal{L} = f \frac{n_1 n_2}{4\pi\sigma_x\sigma_y} \quad . \tag{3.2}$$

In such an experiment, then, the expected number of events of a given process is the product of its cross-section by the luminosity integrated over the operating time of the experiment:

$$N_{exp} = \sigma \int \mathcal{L}(t)\mathrm{d}t \quad . \tag{3.3}$$

Cross-sections are usually expressed in sub-units of the barn (10^{-24} cm^2), such as the picobarn (pb) and the femtobarn (fb). Luminosity has units of cm^{-2}s^{-1}, and thus integrated luminosity comes in cm^{-2}, or more commonly, in inverse femtobarns, fb^{-1}. Inverting equation 3.3, it is easy to see that one can make a cross-section measurement from the number of experimentally observed events of a given process. One must, however, take into account that detectors have an associated acceptance A (ratio of events in which the final state particles reach the detector) and detection/reconstruction efficiency ε. Thus, the cross-section will be given by

$$\sigma = \frac{N_{obs}}{\int \mathcal{L}(t)\mathrm{d}t \cdot \varepsilon \cdot A} \quad . \tag{3.4}$$

In a physics analysis, there is usually a target process which one is trying to study, called the signal, and several background processes, with similar final states, that one must try to minimise and estimate with precision. If this is the case, N_{obs} in the previous equation is equal to $N_{tot} - N_B$, where N_{tot} is the total number of observed events and N_B is the expected number of background events.

Alternatively, cross-section measurements can be done with reference to a process for which the cross-section is already known (σ_{ref}) [4], by comparing the observed number of events with the number of events for this reference process N_{ref}:

$$\sigma = \sigma_{ref} \frac{N}{N_{ref}} \quad . \tag{3.5}$$

3.2 The Large Hadron Collider

The Large Hadron Collider (LHC) is a 27 km long circular accelerator at CERN, Switzerland, designed to collide hadrons at high energies. It is capable of colliding protons at a centre-of-mass energy of 13 TeV and heavy ions at about 5 TeV, thus being the world's largest and most powerful accelerator. It is composed of two beam pipes, which are tubes kept at ultralight vacuum. Inside these tubes, proton beams are accelerated up to an energy of 6.5 TeV, in opposite directions, by 1232 superconducting dipoles, operating at a temperature of 1.9 K [15], [16].

The accelerated proton beams are allowed to interact at seven different points along the tunnel. In a proton beam there are 2808 bunches, with about 1.2×10^{11} protons each. The bunches collide every 25 ns (40 million collisions per second).

The final products of these collisions are then detected and recorded by the detectors of the LHC experiments. The largest of these experiments are the ATLAS detector [17] and the Compact Muon Solenoid (CMS), described in the next section - two general-purpose experiments. There is also the LHCb [18], which focuses on the study of processes involving the bottom quark and ALICE [19], which studies mainly heavy-ion collisions.

The LHC has been collecting data since 10 September 2008, and is currently undergoing a major

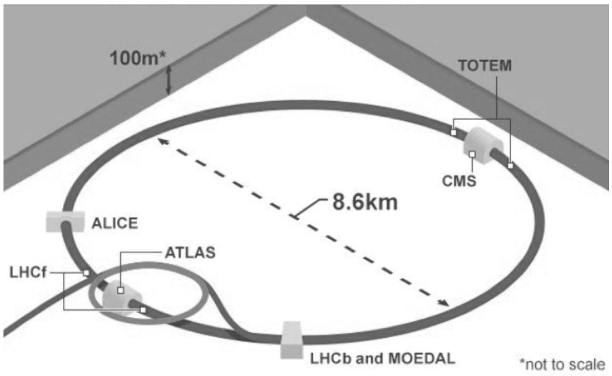

Figure 3.1: Scheme of the Large Hadron Collider, showing the location of different experiments, adapted from [15].

upgrade. It is expected to start collecting data again in 2021, in what will be known as Run3. A scheme showing the plans regarding LHC running can be seen in figure 3.2. The plans for the High-Luminosity LHC (HL-LHC) are also shown. Since the start of its activity, the LHC has been able to improve its performance consistently, regarding the attained luminosity. HL-LHC will be a phase where the luminosity is expected to be even further increased. Due to margins in the design of the nominal LHC, it is expected to be possible to reach about two times the nominal design performance [20]. This may provide enough statistics to measure a number of rare processes that the current LHC capabilities do not yet allow.

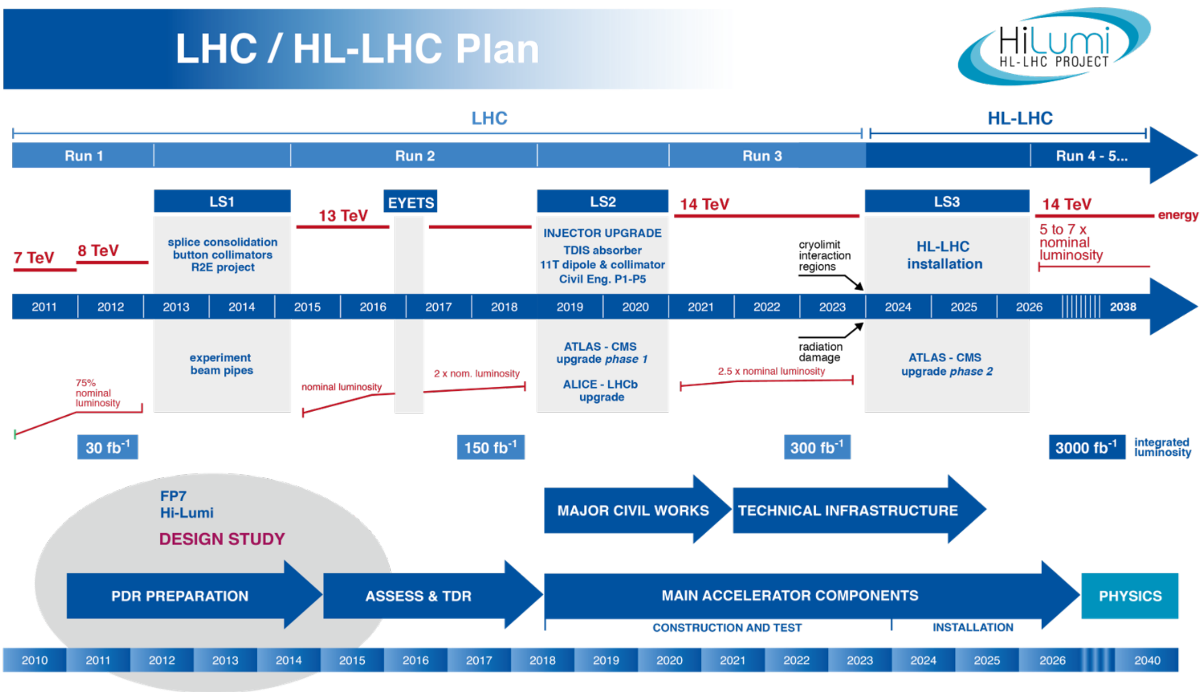

Figure 3.2: LHC Project Schedule, including the schedule for the High-Luminosity LHC phase [20].

3.2.1 Compact Muon Solenoid

The CMS detector is one of LHC's general-purpose experiments. It has a cylindrical shape and consists of a central region where the collisions occur, followed by a silicon tracker, then an electromagnetic calorimeter, and a hadronic calorimeter. Continuing outwards, there is a superconducting solenoid which produces the 3.8 T magnetic field, and the muon chambers (a brief description of these detectors is given in the next subsections, a full description can be found in [21]). A scheme of a slice of CMS is in figure 3.3.

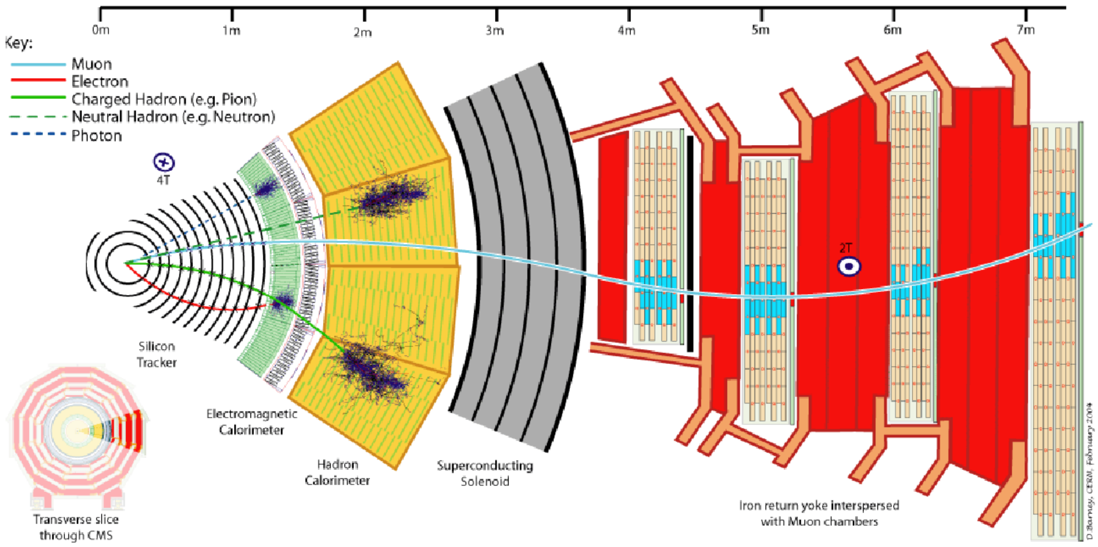

Figure 3.3: Transverse cut of the CMS detector, depicting the trajectory and detection of different particles, from [22].

In terms of geometry, figure 3.4 shows the reference frame, as well as the polar angles θ and ϕ, as they are defined in the CMS detector. It also presents one other angular variable, the pseudorapidity, η, defined as $-\ln[\tan(\theta/2)]$.

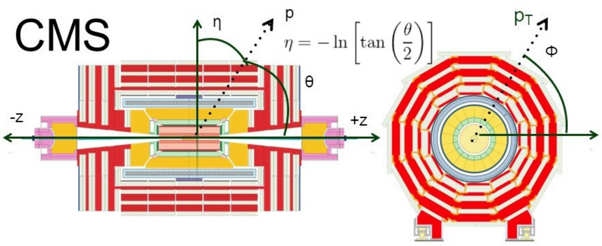

Figure 3.4: Schematic description of CMS geometry and coordinates. The z-axis corresponds to the beam axis, the y-axis is vertical and pointing upwards, and the x-axis horizontal, perpendicular to the beam and point towards the centre of LHC. Adapted from [22].

Silicon tracker

The silicon tracker records precisely the trajectory of charged particles with $|\eta| < 2.5$ (see figure 3.5). Particles with opposite charge bend in opposite directions, due to the presence of the magnetic field, and the curvature radius is proportional to the particle momentum. The tracker has pixels and silicon microstrip detectors: the pixels, at the very core of the detector, deal with the highest intensity of particles, and the strip detectors surround it. As particles travel through the tracker, the pixels and microstrips produce tiny electric signals, collected by 75 million separate electronic read-out channels.

The tracker is essential to reconstruct electrons and muons and to measure their momenta. It is also used to tag jets as originating from b-quarks: the b-hadrons have a lifetime which allows them to travel a certain distance in the tracker before decaying; thus it is possible to measure a displaced vertex, which, combined with other variables, is used for tagging of b-jets [23].

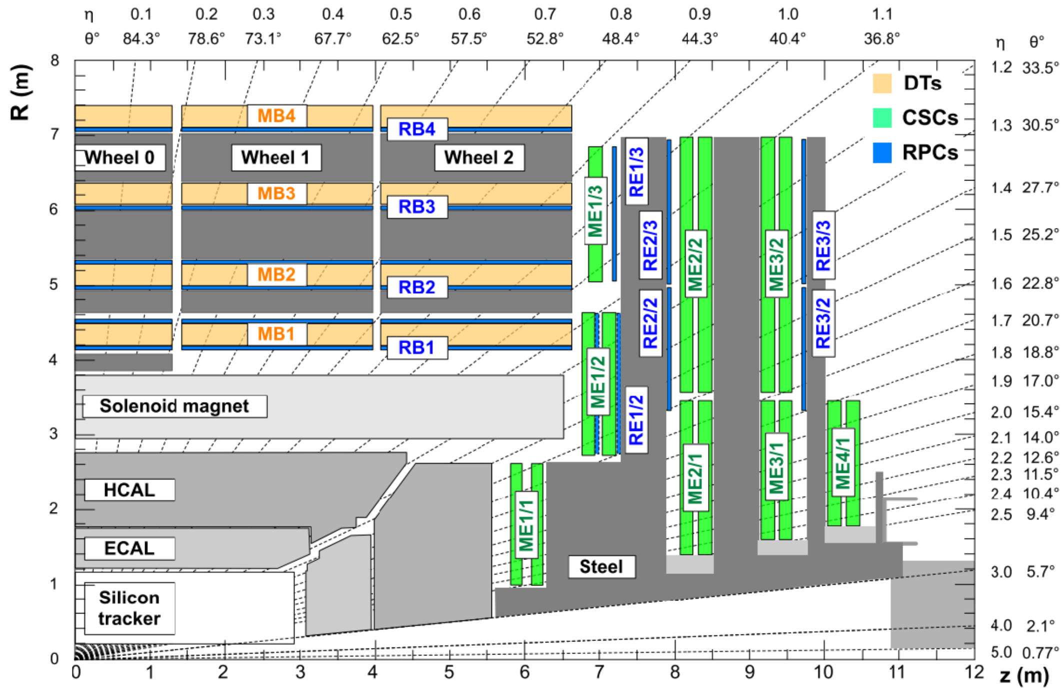

Figure 3.5: z –R transverse section of the CMS detector. The interaction point is located at (0,0) [24].

Calorimeters

The CMS detector possesses two different calorimeter detectors, the Electromagnetic Calorimeter (ECal) and the Hadron Calorimeter (HCal). The first is called electromagnetic calorimeter because it collects the energy of particles which interact through the electromagnetic interaction, like photons and electrons. It is composed of nearly 80000 lead tungstate crystals, very dense and transparent crystals in which the particles deposit their energy. The crystals then emit light in proportion to the particle's energy, in fast, short and well-defined photon bursts. The light is collected using photodetectors glued to the end of each crystal, which convert it into an electrical signal, that is amplified and sent for analysis.

The HCal is designed to detect the hadrons (particles composed of quarks and gluons) which are formed after the collisions and collect their energy. In order to stop the hadrons, layers of an absorber are needed, where the particles lose their energy by interacting with the material, and are alternated with layers of fluorescent scintillator materials, which emit light pulses as particles pass through. Optic fibres collect up this light and transmit it to readout boxes, where photodetectors are used to amplify the signal.

This calorimeter is designed to be ”hermetic”, in the sense that all the energy from all the detectable particles produced in the collision should be collected (except for muons, which can penetrate several metres of iron without interacting). This allows for the measurement of a property known as missing transverse energy ($\not{E}_T$), which is an important sign of the presence of neutrinos or other BSM invisible particles. This measurement relies on the principle of energy and momentum conservation: before a collision, there is no energy in the transverse (x-y) plane, so by summing the transverse momenta of all the detected particles, it is possible to quantify the missing energy and determine its direction.

Muon detectors

Detecting muons with high precision is one of the most important tasks of CMS (hence the name). For that purpose, four stations of gas-ionization detectors are installed outside the solenoid and sandwiched between layers of iron return yoke plates. Muons are reconstructed by combining the tracker information with hits on the gas chambers, and fitting a trajectory. Due to the curvature of this trajectory, caused by the magnetic field, the momentum of the muons can also be precisely measured.

3.2.2 Precision Proton Spectrometer (PPS)

The Precision Proton Spectrometer (PPS) [25] is a detector which was recently built by the CMS and TOTEM (TOTal cross section, Elastic scattering and diffraction dissociation Measurement at the LHC) collaborations. It is located at about 210 m from the interaction point (IP5), on both sides of CMS. It measures the trajectories of protons that have left the collision intact and lost from about 2 to 20% of their momentum. These protons remain inside the beam pipe, and can be measured using position-sensitive detectors, complemented by timing counters to measure the proton arrival time. PPS consists of several detector planes, inserted in specially designed vacuum chambers called ”Roman Pots” (RPs), which are movable near-beam devices located a few mm ($\sim 15\sigma$ in standard runs) from the LHC beam, without damaging it or compromising the functioning of the accelerator. A scheme of one of the arms is shown in figure 3.6.

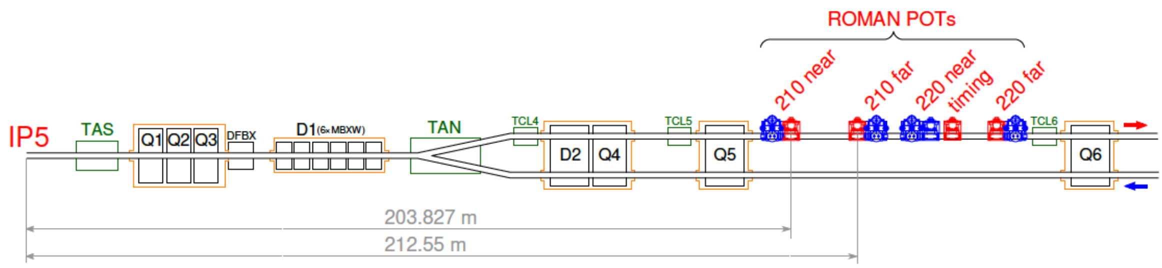

Figure 3.6: Scheme of one arm of CMS, showing the direction of the ingoing and outgoing beams (red and blue arrows) and the approximate position of the RP stations. Stations labelled ”near” are equipped with silicon strips, while those labelled ”far” have pixel detectors (in 2017).

There are two types of RP stations, one for tracking protons and the other for timing detectors. The tracking stations have the look of figure 3.7, where the two vertical pots are used only for alignment and the horizontal one for measurements in standard high-luminosity LHC runs. The timing stations have only one horizontal pot, and the alignment is done by propagating tracks from the tracking stations. In 2016, the RPs from tracking stations were equipped with a superposition of silicon strips. However, in 2017, an upgrade was done, and 3D silicon pixel sensors (similar to the ones used in the CMS tracker) were added. The choice for 3D pixel detectors was made because of the high irradiation fluence ($\sim 3 \times 10^{1}5$ neq/cm^2) that the detectors will be exposed to, for being so close to the beam [26]. Each timing station hosts 3 diamond (time resolution $\sim$ 80 ps) and one Ultra Fast Silicon Detector (time resolution $\sim$ 30 ps) planes. There are 26 RPs in total, placed in pairs on both sides of CMS [27].

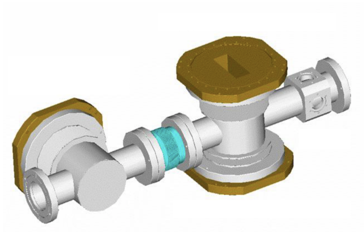

Figure 3.7: Drawing of a tracking RP station, from [28].

In my analysis, I identify the RPs using a 3-digit number, where the first digit is either 0 or 1 according to which arm the pot belongs to (0 for a positive z coordinate: z+ or LHC sector 45, and 1 for negative: z- or LHC sector 56), the second digit is the station number, and the third the RP number. RPs numbered 003 and 103 contain silicon strip detectors, while those labelled 023 and 123 contain 3D pixel detectors. This labelling can be visualised in the scheme of figure 5.1.1.

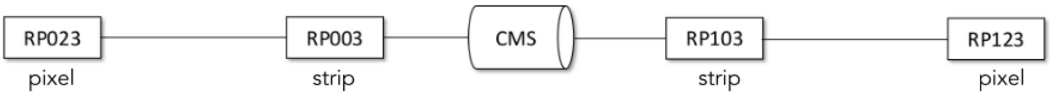

Figure 3.8: Scheme showing the convention used in this thesis in terms of numbering of RP stations.

One of the major difficulties in performing quality measures with PPS is the existence of pileup (multiple proton interactions per bunch crossing). Figure 3.9 shows the efficiency of track reconstruction as a function of the number of interaction vertices. The reconstruction efficiency is evaluated as the ratio of “not empty event and one track reconstructed” and “not empty event”. One can see that for larger pileup, the reconstruction efficiency is worse, as expected. More information on the efficiency of the detectors within PPS can be found in [29].

The plots in figure 3.10 show the typical track multiplicity in 2017 data, for station 023 and 123 (pixel detectors). In figure 3.11 is the fractional momentum loss of the detected protons (ξ), for the same two stations, where

$$\xi = \frac{\Delta p}{p} \quad , \tag{3.6}$$

with p the nominal proton momentum (before the collision) and Δp the momentum lost upon the collision.

In these plots, one can see the acceptance of the pixel detectors (from about 0.02 to 0.18 in station 023 and from about 0.025 to 0.2 in station 123). This unintentional asymmetry is explained by the fact

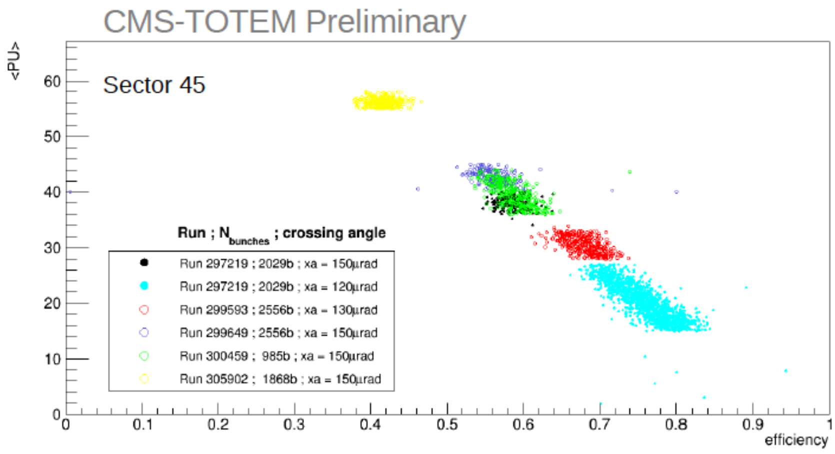

Figure 3.9: Efficiency of track reconstruction in PPS as a function of the number of interaction vertices (pileup - <PU>), for the detectors in sector 45, from [30]. For sector 56 the picture is very similar.

that the dispersion of the two LHC beams is not exactly the same. In fact, the size of the asymmetry is smaller than the precision with which the LHC can control and measure the beams by adjusting the magnet currents. This is briefly discussed in [31].

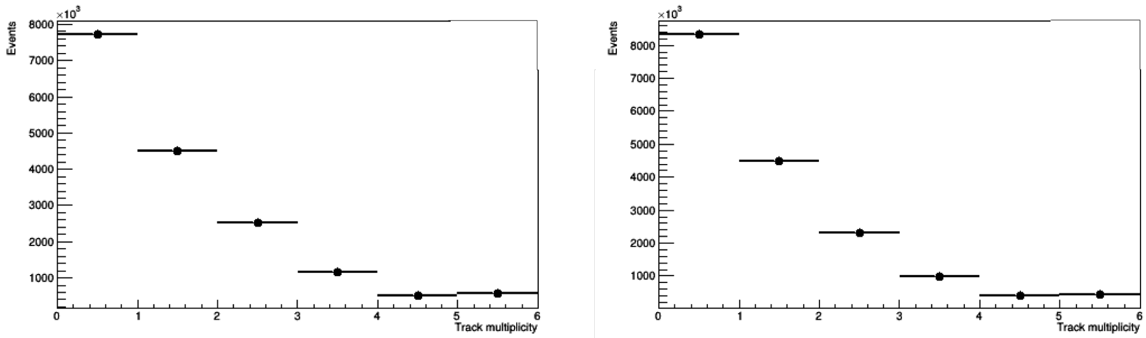

Figure 3.10: Pixel detectors track multiplicity (per event) in 2017 data, for RP stations 023 (left) and 123 (right).

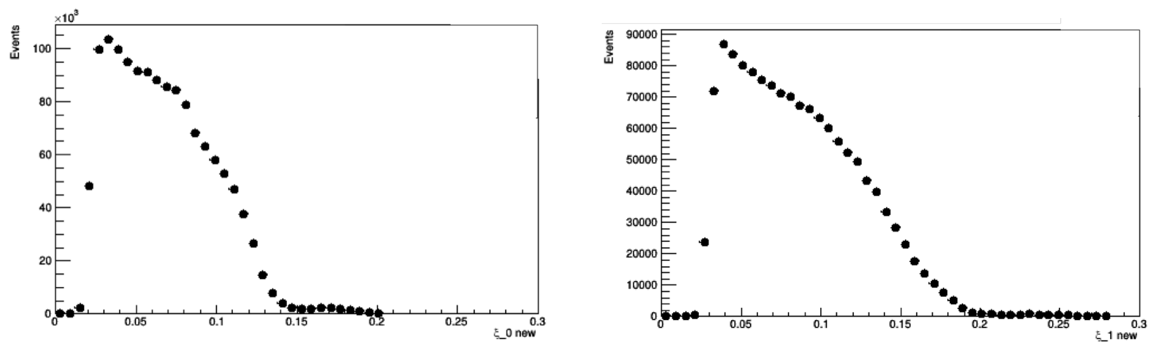

Figure 3.11: Fractional momentum loss (ξ) of protons reconstructed from RP stations 023 (left) and 123 (right), in 2017 data.

Figure 3.12 shows the total integrated luminosity recorded by the CMS and PPS experiments in 2017.

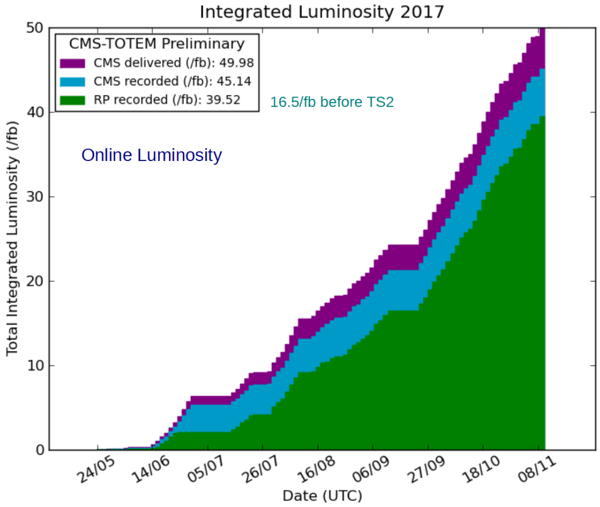

Figure 3.12: Total integrated luminosity recorded by the CMS and PPS experiments in 2017, from [30].

3.3 Some kinematics definitions in CMS and PPS

One of the most important physics observables in CMS is the transverse momentum, p_T, of the final state particles. This is the component of the momentum $\vec{p}$ in the transverse (x-y) plane:

$$p_T = \sqrt{p_x^2 + p_y^2} \quad . \tag{3.7}$$

Using the special relativity equation $E^2 = m^2c^4 + p^2c^2$ and setting c=1 (natural units), one can define a quantity called the invariant mass, by:

$$m = \sqrt{E^2 - \vec{p}^2} \quad . \tag{3.8}$$

This variable, as the name indicates, is a Lorentz invariant, meaning it will remain constant when changing the reference frame. For example, if one has events where Z-bosons decay into an electron and a positron, one can calculate the invariant mass of the electron-positron system and the result should be a distribution centred around the Z-boson mass ($m_{e^+e^-} = \sqrt{(E_{e^+} + E_{e^-})^2 - (\vec{p}_{e^+} + \vec{p}_{e^-})^2} = M_Z$).

Apart from the energy and momentum, it is useful to take advantage of the angular information provided by the detector. The most commonly used angular quantities are the pseudorapidity η and the angle ϕ , defined in section 3.2.1. One can build a variable which quantifies the angular separation between two particles, by summing the squared differences of these two quantities. This is called ΔR, and calculated as:

$$\Delta R \equiv \sqrt{(\Delta\eta)^2 + (\Delta\phi)^2} \quad . \tag{3.9}$$

An alternative variable to the pseudorapidity is the rapidity, y, calculated as

$$y \equiv \frac{1}{2} \ln\left(\frac{E + p_{\mathrm{L}}}{E - p_{\mathrm{L}}}\right) \quad . \tag{3.10}$$

In the relativistic limit, where the momentum of the particle is much larger than its mass ($E \approx |\vec{p}|$), then $\eta \approx y$.

In PPS, when at least one proton track is reconstructed on each arm of CMS, one can take the ξ of each proton candidates and use it to reconstruct the invariant mass and rapidity of the two proton system (m_{pp} and y_pp). In the case of exclusive production, these quantities will correspond to the total invariant mass and rapidity of the central system. The equations that relate the ξ of each proton with m_{pp} and y_pp are the following:

$$M_{pp} = \sqrt{s\xi_0\xi_1} \tag{3.11}$$

$$y_{pp} = \frac{1}{2}\ln\left(\frac{\xi_0}{\xi_1}\right) \ , \tag{3.12}$$

where the subscripts 0 and 1 refer to the arm index.

Chapter 4

State of the art

In this chapter, I present some of the most relevant work that has been done in this area, both in the context of top anti-top quark production measurements, and in the context of forward physics in CMS. I present the first physics result obtained using PPS, and discuss the analysis that led to this result, which served as a starting point for this thesis work. As for the exclusive production of top quark pairs, no previous searches have been reported.

4.1 Inclusive $t\bar{t}$

The first measurement of the cross-section of $t\bar{t}$ production, performed in 2010 [32], was an extremely important milestone for the LHC and the CMS experiment, since most of the new physics models that the LHC was designed to test either include top quarks or have $t\bar{t}$ production as one of the main backgrounds. In this thesis, inclusive $t\bar{t}$ production refers to events where a $t\bar{t}$ pair is produced with one or both of the protons being disrupted in the process, as opposed to exclusive $t\bar{t}$, where both protons are kept intact. The latter is, however, several orders of magnitude less probable, and when measuring $t\bar{t}$ properties, any contribution from exclusive production is completely neglegible.

In this section, I present the most recent measurement of this process, by the CMS collaboration, with a total integrated luminosity of 35.9 fb^{-1} [33]. The dilepton channel is explored (pp$\rightarrow t\bar{t}\rightarrow$ b b $l^{+}\bar{\nu}_{l}$ $l'^{-}\nu_{l'}$), due to its purity. A similar selection of $t\bar{t}$dilepton events is used in this work, discussed later in section 6.1.

The reconstructed interaction vertex in each CMS event with the largest value of summed transverse momentum (of all physics objects) was taken to be the primary pp interaction vertex. Dilepton triggers with specific p_T requirements are used. Two oppositely charged leptons (electrons and/or muons), reconstructed within $|\eta| < 2.4$, with $m_{ll} < 20$ GeV and properly isolated from neighbouring particles are required. Moreover, leptons are required to be consistent with originating from the primary interaction vertex.

At this stage, the main backgrounds is from Drell-Yan (DY) events (Z/$\gamma^{*} \rightarrow e^{+}e^{-}$ or $\mu^{+}\mu^{-}$). In order to improve the separation, the following selection is applied:

- For final states with e^+e^- and $\mu^+\mu^-$, events with an invariant mass of the reconstructed lepton pair around the Z mass ($76 < m_{ll} < 106$ GeV) are excluded, to reduce DY contribution;

- At least 1 b-tagged jet is required.

The events are then categorised according to the number of b-tagged jets (1,2,≥3 b-tags) and to the flavour of the final state leptons (ee, $\mu\mu$ or $e\mu$). Additionally, events are further categorised by the number of additional non-b-tagged jets in the event. The number of jets and number of b-tags can be seen in figure 4.1 for the $e\mu$ channel. A statistical analysis is performed, assuming a top quark mass of $m_t = 172.5$ GeV [34], and the total cross-section is measured to be $\sigma_{t\bar{t}} = 803 \pm 2$(stat)$\pm 25$ (syst)± 20 (lumi) pb. The result agrees with the theoretical predictions at next-to-next-to-leading order (NNLO) in perturbative QCD, which predict 832 ± 20(scale)± 35 (PDF+α_s) pb, where α_s is the strong coupling constant.

In [33], they also perform the total $t\bar{t}$ cross-section measurement by leaving the mass of the top quark as a free parameter in the fit. In this case, they obtain $\sigma_{t\bar{t}} = 815 \pm 2$(stat)$\pm 29$ (syst)± 20 (lumi) pb for the cross-section and $m_t = 172.33 \pm 0.14$ (stat)$^{+0.66}_{-0.72}$ (syst) GeV for the top mass, in agreement with the theoretical calculations. The coupling constant of the strong interaction is also estimated from these measurements.

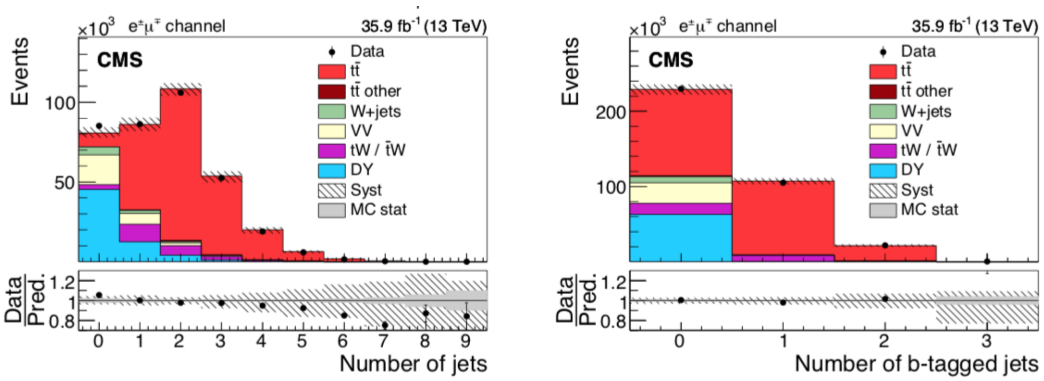

Figure 4.1: Distributions of the number of jets and number of b-tagged jets, for data and simulation, for events passing the selection, with an electron and muon in the final state.

4.2 Exclusive dileptons

The central (semi)exclusive production of two high-energy leptons was observed by the CMS-TOTEM collaboration using PPS, in 2018 [35]. This is a significant result, being the first observation of proton-tagged $\gamma\gamma$ collisions at the electroweak scale, and showing that PPS performs according to its specifications. Furthermore, the selected final state (two leptons) includes the dileptonic $pp \rightarrow t\bar{t}pp$ final states; therefore, the selection done in this article is a very useful starting point for my analysis.

Data from 2016 are used, with an integrated luminosity of 9.4 fb^{-1}. The processes they looked for are represented in the Feynman diagrams of figure 4.2. The left and centre processes are considered as signal in this analysis, while the one on the right, where no proton stays intact, is treated as background, and contributes if a proton from another interaction in the same bunch-crossing (pileup) is detected in PPS.

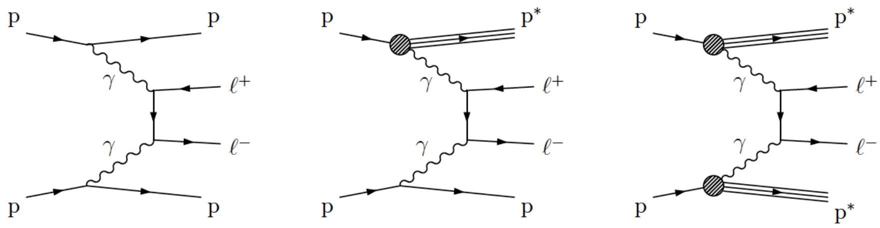

Figure 4.2: Feynman diagrams for central production of dilepton pairs by $\gamma\gamma$ fusion. Left: none of the protons is dissociated, Center: one proton suffers dissociation and the other is kept intact, Right: both protons are dissociated.

The alignment process of the PPS detectors, as well as the proton reconstruction method, are determined using a combination of data and simulated events. From each track recorded in the detector, the fractional momentum loss, $\xi = \Delta p/p$, is calculated, where p is the nominal beam momentum and Δp the longitudinal momentum loss. This is done using beam optics, a method that treats the elements in the beamline as optical lenses, and relates the momentum of the proton scattered at the IP with the momentum measured at the RP position through "transport" matrices, which describe the proton transport through the LHC.

A central selection is applied. Two leptons of the same flavour (muons or electrons) are required, with $p_T > 38(33)$ GeV for each muon (electron). Only leptons of opposite charge are kept. The muon/electron tracks are reconstructed to a common vertex, and the resulting vertex position is required to be consistent with that of a collision. Furthermore, the event is only accepted if no additional tracks are found from a nearby region, along the z direction, around the primary vertex. Then, the azimuthal angle difference $\Delta\phi$ is required to be consistent with the 2 leptons being back-to-back. Figure 4.3 shows the invariant mass and rapidity of the dilepton systems for the selected events.

The data that pass the central selection are matched with the PPS data. For events that pass the selection and show at least one track in the RPs, the expected fractional proton momentum loss ξ can be calculated from the transverse momentum p_T and pseudorapidity $\eta = -\ln\tan(\theta/2)$ (θ is the angle between the particle and the positive direction of the beam axis) of each lepton:

$$\xi(l^+l^-) = \frac{1}{\sqrt{s}}\left(p_T(l^+)e^{\pm\eta(l^+)} + p_T(l^-)e^{\pm\eta(l^-)}\right) \tag{4.1}$$

The two solutions for $\pm\eta$ correspond to the protons moving in the ±z direction. The expected ξ is then compared with the observed one (this comparison can be seen in figure 4.4. For the $\mu^+\mu^-$ final state, 12 events were found with a track in at least one of the two RPs, matching $\xi(\mu^+\mu^-)$ within 2σ. For the e^+e^- final state, the number of events is 8. Considering the background estimates, these observations have a significance of 4.3 σ and 2.6 σ, for the ee and $\mu\mu$ final states, respectively.

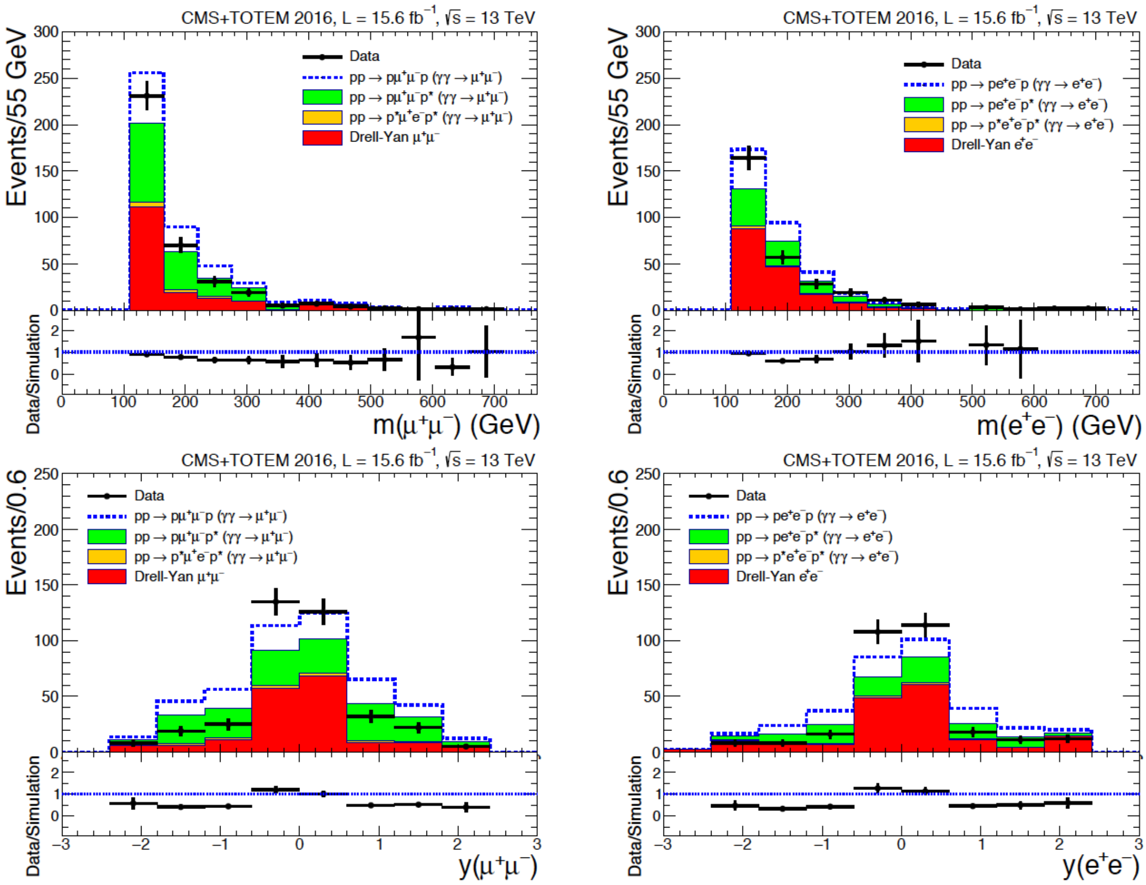

Figure 4.3: Dimuon (left) and dielectron (right) invariant mass (top) and rapidity (bottom), after all central-detector criteria are applied, in pp collisions at 13 TeV. The ratio between data and all simulated events (simulated signal + background) is shown in the lower panel of each plot. From [35].

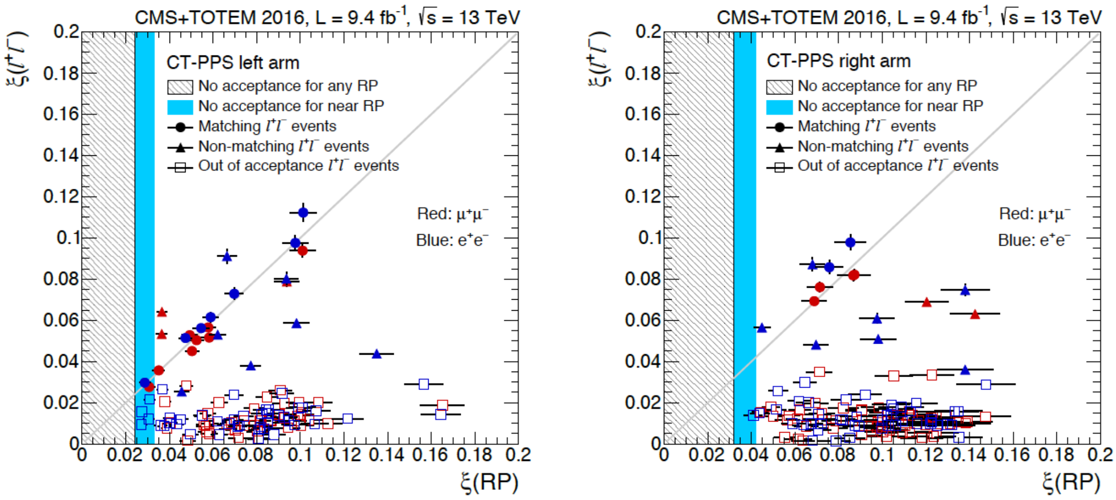

Figure 4.4: Comparison between the ξ obtained in the central system, for selected events, and the ξ from the RPs tracks, for both arms of PPS, from [35].

Chapter 5

Analysis Tools

In this chapter, I list the data and simulation samples that were used for the analysis. I also discuss the signal process, in terms of kinematics, and present the main backgrounds. Finally, I present the two different analysis approaches and the statistical methods which were employed to derive the cross-section results.

5.1 Data and simulation samples

5.1.1 Data samples

The analysis is performed using proton-proton collisions data at $\sqrt{s} = 13$ TeV collected in 2017 by CMS. The total integrated luminosity corresponds to 41.8 fb^{-1}. The primary datasets with inclusive single- and double-lepton triggers, i.e. SingleMuon, SingleElectron, DoubleMuon, DoubleEG and MuonEG, available from March 31 2018, have been used. These are datasets which contain events with offline reconstructed electrons or muons. Then, a set of High Level Trigger (HLT) requirements was applied (for the list of trigger names see Appendix A). These triggers select electrons and muons which are reconstructed above a certain p_T threshold, within a rapidity interval, properly isolated from other particles in the detector.

To avoid double-counting, events from the SingleElectron and SingleMuon datasets for which the di-electron and the di-muon triggers fired, respectively, were not considered. Furthermore, events with electron-muon trigger are only accepted if they come from the MuonEG dataset (dataset with one reconstructed electron and one muon).

For the correlation between the central detector and the PPS, only data from RPs 003, 023, 103 and 123 (following the numbering scheme from figure) were used, since no alignment parameters exist for other pots. Besides, only collisions for which the LHC beam crossing angle was 120, 130, 140 or 150 μrad are considered (this is the majority of 2017 collisions). The total integrated luminosity where combined CMS-PPS data have been analysed with calibrated pixels is thus reduced to 39.5 fb^{-1}.

In terms of proton reconstruction, the reconstruction recipe validated in November 2018 is being used. This is not the most up-to-date reconstruction recipe. The most recent one is from May 2019, however the datasets that include it are still being processed. These recipes are not yet public, but are similar to the ones applied to 2016 data, which can be seen in [31, 36].

To compensate for this, a set of *a posteriori* corrections are applied for each crossing angle, which account for most of the effect of this new alignment. The difference between the data before and after alignment and calibration corrections is shown in Appendix C.

5.1.2 Simulation samples

The official Monte Carlo production samples were used for the background. These were produced using Madgraph/Powheg/MC@NLO [37, 38], with Pythia8 [39] used to do the showering and hadronization. The names of the samples and the cross sections used to normalise them is summarised in Tab. 5.1. The $\mathrm{t\bar{t}}$ cross-section has been calculated according to the recommendations in [40], at next-to-next-to leading order (NNLO) in QCD including resummation of next-to-next-to-leading logarithmic (NNLL) soft gluon terms with top++2.0 (see [41] and references therein). The single top cross-section was computed using NNLO approximate calculations [42]. The cross-sections for the remaining processes were all calculated following the instructions in [43].

Table 5.1: MC samples from the RunIIFall17MiniAODv2-PU2017_12Apr2018_94X_mc2017_realistic_v14 production used in this analysis, and the corresponding process and cross section values.

Process	σ [pb]	MC sample
		Background samples
Z/γ^* ($10 < M(\ell\ell) < 50$ GeV)	18610	DYJetsToLL_M-10to50_TuneCP5_13TeV-madgraphMLM-pythia8
Z/γ^* ($M(\ell\ell) > 50$ GeV)	5765.4	DYJetsToLL_M-50_TuneCP5_13TeV-amcatnloFXFX-pythia8
tW	35.85	ST_tW_top_5f_inclusiveDecays_TuneCP5_PSweights_13TeV-powheg-pythia8 ST_tW_antitop_5f_inclusiveDecays_TuneCP5_PSweights_13TeV-powheg-pythia8
$t\bar{t}$	832	TTJets_TuneCP5_13TeV-amcatnloFXFX-pythia8
ZZ	12.14	ZZ_TuneCP5_13TeV-pythia8
WZ	27.6	WZ_TuneCP5_13TeV-pythia8
WW	75.8	WW_TuneCP5_13TeV-pythia8
W+jets	61526.7	WJetsToLNu_TuneCP5_13TeV-madgraphMLM-pythia8
$\gamma + jets$ ($40 < H_T < 100$)	20790	GJets_HT-40To100_TuneCP5_13TeV-madgraphMLM-pythia8
$\gamma + jets$ ($100 < H_T < 200$)	9238	GJets_HT-100To200_TuneCP5_13TeV-madgraphMLM-pythia8
$\gamma + jets$ ($200 < H_T < 400$)	2305	GJets_HT-200To400_TuneCP5_13TeV-madgraphMLM-pythia8
$\gamma + jets$ ($400 < H_T < 600$)	274.4	GJets_HT-400To600_TuneCP5_13TeV-madgraphMLM-pythia8
$\gamma + jets$ ($H_T > 600$)	93.46	GJets_HT-600ToInf_TuneCP5_13TeV-madgraphMLM-pythia8
QCD EM enriched ($15 < \hat{p}_T < 20$)	2302200	QCD_Pt-15to20_EMEnriched_TuneCP5_13TeV_pythia8
QCD EM enriched ($20 < \hat{p}_T < 30$)	5352960	QCD_Pt-20to30_EMEnriched_TuneCP5_13TeV_pythia8
QCD EM enriched ($30 < \hat{p}_T < 50$)	9928000	QCD_Pt-30to50_EMEnriched_TuneCP5_13TeV_pythia8
QCD EM enriched ($50 < \hat{p}_T < 80$)	2890800	QCD_Pt-50to80_EMEnriched_TuneCP5_13TeV_pythia8
QCD EM enriched ($80 < \hat{p}_T < 120$)	350000	QCD_Pt-80to120_EMEnriched_TuneCP5_13TeV_pythia8
QCD EM enriched ($120 < \hat{p}_T < 170$)	62964	QCD_Pt-120to170_EMEnriched_TuneCP5_13TeV_pythia8
QCD EM enriched ($170 < \hat{p}_T < 300$)	18810	*missing in action*
QCD EM enriched ($\hat{p}_T > 300$)	1350	QCD_Pt-300toInf_EMEnriched_TuneCP5_13TeV_pythia8

In addition, a signal $pp \to p\gamma p \to \mathrm{t\bar{t}}pp$ sample has been produced privately using FPMC [44] as the matrix element generator and HERWIG++ [45] as the parton shower. As cross-section, the value of 1 pb was used for the normalisation of the signal. The most recent calculations for the expected signal cross-section predict a value of 0.29 fb. [8].

5.2 Exclusive $t\bar{t}$ analysis

The exclusive $t\bar{t}$ process, in the dilepton channel, corresponds to the Feynman diagram of figure 5.1. The final-state particles in the central detector are two b-quarks, two leptons and two neutrinos. The b-quarks hadronise and form jets. In the analysis, we'll use leptons as a shorthand for energy deposits in the calorimeter combined with tracker and muon chamber information, through the so-called particle flow algorithm.

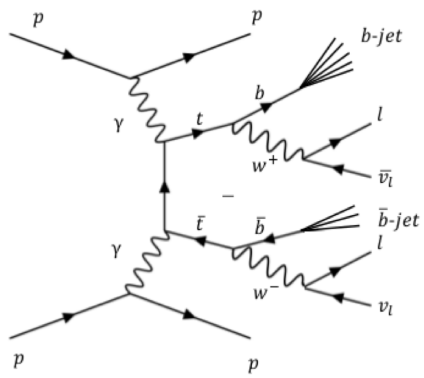

Figure 5.1: Feynman diagram of the exclusive $t\bar{t}$ dilepton channel.

In terms of detector information, the jets can be detected through the energy deposits in the calorimeter, and can be tagged as originating from a b-quark, as mentioned in section 3.2.1.

Electrons and muons leave tracks in the silicon tracker. Continuing outwards, electrons deposit their energy in the electromagnetic calorimeter, while muons are detected in the muon chambers. Final state neutrinos are not detected directly, since they do not interact with the detector, and their presence can only be inferred due to the principle of energy conservation: if one detects the existence of missing energy in the transverse plane (denoted $\not{E}_T$), this can be used to reconstruct the sum of the neutrino's p_T.

Additionally, the two recoiling protons, intact after the collision, can be detected in the PPS if they fall within the detector acceptance, thus adding a clear signature to this process.

In general, a background in a particle physics analysis is a known physics process which produces a similar final state to the process under study (called the signal). For this process, the main background is expected to be from non-exclusive $t\bar{t}$ production, that is, $t\bar{t}$ production via the diagrams in figure 2.2. The final state of this process is expected to be exactly the same as described for the signal, with very few kinematic differences. The most significant difference is, naturally, the absence of the outgoing recoil protons. Another important background is from Drell-Yan production, when a quark and an anti-quark interact to produce a Z-boson or a virtual photon which then decays into a pair of leptons, as in figure 5.2. Most of Drell-Yan events will not have jets in the final state; however, the quarks can emit gluons, which in turn produce quark anti-quark pairs, originating jets. If this is the case, the signature of this process is again similar to the signal.

Other background processes have to be considered, even though they are not dominant after the pre-

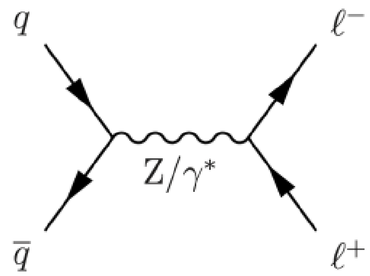

Figure 5.2: Feynman diagram for Drell-Yan production.

selection. One of these backgrounds is what is known as Multiboson production, namely the production of two W bosons (WW), two Z bosons (ZZ) or one Z and one W (WZ). These processes can have both leptons and jets in the final state, which mimic the signature of $t\bar{t}$. Another process is the production of a W boson, that may also contain jets due to emission of gluons by the initial quarks. Other backgrounds include γ+jets, the production of a photon in association with jets, and what is known as QCD, the production of multiple jets from quark and gluon fusion, which is a very abundant process in hadron colliders and at the LHC in particular. QCD processes may appear as signal in the case when two of the jets are erroneously reconstructed as leptons, or are produced together with DY events or W/Z bosons.

Kinematic differences between signal and backgrounds

Although it has a large production cross-section, the Drell-Yan (DY) events can be efficiently separated from the exclusive ttbar signal. On the one hand, in the DY process, the final state leptons are necessarily of the same flavour (two electrons or two muons). On the other hand, this process is dominated by Z-boson production, and in this case, the distribution of the invariant mass of the two leptons will have a large concentration of events (peak) around the Z-boson mass (~91.2 GeV).

When it comes to the inclusive $t\bar{t}$ background, the story is more complicated. Selecting events with PPS tracks is the most obvious choice, however, as shown in section 3.2.2, the PPS signal is overwhelmed with protons coming from pileup, which randomly reach PPS. Thus, there is need to explore the kinematic differences of the central process. The main difference would be the fact that exclusive $t\bar{t}$ events are expected to be produced more back-to-back (higher angular difference) than the inclusive ones. There are two main reasons for this:

- The top quark pair, in the exclusive process, is produced through an electroweak vertex, so no extra activity (from soft gluons or initial state radiation) is expected in the event, and thus there are no particles for the tops to recoil against. Due to momentum conservation, the top and anti-top are expected to be back-to-back;
- The electromagnetic form factor of the proton heavily suppresses photon-exchange with large transverse momentum when the protons stay intact. So the $t\bar{t}$ system is expected to have a total p_T ~0, that is, the tops must be produced back-to-back [8].

The second reason is illustrated in figure 5.3, where the expected $t\bar{t}$ transverse momenta for the exclusive (elastic-elastic) and the inclusive (elastic-inelastic or inelastic-inelastic) cases are shown.

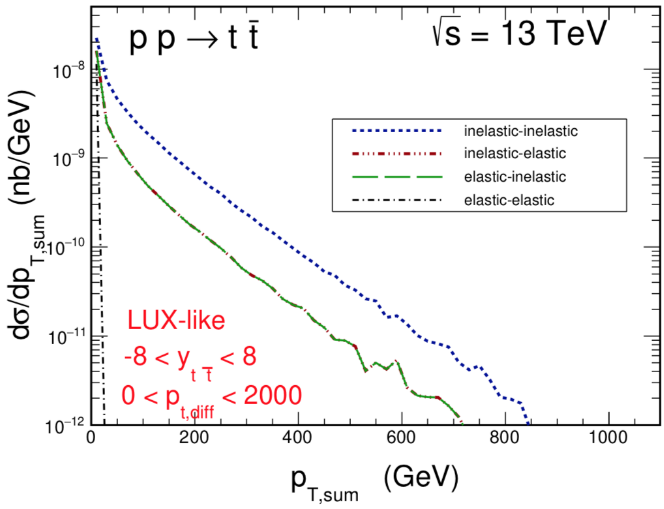

Figure 5.3: Simulated distributions of the transverse momentum of the $t\bar{t}$ pairs for elastic-elastic, inelastic-elastic (elastic-inelastic) and inelastic-inelastic contributions to the exclusive $t\bar{t}$process, from [8]. The "LUX-like" label in the picture refers to the LUX framework, that models the photon content inside the proton, and was used to compute these distributions [46].

5.2.1 Cut-based analysis

A cut-based analysis works based on a simple principle: find the observables which provide higher discimination between signal and backgrounds, and define cuts to apply to the data, in order to reject as much background as possible while keeping a reasonable amount of signal events.

5.2.2 Multivariate analysis

ROOT's TMVA

In high-energy physics, there are often large amounts of data and a large number of variables at play. In such cases, the optimal way of selecting signal from background events by applying cuts is not trivial. Techniques which are able to take advantage of different correlations between variables for signal and background, and perform n-dimensional cuts, are thus quite useful. The Toolkit for Multivariate Data Analysis with ROOT (TMVA) [47] is a toolkit containing a large variety of multivariate classification algorithms. It provides a number of options for training, testing, performance evaluation and application of the classifiers, with a user-friendly interface.

Boosted Decision and Regression Trees

A decision (regression) tree is a binary tree-structured classifier (regressor). Decision trees are used to separate signal from background, while Regression trees are used to estimate the value of a given "target" variable. Both are based on yes/no decisions on one single variable at a time, which divide the phase space into several regions, until a stop criterion is reached. In the case of classifiers, the output regions are classified as signal or background, according to the origin of the majority of training events that end in this node. In the case of regressors, the output node represents a specific value of the target variable.

The boosting extends this concept to an ensemble of trees, called a *forest*. The trees are all built from the same training data, by reweighting events,[1] and they are finally combined into a single classifier (regressor) which is the weighted average of the individual trees.

In a boosted decision tree (BDT), each split corresponds to a cut on the variable that is the best at separating signal from background at that point (see the structure of figure 5.4). In the end, the BDT output is a function that is applied to an event and gives a number, usually from -1 to 1, where the closer to 1 the more signal-like the event is, and conversely the closer to -1 the more background-like. Applying a cut on this BDT output is the typical way of performing a physics analysis using this method.

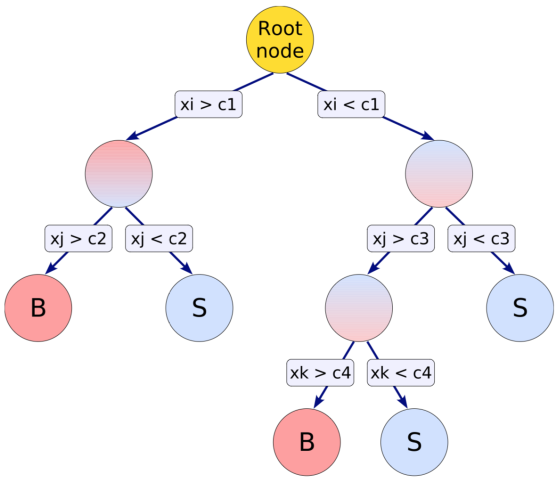

Figure 5.4: Scheme showing the structure of a BDT. The variables x_i are then used to perform the cuts.

In a boosted regression tree (BRT), the splits are done similarly, but cutting on the variable which causes the maximum decrease in the average squared error of the estimated target value. If the target is, for example, the ratio between the value of an unknown variable b and a known variable a, target $= b/a$, the output of the regressor is a correction factor C that one can apply to a so that $C * a$ is an estimate of b.

For all types of boosted trees, the sample is divided into two sets: one for training and one for testing. The training is done as described above, using the training set, and produces a file with a set of weights to be applied. The testing consists of applying these weights to the test set. The classification results for both sets are usually compared, in order to check for overtraining. Overtraining occurs when the classifier is too flexible; that is, it has too many degrees of freedom: too many adjustable parameters for too few training events. The consequence of this is that the trees may learn specific features of the training set, which are not actual physics characteristics of the process. This often reflects in a disagreement between the BDT output of the two sets, and if it is observed, it must be corrected, since an overtrained classifier will not perform well when applied to the data.

[1] Several reweighting methods exist. In this work, one of the most popular methods, Adaptive Boost (*AdaBoost*) is used. This method starts with the original event weights when training the first decision tree, then the subsequent tree is trained using a modified sample where the weights of previously misclassified events are increased by a certain factor, and so on.

A visual representation of the concept of overtraining is shown in figure 5.5. Let x_1 and x_2 be two variables accessible in the data, and the blue and red points correspond to background and signal points, respectively. Then, an intuitively adequate cut to apply would be the cut on the left of the figure, since it seems to reflect the general tendency of the distribution and is likely to give better results when applied to another statistically independent data set. The cut on the right, on the contrary, seems to reflect the specific features of the dataset, rather than the general features. The latter is a typical example of what we call overtraining.

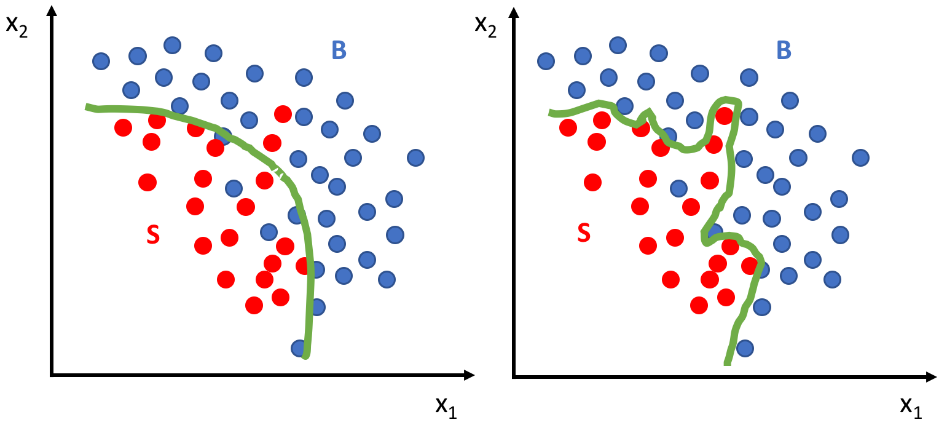

Figure 5.5: Scheme depicting the concept of overtraining. On the left, a seemingly reasonable cut is applied on a 2-d distribution to separate signal and background. On the right, the cut which is applied reflects the specific characteristics of the dataset, and is unlikely to perform well when applied to a different one (overtraining).

Several causes exist for overtraining: the number of trees being used, the sizes of the training and test sets, the number of variables, the choice of algorithms, and others. When doing an MVA analysis, one must make sure that there is no overtraining, otherwise, when applying the BDT weights to data, it will not classify events correctly.

5.2.3 Method employed in the statistical analysis

The cut-based or multivariate analyses result on the definition of separate signal and control regions (subsets of the data which are rich in signal and background events, respectively). The number of events expected and observed in the signal and control regions can be used as inputs to a statistical analysis, which allows us to set limits on the production cross-section of $\mathrm{pp} \rightarrow \mathrm{t\bar{t}pp}$.

In order to do it, we parametrise the total number of events expected in a single category as follows:

$$N_{\mathrm{exp}} = N_{\mathrm{exp}}(\mathrm{pp} \rightarrow \mathrm{t\bar{t}pp}) + f \cdot \left[N_{\mathrm{exp}}(\mathrm{t\bar{t}}) + N_{\mathrm{exp}}(\mathrm{DY}) + N_{\mathrm{exp}}(\mathrm{others}) \right] \quad , \tag{5.1}$$

where f is the probability that a non-exclusive event passes the selection of the RPs due to combinatorial tracks. This factor f is independent of the process because it is only related with pileup. In Eq. 5.1 we assume that there is no additional exclusive process which may contribute in the selected regions. The control regions (CRs) for the $\mathrm{t\bar{t}}$ and DY processes, defined in the next chapter, are used to normalise the initial expectations based on simulation. We thus employ $\mu_{\mathrm{t\bar{t}}}$ (μ_{DY}) as scaling factors of the initial expectations for $\mathrm{t\bar{t}}$(DY), i.e.:

$$N_{\mathrm{exp}}(b) = \mu_b \cdot N^{\mathrm{MC}}_{\mathrm{exp}}(b) \quad , \tag{5.2}$$

where b=$\mathrm{t\bar{t}}$, DY and $N^{\mathrm{MC}}_{\mathrm{exp}}(b)$ is the expectation from simulation which includes the theory cross-section, the integrated luminosity, and the corrections for the simulated efficiency with data-MC scale factors. Other processes in Eq. 5.1 will float constrained according to the estimated uncertainty. The expectations for the signal are written as a product of the following factors:

$$N_{\mathrm{exp,c}}(\mathrm{pp} \to \mathrm{t\bar{t}pp}) = A \cdot L \cdot \varepsilon_{\mathrm{c}} \cdot \sigma(\mathrm{pp} \to \mathrm{t\bar{t}pp}) \quad , \tag{5.3}$$

where c=ee,$e\mu$,$\mu\mu$ is the event category, A is the acceptance at generator level for the selection of two leptons and an invariant mass of the outgoing protons in the acceptance of the PPS detector, L is the total integrated luminosity, ε_{c} is the efficiency of the selection and $\sigma_{\mathrm{pp}\to\mathrm{t\bar{t}pp}}$ is the cross-section. Given that the selection criteria differ slightly in the ee, $\mu\mu$ and $e\mu$ categories, in Eq. 5.3, the efficiency factors are computed separately for each category. With these definitions in hand, we can maximise the following likelihood as function of $\sigma_{\mathrm{pp}\to\mathrm{t\bar{t}pp}}$:

$$\mathcal{L} = \prod_{k=1}^{N} \mathcal{P}_{\mathrm{oisson}}(N_{\mathrm{obs}}|N_{\mathrm{exp}}) \cdot \prod_{m=1}^{M} f(\theta_k) \quad , \tag{5.4}$$

where the first product runs over the N categories in which events are counted, and the second product runs over M nuisance parameters which encode the relative uncertainty of the parameters employed to parametrised the expectations N_{exp}. The PDF $f(\theta_k)$ is taken as a log-normal function, that is, a function whose logarithm is normally distributed. The implementation of Eqs 5.1- 5.4 is made in RooStats, using the Higgs Combination Tool [48, 49].

Two different methods within the Higgs Combination Tool are used. The first is the *AsymptoticLimits* method, which provides an estimate of the observed and expected limits. It yields accurate results when the event yields are not too small, and the systematic uncertainties do not play a major role in the result. This calculation relies on an asymptotic approximation of the so-called LHC test-statistic, defined as

$$q_r = -2\ln[\mathcal{L}(\mathrm{data}|r, \hat{\theta}_r)/\mathcal{L}(\mathrm{data}|r = 0, \hat{\theta}])} \quad , \tag{5.5}$$

that is, proportional to the logarithm of a ratio between the likelihoods of the signal and background hypotheses. In the expression, r is the signal strength (number of signal events divided by the number of expected signal events), and $\hat{\theta}$ represents the expected value of the nuisance parameters. This is used to compute two p-values, p_μ (signal+background hypothesis) and p_b (background-only hypothesis) and to define a confidence level (CL), given by

$$\mathrm{CL}_s = \frac{p_\mu}{1 - p_b} \quad . \tag{5.6}$$

This method will then output the expected upper limit, together with the observed limit in data. The method generates a number of toy MCs (pseudo-data histograms, sampled randomly from the MC distributions) and computes the limit for each of these toys, outputting in the end the mean and median values, together with the expected bands at 68% and 95% CLs (accounting for the statistical dispersion of the measurement).

The other method that was used is a multi-dimensional fit, *MultiDimFit*. This method performs, for a specific cross-section scenario, a multidimensional likelihood scan to fit several parameters of interest, in the case of this theses, the signal strength and the scaling factors $\mu_{t\bar{t}}$ and μ_{DY}.

Chapter 6

Analysis

6.1 Event selection

6.1.1 Central detector selection

Two charged leptons (electron or muon) with $p_T > 20$ GeV are required. Both have to be reconstructed within $|\eta| < 2.4$. At least one of the leptons is required to have $p_T > 30$ GeV and $|\eta| < 2.1$. Furthermore, the dilepton system is required to have an invariant mass above 20 GeV ($M_{ll} > 20$ GeV). Depending on the flavour and invariant mass of the dilepton system, the events are classified in the following exclusive categories:

- same flavour leptons (ee or $\mu\mu$) with reconstructed M_{ll} around the Z boson mass ($M_{ll} \in [76, 106]$ GeV): Z control region;
- same flavour leptons outside the Z-peak region: ee and $\mu\mu$ regions;
- opposite flavour leptons ($e\mu$): $e\mu$ region.

After categorising the events, the following selection is applied:

- $\geq$ 1 jet ($p_T > 30$ GeV, $|\eta| < 2.4$ passing a loose pileup jet id criteria [50]);
- $\geq$ 1 b-jet ($p_T > 30$ GeV, $|\eta| < 2.4$. The working point selected (deepCSV medium) provides a b tagging efficiency of about 68%, with a corresponding light-flavour misidentification rate of 1.1% and for c quark initiated jets of 12% [51]);
- at least one lepton-b combination verifies $M_{lb} < 160$ GeV.

Events failing these selection requirements are not excluded but categorised separately. In the last requirement, M_{lb} refers to the invariant mass of the lepton-b jet system. The b jet with the highest momentum is matched with the lepton more likely to have come from the same top quark. The criterion stems from the fact that, by energy conservation, one expects at leading order (LO), that $M_{lb} < \sqrt{m_t^2 - m_W^2} \approx 160$ GeV, for $m_t = 172.5$ GeV and $m_W = 80.4$ GeV [4]. Thus, by applying such requirement, we expect that higher $t\bar{t}$ purity is attained.

Associating the b-jet with the lepton from the same top decay

In order to make this association, I took two different approaches and compared the outcome. The first was to consider the combination that yields the lowest invariant mass. The second approach was to take the first b-jet and then find the closest lepton, i.e, the lepton with lowest angular distance ΔR with respect to it, where ΔR is given by $\sqrt{(\Delta\eta)^2 + (\Delta\phi)^2}$.

Figure 6.1 on the left shows the mass calculated through the first process versus the second.

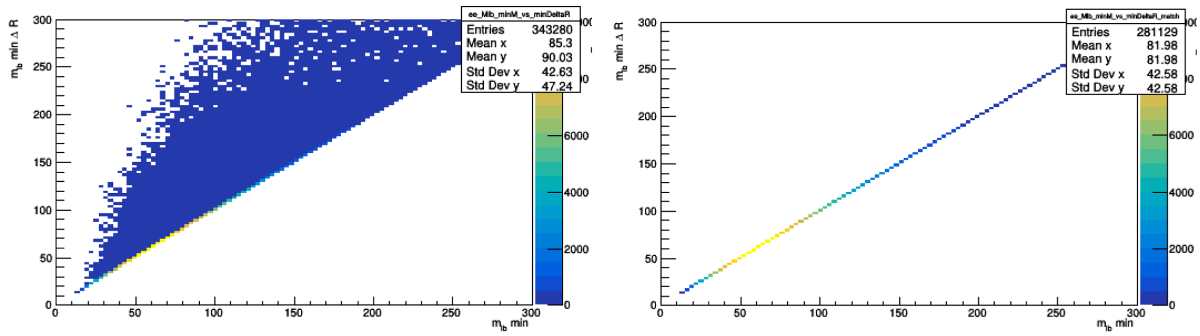

Figure 6.1: Left: Comparison between the M_{lb} calculated using the minimum mass value (x axis) and using the minimum $\Delta R(l,b)$ (y axis). Right: Events for which both methods yield the same resut.

One can see that the outcome is mostly the same. In fact, the majority of events lie along the diagonal. The plot on the right shows only the events that lie on the diagonal. By comparing the number of entries in the two, one verifies that 82% of the times, the same combination is picked by both methods. Therefore, the first approach was used, for simplicity, because it is expected to pick the correct combination in the great majority of the events, even though we cannot guarantee that the correct combination is picked for all events.

Control plots

Figure 6.2 shows the distribution of the invariant mass of the dilepton system for the ee, $\mu\mu$ and $e\mu$ categories. The same-flavour categories are dominated by Drell-Yan (DY) production. A clear peak is observed around the Z boson mass region, as expected. The opposite flavour category, however, is fairly pure in $\mathrm{t\bar{t}}$ events, although there is significant contribution from Multiboson and W production.

In order to increase this purity, the M_{lb} cut is applied. Figure 6.3 shows the distribution of the invariant mass of the dilepton system, for opposite flavour leptons ($e\mu$), but now for events with at least one b-jet, satisfying $M_{lb} < 160$ GeV. Comparing with the bottom plot of figure 6.2, one clearly sees the effect of the background rejection efficiency obtained after the Mlb cut is applied to the $e\mu$ events. Except for the ttbar process, all other backgrounds are heavily suppressed for signal and for background events, as well as for data. A good agreement is found.

Figure 6.4 shows the distribution of the b-tagging multiplicity. The number of b-jets produced in $\mathrm{t\bar{t}}$ events is at least two, due to the decay of the top and anti-top quarks. However, in the distributions we observe that a fraction of $\mathrm{t\bar{t}}$ events have 0 or 1 b-tagged jets. This is due to the b-tagging efficiency, about

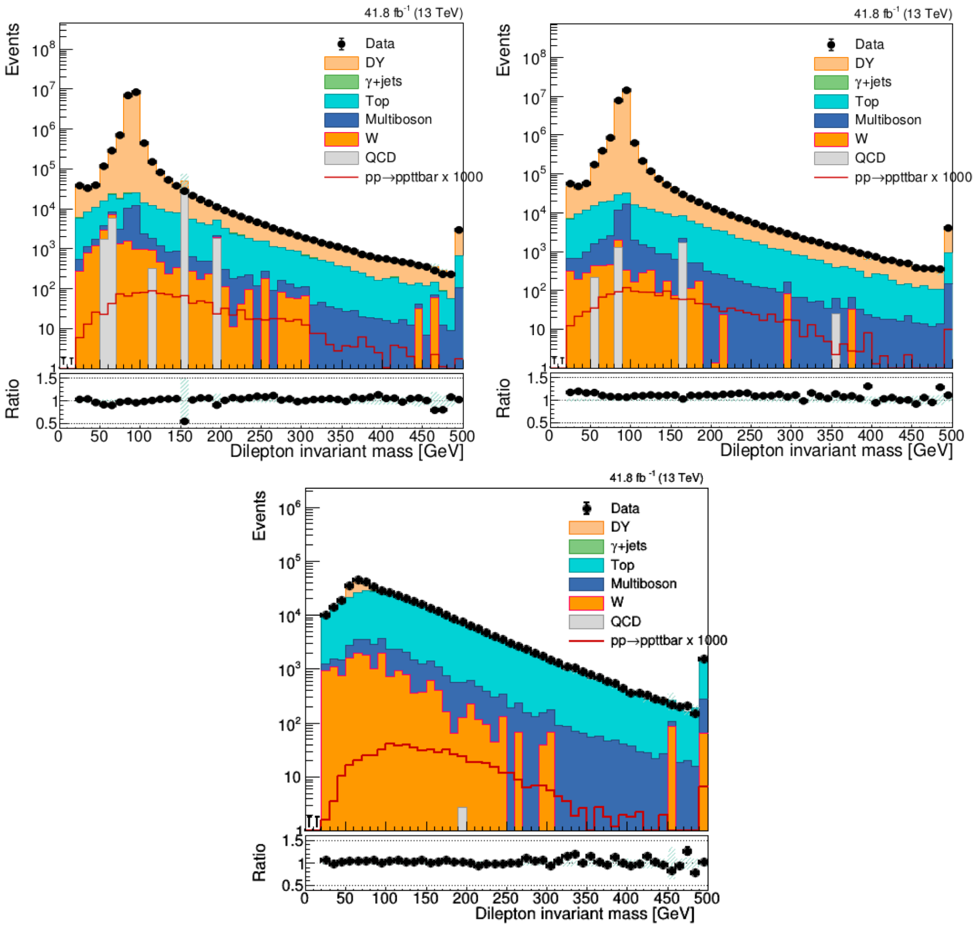

Figure 6.2: Distribution of the invariant mass of the dilepton system after selecting 2 leptons. Top left: ee, top right: $\mu\mu$, bottom centre: $e\mu$ channel.

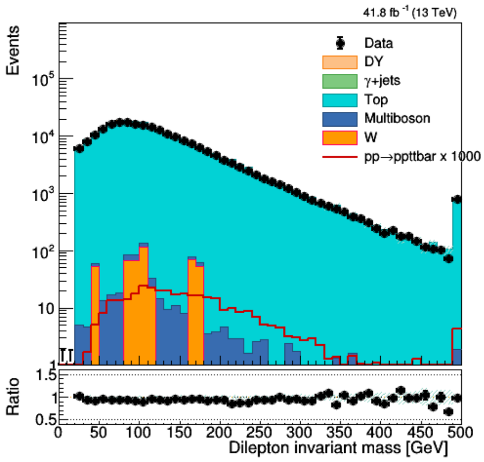

Figure 6.3: Distribution of the invariant mass of the dilepton system after selecting 2 leptons and ≥1 b and requiring $M_{lb} < 160$ GeV, for the $e\mu$ channel. The signal is normalised to a cross-section of 1 fb and multiplied by 1000, to make it visible in the distribution.

68%, as mentioned above. Even with this factor, it is still visible that top quark events (both inclusive and exclusive) have typically a higher number of b-tagged jets than the other background processes, as expected. A good data-MC agreement is observed.

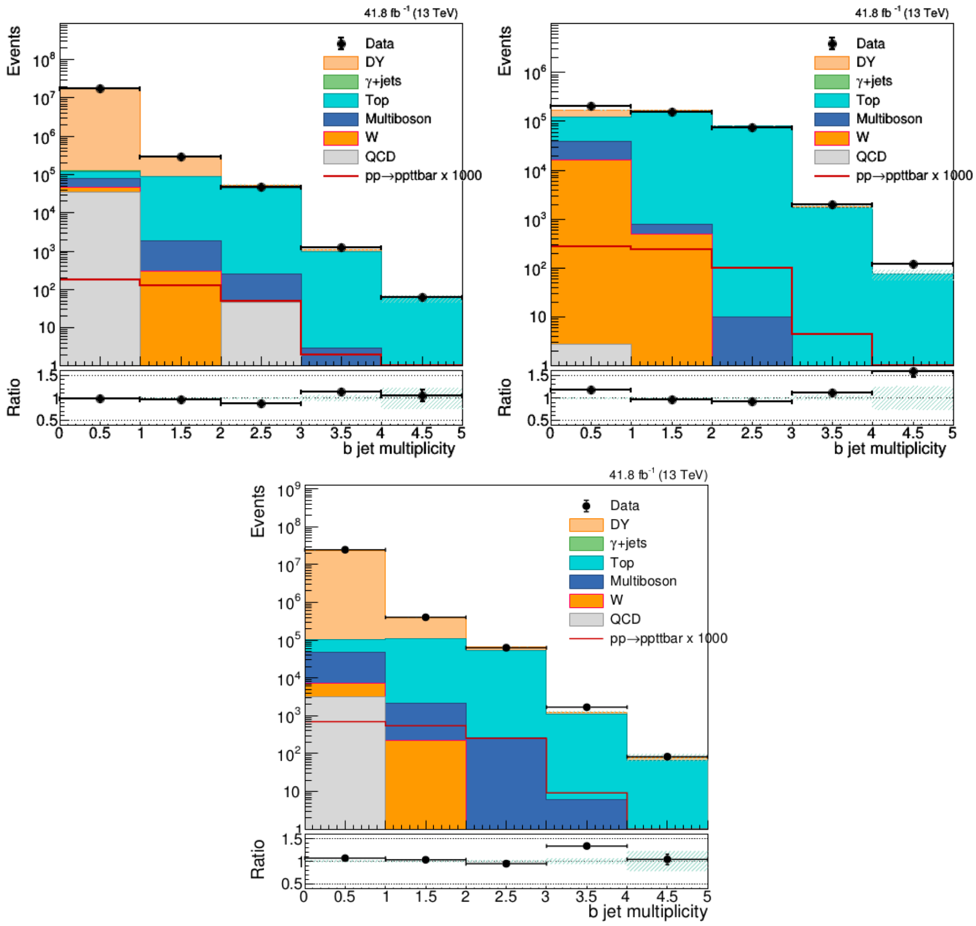

Figure 6.4: Distribution of the number of b-tagged jets after selecting 2 leptons. Top left: ee, top right: $\mu\mu$, bottom centre: $e\mu$ channel. The signal is normalised to a cross-section of 1 fb and multiplied by 1000, to make it visible in the distribution.

We compared the signal and the inclusive $\mathrm{t\bar{t}}$ sample concerning specific variables reconstructed in the central detector. The variables were chosen to be sensitive to the additional hadronic activity, which is expected to be suppressed in the case the production is exclusive and via electroweak vertices. The variables chosen are:

- $H_T = \sum_{j=1}^{N_j} |\vec{p}_{\mathrm{T,j}}|$, the scalar sum of the transverse momentum of all jets except the b-jets;
- Hadronic recoil $h = |\vec{p}_T^{miss} + \vec{p}_T(\ell_1) + \vec{p}_T(\ell_2) + \sum_{j=1}^{N_b} \vec{p}_T(j)|$, obtained from the sum of the missing transverse energy with the momenta of the two charged leptons and up to two b-jets. In the analysis, we make use of the so-called *puppiMET*[1] estimator for $\vec{p}_T^{miss}$ [53].

In the simulations we observe that signal $\mathrm{t\bar{t}}$ has a considerably small fraction of events which have extra activity: most of the events have H_T=0 (no extra jets above the p_T threshold in the event). Conversely signal $\mathrm{t\bar{t}}$ events tend to have lower h when compared to inclusive $\mathrm{t\bar{t}}$ production. Figure 6.5

[1] *puppi MET* is a missing transverse energy estimator that uses the PUPPI (Pileup per particle identification) algorithm [52] and accounts for additional contribution from pileup interactions.

shows the distribution of these variables in data and simulation. This feature could already be seen in figure 6.4, since there are less expected b-jets for signal than for inclusive $t\bar{t}$ background.

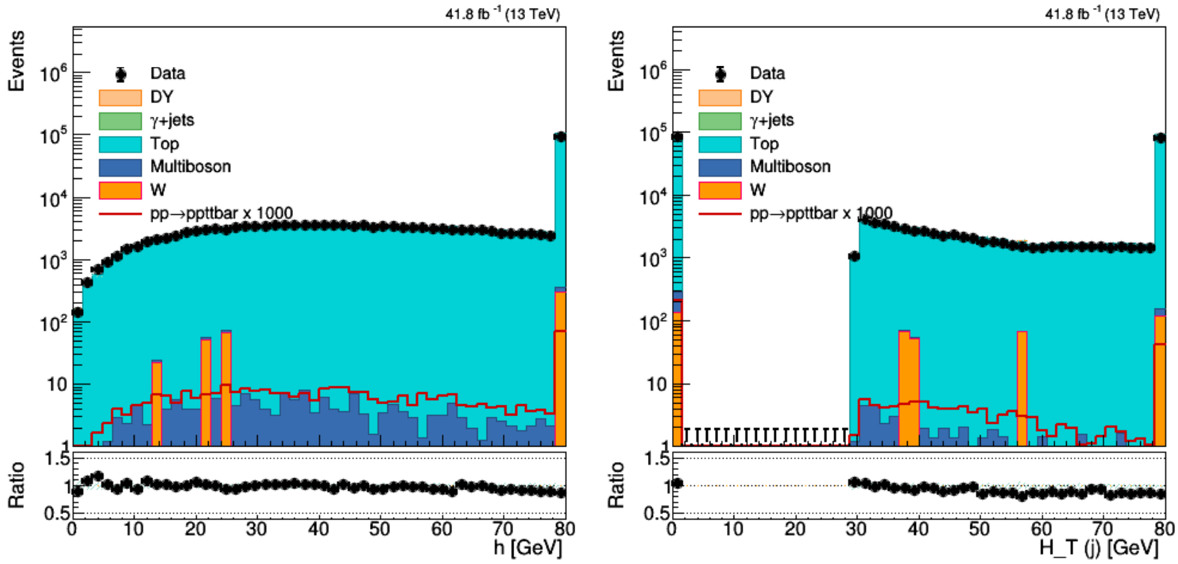

Figure 6.5: Hadronic activity distributions obtained after requiring 2 leptons, 1 jet, 1 b-jet, M_{lb} <160 GeV and opposite flavour leptons. The hadronic recoil h (left) and H_T (right) are shown. The signal is normalised to a cross-section of 1 fb and multiplied by 1000, to make it visible in the distributions.

In fact, requiring $H_T = 0$ GeV preserves 63% of exclusive $t\bar{t}$ (signal) events and only 22% of inclusive $t\bar{t}$ (background). In this analysis, $H_T = 0$ GeV is used to define the signal region.

Another variable that I found to be important is $\Delta R(l,l)$. One can see by looking at the distribution in figure 6.6 that, as expected, the exclusive $t\bar{t}$ events have a sharper peak around $\Delta R(l,l) \approx 3$. This corresponds to leptons emitted in opposite directions (back-to-back) with low pseudorapidity.

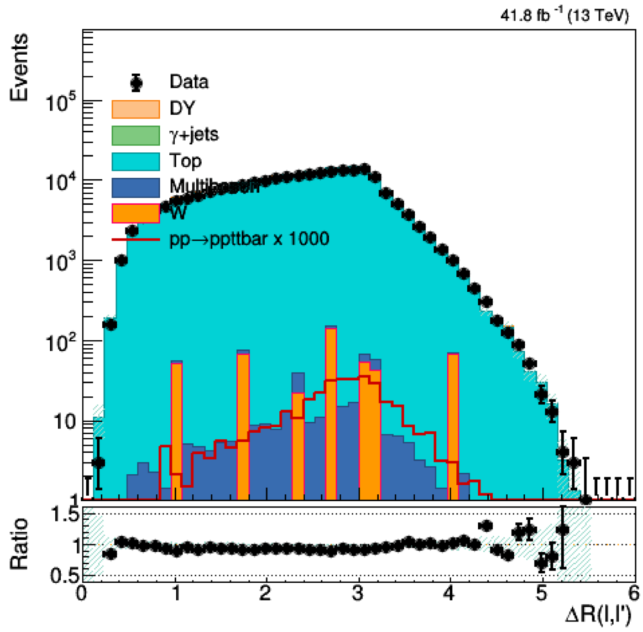

Figure 6.6: Distribution of the ΔR between the two leptons, after selecting 2 leptons and ≥1 b and requiring $M_{lb} < 160$ GeV, for the $e\mu$ channel. The signal is normalised to a cross-section of 1 fb and multiplied by 1000, to make it visible in the distribution.

6.1.2 PPS detector selection

For the final selection, we use data from the pixel detectors. The pixels have an associated efficiency, which depends on the RP and on the data-taking period. This efficiency is in general close to 1 (within 10%) for mid and high ξ's, but for for small ξ values (ξ <0.04) it can be as low as 0.5. This is accounted for by scaling the signal MC. As the efficiency is time-dependent, we compute the average efficiency as a function of ξ for each arm, by taking the efficiency for each data-taking period and weighting by the luminosity. We then apply these averages as weights for the MC.

For each track reconstructed in the pixel detector, one is able to reconstruct the fractional momentum loss (ξ) of the proton. In front of the RPs, a collimator is installed, to reduce the hits of protons from the beam halo, that would heavily damage the detectors. Due to the presence of this collimator, the detector acceptance is reduced and fiducial cuts must be applied, to ensure that the reconstructed protons are within the collimator acceptance. The recommended fiducial cuts applied are $0.015 < \xi < 0.12$ for arm 0, and $0.025 < \xi < 0.16$ for arm 1.

The ξ distribution for each pixel is shown in figure 6.7, for signal and for data. The vertical dashed orange lines represent the fiducial cuts applied. Looking at the data points, one can notice the asymmetric acceptance of the RPs.

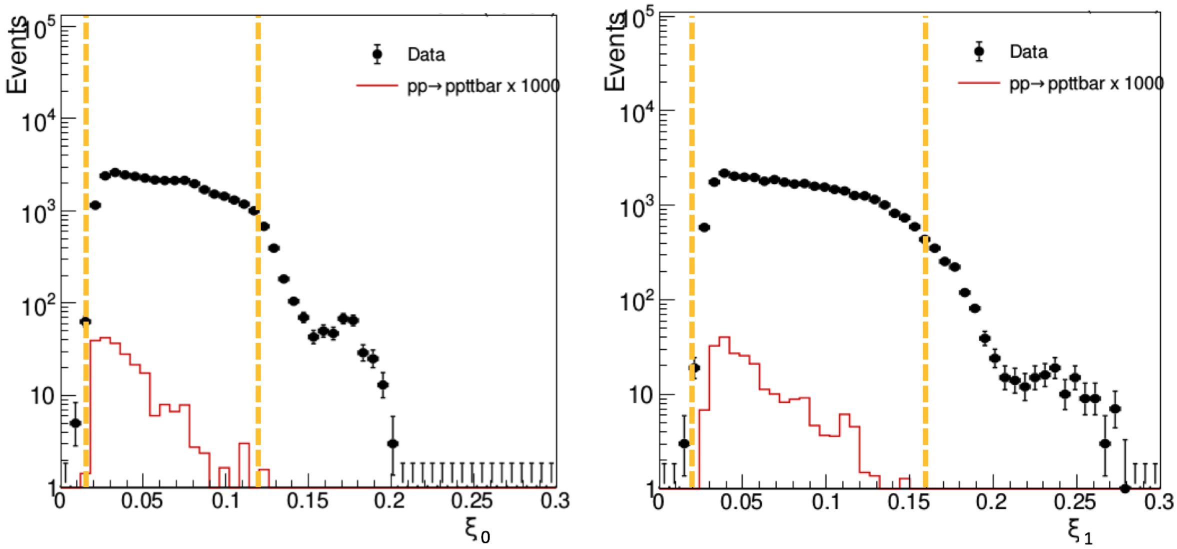

Figure 6.7: Distribution of the fractional momentum loss (ξ) of the protons detected in the pixels, for RP023 (left) and RP123 (right), for data and signal simulation. The orange lines represent the fiducial cuts due to detector acceptance.

From the values of ξ, one can reconstruct the mass and rapidity of the $t\bar{t}$ in the central system, using equations 3.11 and 3.12.

Due to pileup (the average vertex multiplicity in the 2017 data is ~30), there is often more than one track per event in each pixel detector. Thus, there is the need to reconstruct the mass and rapidity for every combination of tracks. In this analysis, we selected events in the $M_{RP} \in [300, 600]$GeV range, which is chosen to be compatible with the bulk of the production threshold of exclusive $t\bar{t}$. The choice for the correct combination is given by the combination that yields the lowest mass. The events are categorised depending on whether or not there is a combination of tracks that leads to a reconstructed $t\bar{t}$mass in this range.

PPS information is only available for data and simulated signal sample; the official 2017 MC samples used for the background do not contain this information. In order to circumvent this problem, I use a data-driven method to attribute a "fake" PPS information to the MC samples. For that, I take the number of forward tracks and the ξ distributions from data (as observed at pre-selection level where possible contribution from the signal is negligible), and attribute, to each MC event, a number of tracks, randomly picked from the distribution, as well as a random ξ value for each track (according to the distribution and within the acceptance of the RPs), and then compute the mass and rapidity using equations 3.11 and 3.12. This method for modelling the background assumes no significant correlations between the number of tracks in the event and the values of ξ. However, it was verified that this assumption led to a slope in the data-MC ratio, in the distributions of the mass and rapidity of the two protons.

In order to eliminate this source of mismodelling and allow the setting of meaningful limits, it was required that events have only one track on each side of PPS (it was decided that events with multiple tracks were not considered for the forward selection). This procedure eliminates, on the one hand, the systematic error introduced by trying several combinations and choosing the lowest mass, and on the other hand, the correlations mentioned above. One clear disadvantage is the loss of signal efficiency, since many of the signal events, which have several tracks in PPS, are discarded. This is again accounted for by scaling the signal MC. As a result, the plots for the pp mass and rapidity were obtained, and they are shown in figure 6.8.

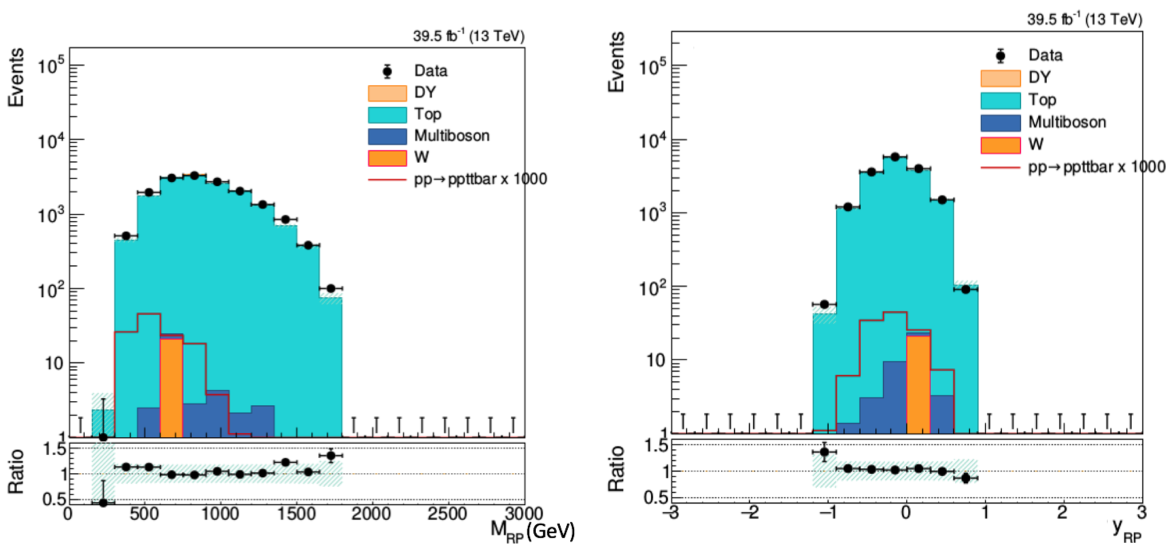

Figure 6.8: Distribution of the reconstructed mass (left) and rapidity (right) of the two-proton system in the RPs, when requiring 2 leptons of opposite flavour, 1 jet, 1 b-jet, low mass of the lepton/b-jet system, and 1 track on each side of PPS.

One can observe that a good data/MC agreement is obtained. As a slight disagreement is still found for some particular bins, an additional systematic error of the method was introduced. The systematic was taken as 15%, as this covers the maximum observed discrepancy from data.

	Pre-selection			$76 < m_{ll} < 106$ GeV (outside Z peak)			$\geq$ 1b		
	ee	$e\mu$	$\mu\mu$	ee	$e\mu$	$\mu\mu$	ee	$e\mu$	$\mu\mu$
qcdTT	160004±710	299084±960	195047±830	124958±610	299084±960	152827±730	93311±590	224194±840	114386±610
DY	16725545±7000	47294±328	21899990±8120	1316392±2490	47294±328	1504421±2720	19286±430	1027±74	23413±535
others	78969±1520	38765±1562	47746±2926	55944±25480	38765±1562	18870±2422	569±305	383±210	292±113
total	16964518±25240	384940±1610	22140655±9260	1492854±24240	384940±1610	1671280±3360	113116±700	226732±840	138714±820
signal	1147	2037	1431	946	2037	1159	480	1129	623
data obs.	17396913	431794	25004777	1552878	431794	1968104	112933	231811	150549

Table 6.1: Yields of expected and observed events, at pre-selection level, as well as after selecting events outside the Z peak region, and after requiring ≥1b-tagged jet. The uncertainties shown for the MC include the statistical uncertainty only.

	$M_{lb} < 160$ GeV			$H_T = 0$			$300 < m_{RP} < 600$ GeV		
	ee	$e\mu$	$\mu\mu$	ee	$e\mu$	$\mu\mu$	ee	$e\mu$	$\mu\mu$
qcdTT	92574±509	222576±840	113548±610	30510±270	75248±470	38277±320	300±32	650±50	359±37
DY	16939±421	868±74	20497±426	10807±295	572±53	13101±520	127±29	2±2	144±36
others	509±187	320±208	238±71	206±66	213±138	123±57	2±1	1±1	1±1
total	110500±700	224879±840	134902±810	41827±450	76713±470	51875±450	429±44	653±50	504±56
signal	479	1119	619	304	680	374	21	42	16
data obs.	109242	229091	145571	44459	85998	60896	470	926	598

Table 6.2: Yields of expected and observed events outside the Z peak region with ≥1b-tagged jet, after selecting $M_{lb} < 160$ GeV, $H_T = 0$ and $m_{RP} \in [300, 600]$ GeV. The uncertainties shown for the MC include the statistical uncertainty only.

The tables 6.1 and 6.2 show the event yields after applying, in sequence, each of the event selection cuts. There is an overall slight excess of data, when compared to the MC prediction. This is yet to be investigated, however a possible source for the discrepancy is the normalisation being applied to the DY MC samples, which has to be updated. Some extra control plots of other kinematic variables can be found in Appendix B.

PPS background determination

The most important background is due to non-exclusive $t\bar{t}$ events combined with random pileup protons that are detected in PPS. This background is estimated using the data-driven method explained above. The method results in a background m_{RP} distribution. From this distribution, the fraction of events that have a mass reconstructed in the RPs, m_{RP}, between 300 and 600 GeV, i.e. $m_{RP} \in [300, 600]$ GeV cut is computed, and the ”fake rate” is determined to be ≈11%, with negligible statistical uncertainty. The result is similar for the ee, $\mu\mu$ and $e\mu$ final states and for events with m_{ll} around the Z peak. A scheme of the method used is shown in figure 6.9.

6.1.3 Matching the central and the forward kinematics

A further improvement in the S/B ratio may be achieved by matching the kinematics of the events reconstructed in the central and in the PPS detectors.

However, as the $t\bar{t}$ dilepton final state is being used, two neutrinos will be present in the event, and the full reconstruction of the central system is not trivial. In the following section, the methods to overcome this difficulty are described.

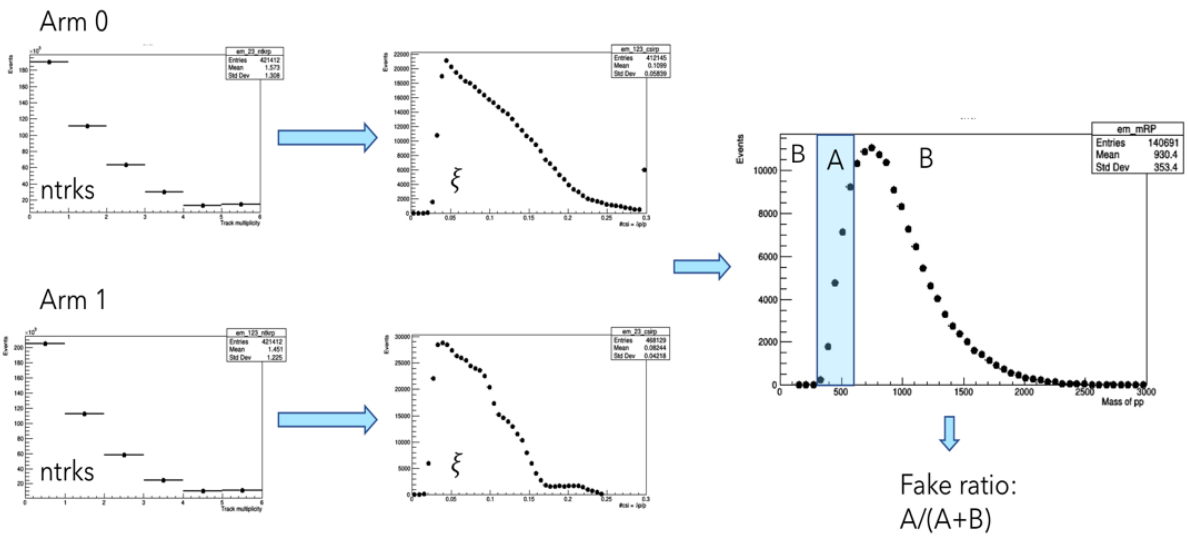

Figure 6.9: Scheme showing the procedure for computing the fake rate. For a given number of simulated events, one generates a random number of tracks in each arm of PPS, according to the data distributions. Then, for each track, a random ξ value is generated (also according to the probability of the distributions). The pp mass (M_{RP}) is then reconstructed from the two random tracks in the two opposite PPS arms, and the fraction of times that it falls within the [300,600] GeV range yields the fake rate.

Reconstructing the central system

We apply the algorithm described in [54] to reconstruct the kinematics of the central system for the selected events. The algorithm is applied to the events which pass the full central selection described earlier, with the additional requirement of at least 2 b-tagged jets. It takes as inputs the 4-momenta of the 2 leptons and 2 b-jets and the missing transverse energy, and using linear algebra, it reduces the possible solutions for neutrino momenta to a discrete set. Given the ambiguity in the pairing of the leptons with the b jets, and in reconstructing the kinematics of the two outgoing neutrinos, up to 8 solutions can be found per event. Two variables are reconstructed: the invariant mass and the rapidity of the $t\bar{t}$ system, $M_{t\bar{t}}$ and $y_{t\bar{t}}$, respectively. We choose the solution that yields the lowest $M_{t\bar{t}}$. The performance of this algorithm was tested by computing the resolutions of the reconstructed $M_{t\bar{t}}$ and $y_{t\bar{t}}$ values, using simulated $t\bar{t}$ events. For these events, 2D plots comparing the invariant mass and rapidity of the $t\bar{t}$ pair at generator level and the ones reconstructed by the algorithm were produced, as shown in figures 6.10 and 6.11, for $M_{t\bar{t}}$ and $y_{t\bar{t}}$, respectively. The three 2D plots that can be seen in each figure compare the reconstruction for ee, $\mu\mu$ and $e\mu$ samples. In Fig. 6.10 and Fig. 6.11 (bottom right), for all samples together, plots of the difference between the generated and reconstructed quantities is shown. Gaussian functions are used to perform a fit, and a resolution of 15.5 ± 0.5% is obtained for $m_{t\bar{t}}$. It should be noted that the shape of the distribution is not truly gaussian, there is a clear tail, but for computing the resolution this fit is sufficient. This tail is most likely a result of pileup, missing transverse energy resolution and/or jets that do not originate from a top quark.

For the rapidity, $y_{t\bar{t}}$, the standard deviation is measured to be 0.228 ± 0.006, but as one cannot divide by the rapidity value, which is sometimes 0, it does not correspond directly to a resolution. However, for the sake of comparison, this is sufficient to conclude whether the resolution will increase or decrease.

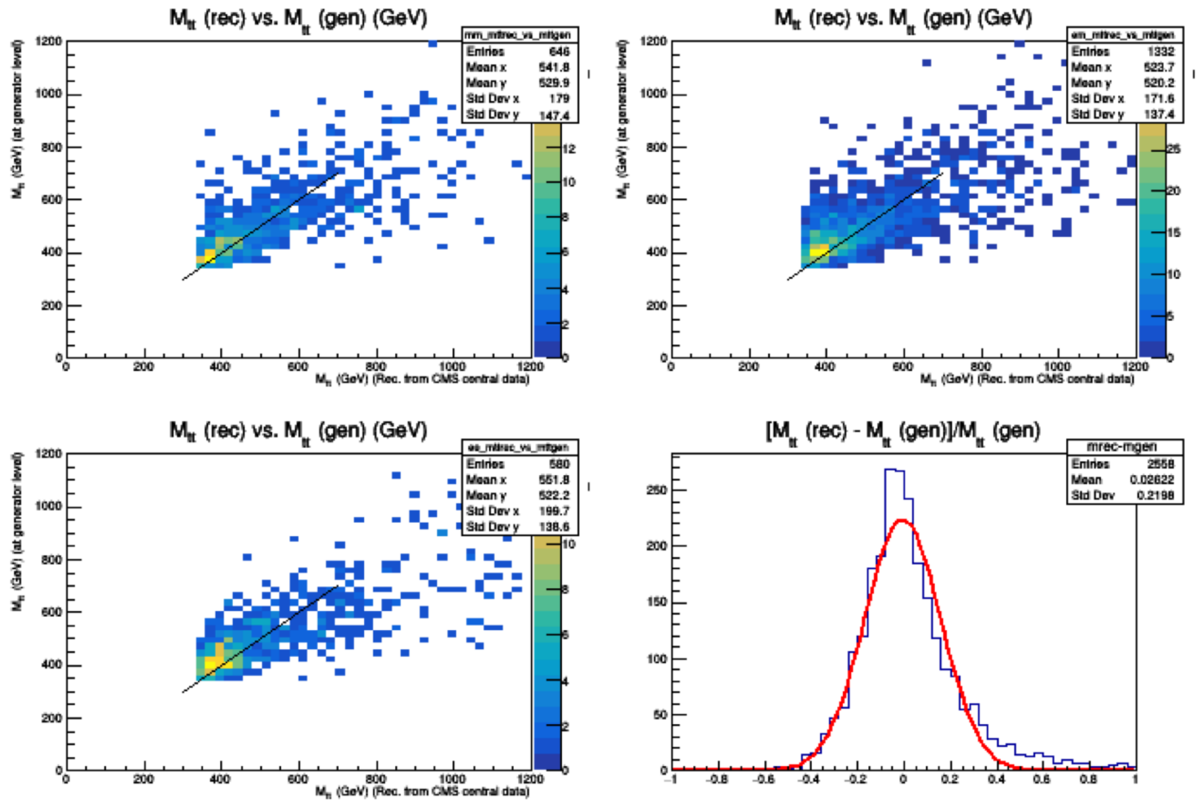

Figure 6.10: Distributions of the invariant mass of the $t\bar{t}$ pair at generator level versus the one reconstructed by the algorithm were produced for ee (top left), $\mu\mu$ (top right) and $e\mu$ (bottom left) samples. On the bottom right plot, the difference between the generated and reconstructed mass is shown, for all channels together. A Gaussian function is fitted, and a resolution of $15.5 \pm 0.5\%$ is obtained.

The algorithm performs according to expectations, in the sense that the distributions are well centred at 0. In order to improve the correlation between the generated and reconstructed quantities, a Multivariate Analysis method was used. We took advantage of the Regression capabilities of ROOT's TMVA. The goal was to improve the resolution of the reconstruction, by training Boosted Regression Trees to regress the true value of $M_{t\bar{t}}$ and $y_{t\bar{t}}$ and give as output a correction factor for each event. The following 21 input variables were used:

- Rec. $m_{t\bar{t}}$: output of the algorithm reconstruction (mass)
- Rec. $y_{t\bar{t}}$: output of the algorithm reconstruction (rapidity)
- M_{ll}: invariant mass of dilepton system
- ΔR_{ll}: ΔR between the two leptons
- $\Delta\phi_{ll}$: azimuthal angle difference between the two leptons
- Number of light jets
- Number of b jets
- Missing transverse energy
- 4-momentum of lepton 1
- 4-momentum of lepton 2
- 4-momentum of b-tagged jet 1
- 4-momentum of b-tagged jet 2

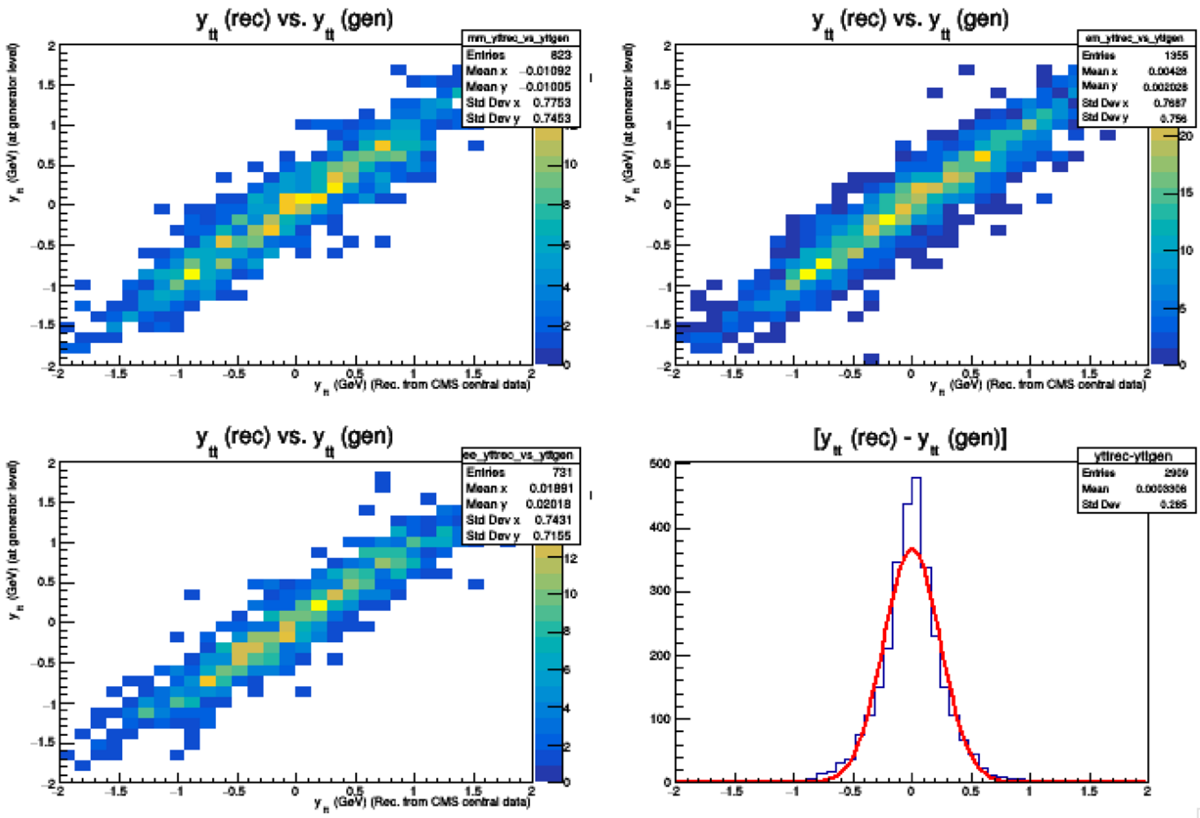

Figure 6.11: Distributions of the rapidity of the $t\bar{t}$ pair at generator level versus the one reconstructed by the algorithm were produced for ee (top left), $\mu\mu$ (top right) and $e\mu$ (bottom left) samples. On the bottom right plot, the difference between the generated and reconstructed rapidity is shown, for all channels together. A Gaussian function is fitted and a standard deviation of 0.228 ± 0.006 is obtained.

RAPIDITY (y)	Mean	σ
Before regression	-0.008±0.006	0.228±0.006
After regression	-0.005±0.004	0.167±0.004
IMPROVEMENT	-	27%

Table 6.3: Comparison of the means and standard deviations of the fit to ($y_{t\bar{t}}$ reconstructed - $y_{t\bar{t}}$ generated), before and after using the regression technique, and the improvement obtained.

- M_{lb}: invariant mass of b-jet lepton system
- $p_x^2 = (p_x(b_1) + p_x(b_2) + p_x(l_1) + p_x(l_2) + p_x(\not{E}_T))^2$
- $p_y^2 = (p_y(b_1) + p_y(b_2) + p_y(l_1) + p_y(l_2) + p_y(\not{E}_T))^2$
- $p_z^2 = (p_z(b_1) + p_z(b_2) + p_z(l_1) + p_z(l_2) + p_z(\not{E}_T))^2$
- $E^2 = (E(b_1) + E(b_2) + E(l_1) + E(l_2) + p_T(\not{E}_T))^2$
- $y_{vis} = y(b_1 + b_2 + l_1 + l_2)$: rapidity of visible particles
- $y_{sum} = |y(b_1)| + |y(b_2)| + |y(l_1)| + |y(l_2)|$: sum of the absolute values of rapidity of each visible particle
- $min_{\Delta y} = min(|y(b1 + l1)| - |y(b2 + l2)|)$
- $max_{\Delta y} = max(|y(b1 + l1)| - |y(b2 + l2)|)$

As for the target of the regression, $rec_{m_{t\bar{t}}}/gen_{m_{t\bar{t}}}$ was used for $M_{t\bar{t}}$, and $rec_{y_{t\bar{t}}} - gen_{y_{t\bar{t}}}$ for $y_{t\bar{t}}$. This means that the Regression Trees will learn how to regress these values from the input variables.

The training is done on simulated background $t\bar{t}$ events, while the testing is done both on simulated signal and background $t\bar{t}$ events. The output of the testing is a ROOT Ntuple which has all the information of the relevant variables, as well as the $M_{t\bar{t}}$ reconstructed by the algorithm and the correction output by the MVA method. If one compares the corrected and uncorrected values of mass and rapidity, the plots of figure 6.12 are obtained. A comparison between resolutions before and after corrections is shown in tables 6.3 and 6.4. One can observe that the relative improvements are approximately 21% and 27% for $M_{t\bar{t}}$ and $y_{t\bar{t}}$, respectively. It is a significant improvement, and therefore the regressed mass and rapidity will be used as inputs in the MVA analysis.

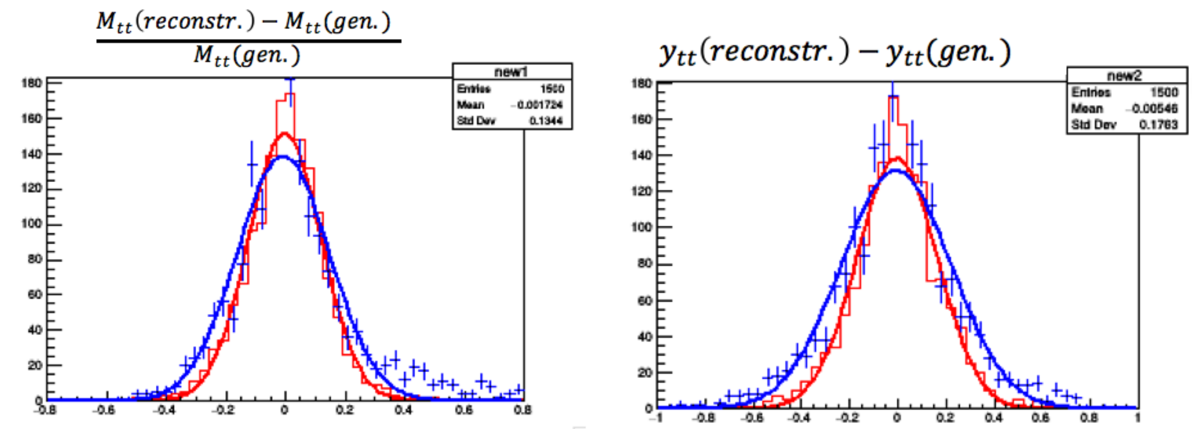

Figure 6.12: Resolution of the mass (left) and rapidity (right) reconstruction - blue: using the algorithm, red: using the algorithm + regression technique

In figure 6.13, it is possible to see, for signal simulation, the comparison between the centrally reconstructed mass and rapidity and the ones measured by PPS, before and after regression, for the signal

MASS (m)	Mean	σ
Before regression	-0.008±0.004	0.155±0.005
After regression	-0.002±0.003	0.123±0.003
IMPROVEMENT	-	21%

Table 6.4: Comparison of the means and standard deviations of the fit to ($M_{t\bar{t}}$ reconstructed - $M_{t\bar{t}}$ generated)/$M_{t\bar{t}}$ generated, before and after using the regression technique, and the improvement obtained.

simulation. The correlation, which is already visible before applying the regression, is visibly improved.

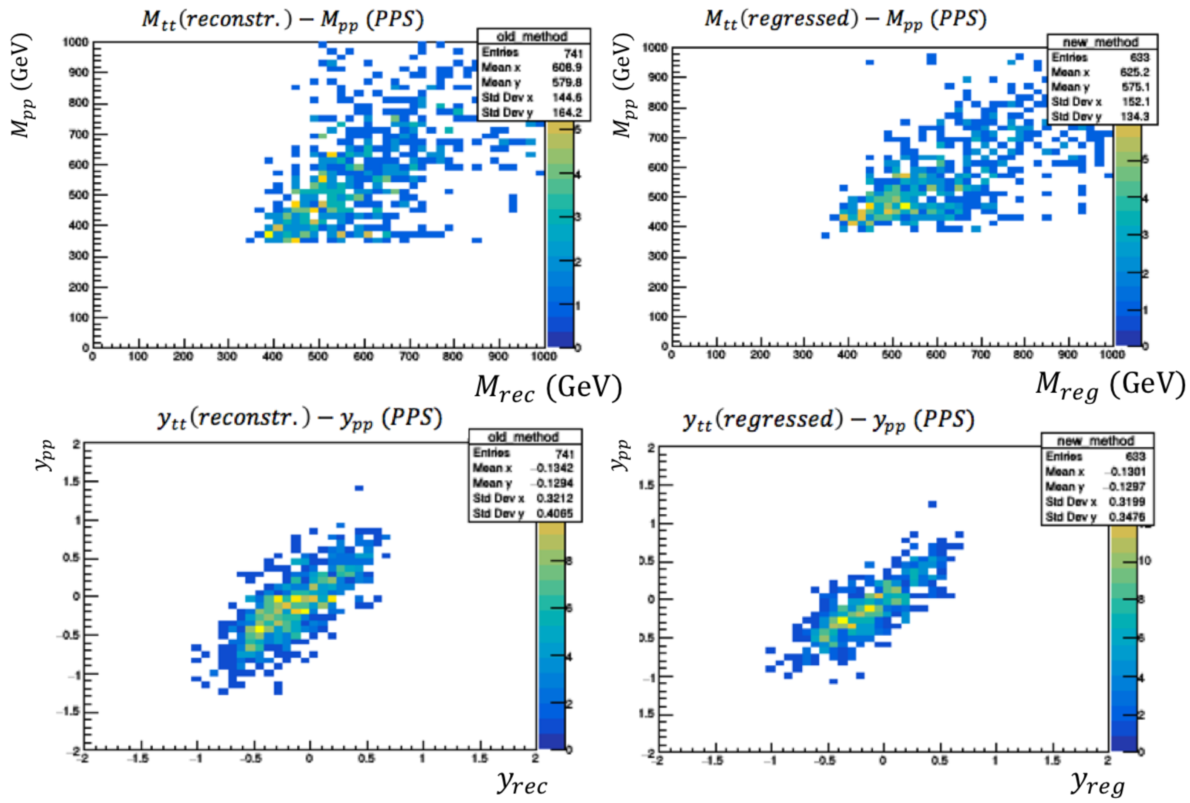

Figure 6.13: Comparison of the $M_{t\bar{t}}$ (top) and $y_{t\bar{t}}$ (bottom) centrally reconstructed and those measured by PPS, for simulated signal events: before regression (left) and after regression (right).

6.2 Determination of Roman Pots acceptance

In order to estimate the detector acceptance of the RPs for the $pp \to pt\bar{t}p$ signal, the sample generated with FPMC+Herwig has been used. A 2D distribution of the mass as a function of the rapidity of the simulated $t\bar{t}$ system is shown in Fig. 6.14 (top), requiring 2 leptons in the final state. Then, a cut is applied by selecting only events for which the forward protons could be reconstructed in PPS (Fig. 6.14, bottom). From these distributions, one simply divides the number of surviving events by the initial number of all simulated events. The acceptance of the RPs is then measured to be (31±2)%.

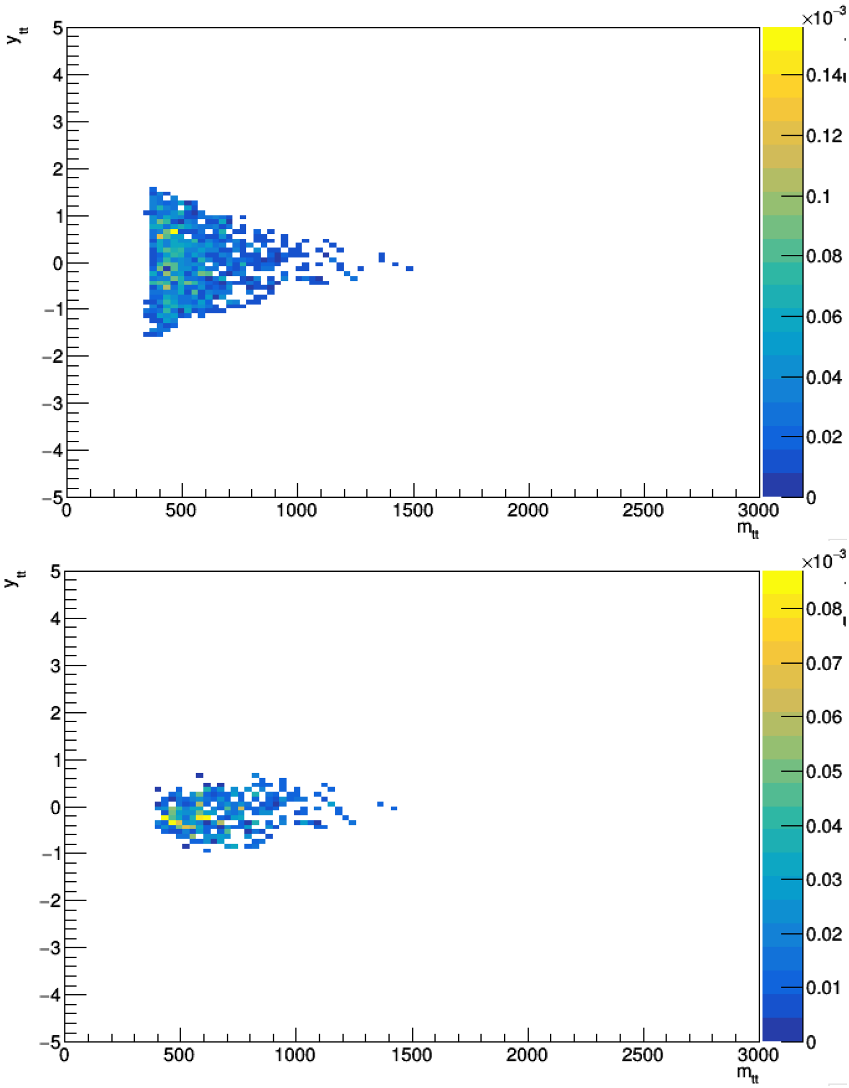

Figure 6.14: 2D distributions of the mass (m_{RP}) versus rapidity (y_{RP}) of the $t\bar{t}$ system in the signal sample, for the $e\mu$ final state (results are similar for other final states) after requiring 2 leptons (top), and after requiring also that the tracks are within the RP acceptance (bottom).

	Surviving events	
Simulated events with 2 leptons	1259	100%
Events in RP acceptance	391	(31±2)%

Table 6.5: RP acceptance: number of events surviving the cut requiring PPS tracks to fall within the RP acceptance, and their corresponding fractions.

6.3 Selection using BDT classifier

For training the BDTs, inclusive $t\bar{t}$ (background) and exclusive $t\bar{t}$ (signal) simulated events are used. Several training parameters were tested, and the ones that resulted in the highest discriminating power while avoiding overtraining were used in the final classification. These parameters are summarised in table 6.6.

	Option	Description
NTrees	50	Number of trees to train
BoostType	AdaBoost	Adaptative Boost (see sec. 5.2.2)
SeparationType	GiniIndex	Separation criterion for node splitting
nCuts	20	Number of steps during node cut optimisation

Table 6.6: Training parameters of the BDT.

As a first approach, all the available kinematical variables were used for the training. However, it was verified that most of them were not being used by the classifier, since they were fully correlated with other variables. The excess of variables being used for training in the signal sample (private production with few events) was causing overtraining. After a few iterations, the 13 variables which were found to be more discriminating were, in order of discriminating power:

1. M_{pp}
2. y_{pp}
3. M_{tt} (after regression)
4. y_{tt} (after regression)
5. y_{vis} (defined in section 6.1)
6. ΔR_{ll}
7. m_{ll}
8. p_y^2 (defined in section 6.1)
9. $\phi(b_2)$ (azimuthal angle of the sub-leading b-tagged jet)
10. y_{sum} (defined in section 6.1)
11. $min_{\Delta y}$ (defined in section 6.1)
12. M_{lb} (defined in section 6.1)
13. $\eta(b_2)$ (pseudorapidity of the sub-leading b-tagged jet)

The normalised distributions for signal and background of each of this variables are shown in appendix B, in figure B.3. The linear correlation coefficients, in percentage, between these variables, for signal and for $t\bar{t}$ background, are shown in figure 6.15. The correlation matrices are a good way to visualise the differences in the correlation between each pair of input variables for signal and for background. In general, a small correlation between the variables (off-diagonal) is found, with some meaningful exceptions. We can see that some variables are heavily correlated for the background, but not for the signal, and vice-versa, and the trees will learn how to take advantage of these differences to define the cuts. If there were any variables which were heavily correlated (close to 100%) both for signal and for background, then these would not have a high discriminating power and could be removed. This, however, is not the case for any of the variables shown.

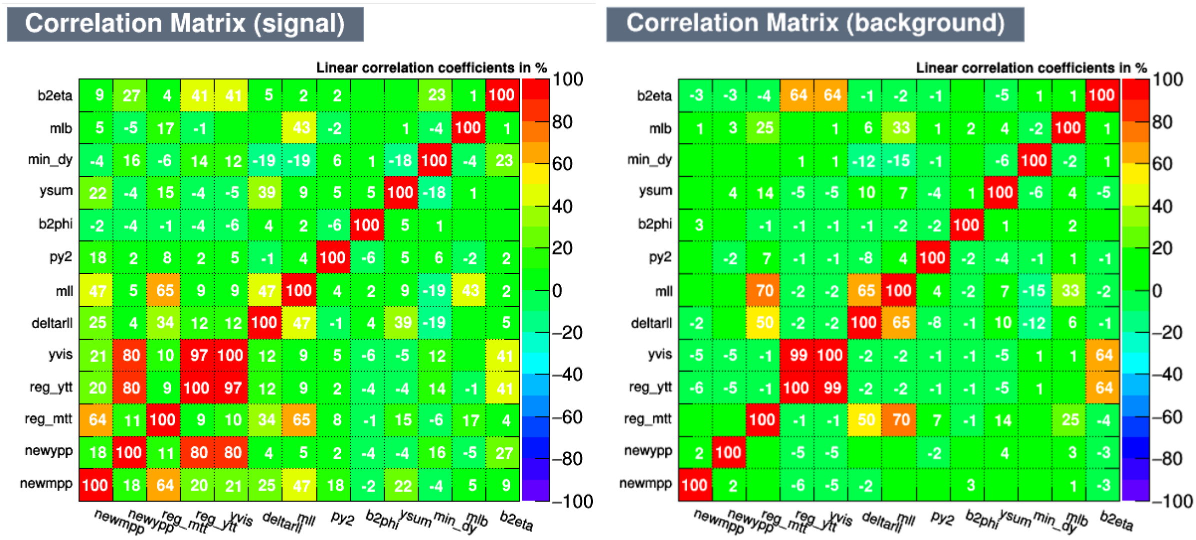

Figure 6.15: Correlation matrices, showing the linear correlation coefficient between all pairs of variables, for signal and background (see text). The correlation coefficients are shown in percentage, from -100 to 100, where 0 means no observed correlation, 100 means fully correlated and -100 means fully anti-correlated.

Looking at the matrices, we can see that for the signal there is a high correlation between the forward variables (M_{pp} and y_{pp} (designated *newmpp* and *newypp* in the correlation matrices in Fig. 6.15), and the central $t\bar{t}$ kinematics (regressed $M_{t\bar{t}}$ and $y_{t\bar{t}}$, *reg_mtt* and *reg_ytt* in the matrices), but not for the background. This is expected, because for the signal the two leading protons are the ones that are connected to the exchange generating the $t\bar{t}$ pair, and thus the invariant mass and rapidity should be heavily correlated (64% for mass and 80% for rapidity), while for the background, these protons are from pileup, and are completely uncorrelated from the central system (0% for mass and -5% for rapidity).

The output of the classifier, comparing training and test samples, can be seen in figure 6.16. As explained earlier, it is evident from the figure that events that are more ”signal-like” will be attributed a larger BDT output (closer to 1), while ”background-like” events will be classified with a low BDT output (closer to -1). We can also see that the training and test samples generally agree in terms of distribution, and there is no overtraining. TMVA performs a series of Kolmogorov-Smirnov (K-S) tests comparing the training and test sets and outputs the average result for signal and for background. The K-S test is a statistical test which compares two distributions (in this case, the training and test distributions), evaluating how much they agree with each other. For random samples, the test should output a uniform distribution between 0 and 1, and therefore the average should be 0.5. In practice, it is difficult to obtain precisely 0.5 with limited statistics, so we consider that there is no overtraining if the test result is of the order of 0.5 and it is visually apparent that the two distributions agree. This is true for the background. The simulated signal sample has a small number of events passing the selection cuts, which is not enough to optimally train the classifier. That is why the agreement for signal is not perfect and the K-S test result is low. However, this was not considered to be problematic, since the distributions seem to agree reasonably.

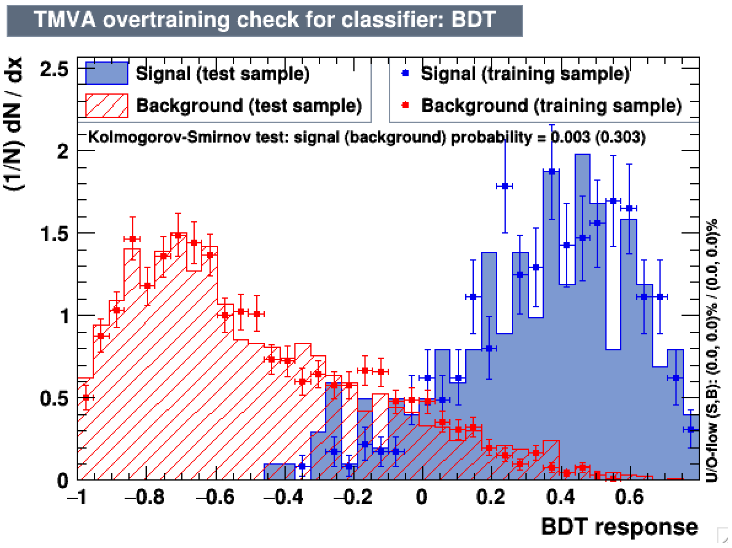

Figure 6.16: Comparison between training and test samples, in terms of the response of the BDT classifier, in order to check for agreement between samples and evaluate if there was overtraining. The training and testing are done using the simulated signal and $t\bar{t}$ background samples. The disagreements found in the signal samples are caused by the very low statistics.

The output weights are then applied to the full data and simulation, and the distribution obtained is shown in figure 6.17. The separation between signal and background is visible in the distribution, and this is what will be used in the definition of signal and control regions in the statistical analysis described in the next section. One must keep in mind, however, that the background is overwhelmingly large, and therefore the signal region will still be quite rich in background events.

6.4 Determination of $\sigma(\mathrm{pp} \to \mathrm{t\bar{t}pp})$ through a statistical analysis

6.4.1 Cut-based selection

The events are classified in 5 categories, according to central and forward kinematic variables. The different Signal Regions (SR) and Control Regions (CR) categories share in common the selection of $\geq$ 2 leptons with M_{ll} >20 GeV. The specific requirements of the final event categories are the following, for the different ee, $\mu\mu$, $e\mu$ final states:

SR_$e\mu$ - $e\mu$ events with ≥ 1b, low M_{lb}, $M_{RP} \in [300, 600]$ GeV and $H_T = 0$ GeV;

SR_ee - similar to SR_$e\mu$ for ee events outside the Z peak;

SR_$\mu\mu$ - similar to SR_$e\mu$ for $\mu\mu$ events outside the Z peak;

$\mathrm{t\bar{t}}$**CR**_$e\mu$ - $e\mu$ events with ≥ 1b, low M_{lb} and failing the $M_{RP} \in [300, 600]$ GeV cut;

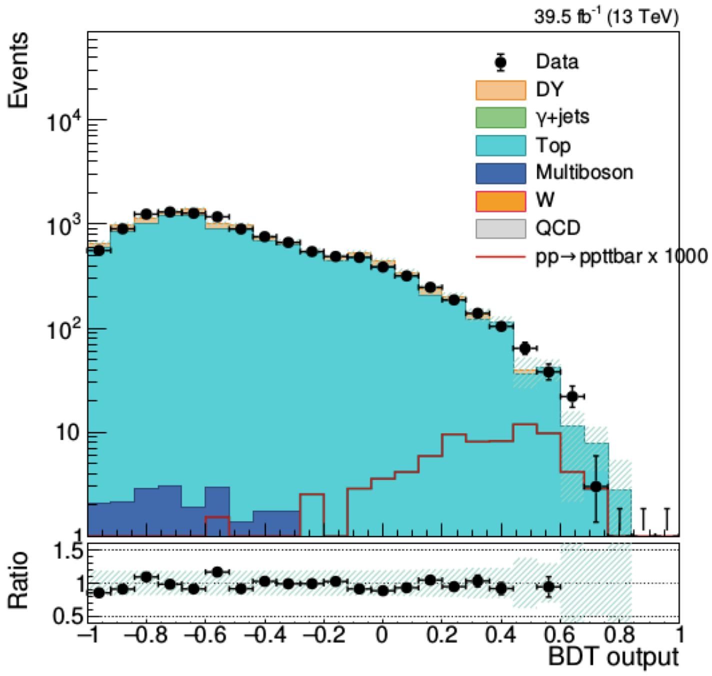

Figure 6.17: Output of the BDT classifier, when applied to the full data and MC samples (all decay channels, ee, $e\mu$ and $\mu\mu$, together). One can observe the separation between signal and background works as expected, with signal events clustering at larger BDT output values and background events in lower BDT output values. The signal is normalised to a cross-section of 1 fb and multiplied by 1000, to make it visible in the distribution.

t$\bar{\text{t}}$CR_ee - similar to t$\bar{\text{t}}$CR_OF for ee events outside the Z peak;

t$\bar{\text{t}}$CR_$\mu\mu$ - similar to t$\bar{\text{t}}$CR_OF for $\mu\mu$ events outside the Z peak;

dyCR - for same flavour events inside the Z peak.

In the following, we perform a combined fit of the event yields observed in each category, that is summarized in table 6.7.

6.4.2 BDT-based selection

For the selection using the BDT output, only two regions were defined: a SR, with high BDT output (SR_hBDT), and a background CR, with low BDT output (CR_lBDT). The choice for the cut in the BDT

	SR_ee	SR_mm	SR_em	ttCR_ee	ttCR_mm	ttCR_em	dyCR
inclusive t$\bar{\text{t}}$	300±32	359±37	650±50	61339±73	74513±83	145805±115	54006±93
DY	127±29	144±36	2±2	6044±47	7287±56	289±9	7073193±2740
others	2±1	1±1	1±1	302±2	113±2	105±1	28885±6
total	429±44	504±56	653±50	67685±33	81913±35	146199±42	7156254±2879
exclusive t$\bar{\text{t}}$	21	16	42	155	215	384	170
obs. data	470	598	926	64104	83814	141562	7556951

Table 6.7: Yields for signal and control regions, for different background contributions, for signal and for observed data. The expected yields for signal are normalised to a cross-section of 1 pb. Exactly one track on each side of PPS is required. Only the statistical uncertainty is being represented.

	SR_hBDT	SR_lBDT
inclusive $t\bar{t}$	10785±213	213±56
DY	1138±100	0±5
others	25±3	1±1
total	11947±329	213±11
exclusive $t\bar{t}$	47	38
data obs.	11680	231

Table 6.8: Yields in the signal and control region, for different background contributions, for signal and for observed data, using a cut on the BDT output of 0.2. The expected yields for signal are normalised to a cross-section of 1 pb. Only the statistical uncertainty is being represented.

output was made so that the signal region would have the largest possible signal/$\sqrt{\text{background}}$ ratio ($S/\sqrt{B}$). This ratio in the SR is shown in figure 6.18, as a function of the cut applied to the BDT output.

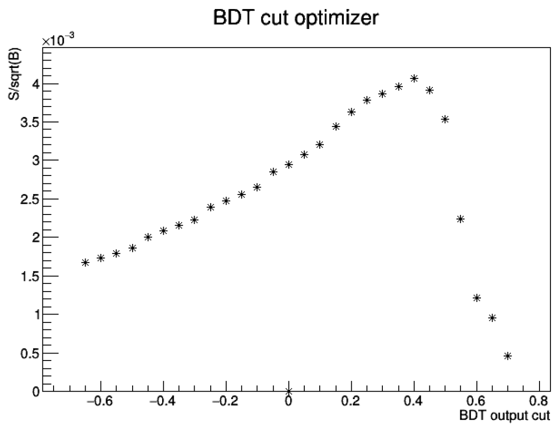

Figure 6.18: Ratio of expected $S/\sqrt{B}$ in the SR as a function of the applied cut in the BDT output. The expected signal yields are normalised to a cross-section of 1 pb.

The best place to apply the cut is where the distribution $S/\sqrt{(B)}$ reaches a maximum, and it corresponds to a BDT output of 0.4. To check if this was an appropriate criterion, several cuts were used to compute the limits, and this showed that the limits are fairly stable with respect to the choice of the BDT cut. The final event categories are as follows:

SR_hBDT - events with 2 leptons and 2 b-jets, with BDT output > 0.4;

CR_lBDT - events with 2 leptons and 2 b-jets, with BDT output < 0.4;

As in the cut-based scenario, a fit is performed combining the event yields observed in each category. The yields in the BDT signal and control region are summarised in table 6.8.

6.4.3 Systematic uncertainties used in the statistical analysis

The summary of the systematic uncertainties considered in the fit is in Tab. 6.9. The uncertainties in the table are based on the CMS recommendations. The uncertainty on the luminosity comes from [55], the uncertainty on the $t\bar{t}$ cross-section is taken from [40]. For the efficiencies in lepton selection, references [56–60] were used.

A fully detailed systematic study would be beneficial for the analysis. Such a study is in progress, and given the nature of the statistically limited analysis, the results are not expected to change dramatically.

Uncertainty	Value	Affects
Luminosity	2.7%	all processes
$\sigma_{\text{inclusive } t\bar{t}}$	5.1%	inclusive $t\bar{t}$ (SR and CR)
σ_{others}	30%	others
DY uncertainty	30%	Drell-Yan
Data-sampling for PPS info.	15%	all except signal and data
Lepton selection efficiency	3%	all processes

Table 6.9: Systematic uncertainties used in the analysis.

Chapter 7

Results

The main result of this thesis is the determination of an upper limit for the cross-section of the exclusive production of top quark pairs. This is done because the cross-section is expected to be small. In fact, what is done is setting two different upper limits, using two separate analysis techniques, one using a simple "cut-and-count" technique and the other using BDTs. In this chapter, these results are presented and discussed. In the last section, a comparison between the two approaches is drawn.

The yields shown in section 6.4, for both methods, are used as an input to the Higgs Combination Tool. First, an asymptotic frequentist limit is computed, in order to get an estimate of the expected limit and observed limits. Then, the expected limits are computed using toy MC events. These are pseudo-data events, generated randomly from the sum of the backgrounds. From the average of these pseudo-data, the method outputs the median and mean limits, together with the 68% and 95% confidence intervals. Finally, the median expected limit is given as input to a Multi-dimensional fit, together with the yields of expected and observed data, and the systematic uncertainties. This method computes $-2*\log$(Likelihood) as a function of a signal strength r, and defines a function, with the minimum in the expected signal strength (corresponding to the cross-section in pb, since the signal is normalised to 1 pb). It also allows us to check if the normalisation factors applied to the dominant backgrounds are the correct ones.

7.1 Statistical analysis - Cut-based approach

By feeding the yields of signal and control regions, together with the systematic uncertainties listed in the previous chapter, to the Higgs Combination Tool, we set an expected limit on the production of $\mathrm{pp} \rightarrow \mathrm{t\bar{t}pp}$ of $\sigma < 1.1$ pb (with a 1σ band of $^{+0.6}_{-0.3}$ pb and a 2σ band of $^{+4.1}_{-0.6}$ pb). The observed limit is 14.5 pb, more than 2 σ from the expected. This seems to occur due to the excess of expected $e\mu$ events in the SR. The origin of such excess is not yet clear and should be further explored.

The likelihood scan for a cross-section scenario of 1.11 pb is shown in figure 7.1 b). For this hypothesis, we expect to measure the signal strength with an associated uncertainty of $^{+1.1}_{-1.1}$ pb @ 95% confidence level. In figure 7.1 a), one can see the contour plot for the scale factors of the two dominant

Nuisance parameter	background-only fit	signal+background fit
DY uncertainty	$+0.40 \pm 0.02$	$+0.38 \pm 0.02$
Selection efficiency	$+0.18 \pm 0.16$	-0.14 ± 0.16
Luminosity	-2.05 ± 0.17	-1.43 ± 0.17
σ other processes	-1.42 ± 0.84	-1.28 ± 0.85
σ inc. $t\bar{t}$	$+0.45 \pm 0.10$	-0.04 ± 0.11

Table 7.1: Post-fit nuisances for background-only and signal+background hypotheses (values not compatible with 0 may indicate inconsistencies in the fit).

backgrounds (DY and QCD $t\bar{t}$), fitted using the dedicated control regions. The minimum is, as expected, at (1,1), showing that the correct factors are being applied.

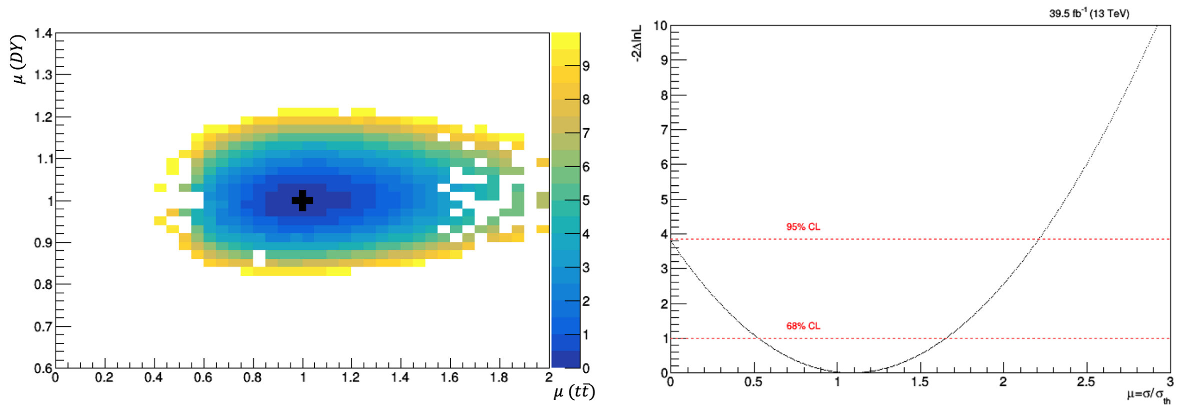

Figure 7.1: (a) Contour of the likelihood for the scale factor for inclusive $t\bar{t}$ and DY processes which are fit using the dedicated control regions. The point marks the fitted values. (b) Likelihood scan results for the signal at expectation level for a $\sigma = 1.1$ pb scenario. The lines intersect the likelihood at the boundaries of the 68% and 95% confidence intervals (CI).

In order to assess the quality of this fit, a method to evaluate the post-fit systematics was used. This method performs a fit to the background-only hypothesis and to the signal+background one. The result is in table 7.1. If everything is according to expectation, the post-fit nuisances should be compatible with 0. This is, however, clearly not the case. Particularly, in the case of two nuisance parameters, the DY production threshold uncertainty and the luminosity. The results seem to be compatible with a lower luminosity than the one that was introduced. This can indicate some problems with the DY simulated samples, for example mean that the cross-section value which was used to normalise the DY production is not the most correct one.

To check that this was the correct interpretation, we tried running the Higgs Combination Tool, not including the DY control region in the fit. The fit diagnostics was performed again and the hypothesis was confirmed (see table 7.2). The discrepancy in luminosity was eliminated and the DY uncertainty is increased, showing that the fit is compatible with a higher DY cross-section, which shows that the DY cross-section is probably underestimated.

The analysis excluding the DY CR resulted in an observed upper limit of 7.2 pb, and a median expected limit of $\sigma < 1.1^{+0.5}_{-0.3}$ pb (@ 68% confidence level), or $1.1^{+1.1}_{-0.5}$ pb (@ 95% confidence level). This result is fully compatible with the previously obtained result. The plots obtained without the DY control region are shown in figure 7.2. The likelihood scan was performed for a cross-section scenario of 1.1

Nuisance parameter	background-only fit	signal+background fit
DY uncertainty	$+0.79 \pm 0.15$	$+0.62 \pm 0.16$
Selection efficiency	-0.26 ± 0.88	-0.39 ± 0.88
Luminosity	-0.31 ± 0.90	-0.41 ± 0.90
σ other processes	-1.61 ± 0.83	-1.40 ± 0.85
σ inc. $t\bar{t}$	-0.31 ± 0.62	-0.49 ± 0.62

Table 7.2: Post-fit nuisances for background-only and signal+background hypotheses, excluding the DY control region (values not com-patible with 0 may indicate inconsistencies in the fit).

pb, and in this hypothesis, we expect to measure the signal strength with associated uncertainties $^{+1.2}_{-1.1}$ pb, @ 95% confidence level.

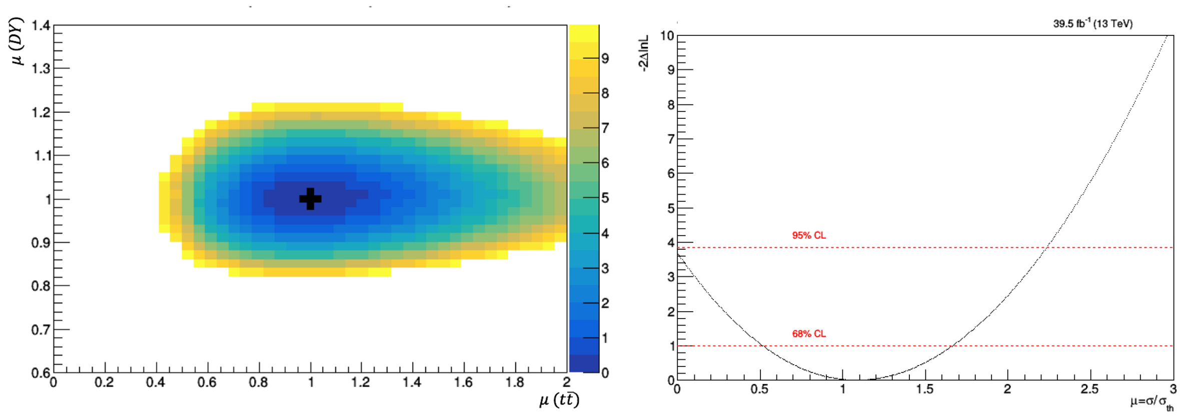

Figure 7.2: (a) Contour of the likelihood for the scale factor for inclusive $t\bar{t}$ and DY processes. The point marks the fitted values. (b) Likelihood scan results for the signal at expectation level for a $\sigma = 1.1$ pb scenario, excluding the DY control region. The lines intersect the likelihood at the boundaries of the 68% and 95% CI.

7.2 Statistical analysis - BDT approach

As for the BDT approach, the same procedure was used, but now with the BDT signal and control regions. The observed upper limit is 1.4 pb, and the median expected limit $\sigma < 0.8$ pb (with 1σ band of $^{+0.4}_{-0.2}$ pb and a 2σ band of $0.8^{+0.7}_{-0.4}$ pb). The observed limit is within 2σ from the expected. The likelihood scan for a cross-section scenario of 0.9 pb is shown in figure 7.3 b). For this scenario, the measurement of signal strength is expected to be made with uncertainties $^{+0.9}_{-0.9}$ pb, @ 95% confidence level. In figure 7.3 a), one can see the contour plot for the scale factors of the two dominant backgrounds (DY and QCD $t\bar{t}$), fitted using the dedicated control regions. The minimum is, as expected, at (1,1), that is, the ratio to the expected value is 1 for both backgrounds, which means that the correct normalisation factors are being applied.

7.3 Comparison between methods and discussion

Since it is designed to apply optimal cuts in several variables, it is expected that the BDT is more sensitive with respect to a simple cut-based selection. In fact, this seems to be the case when looking

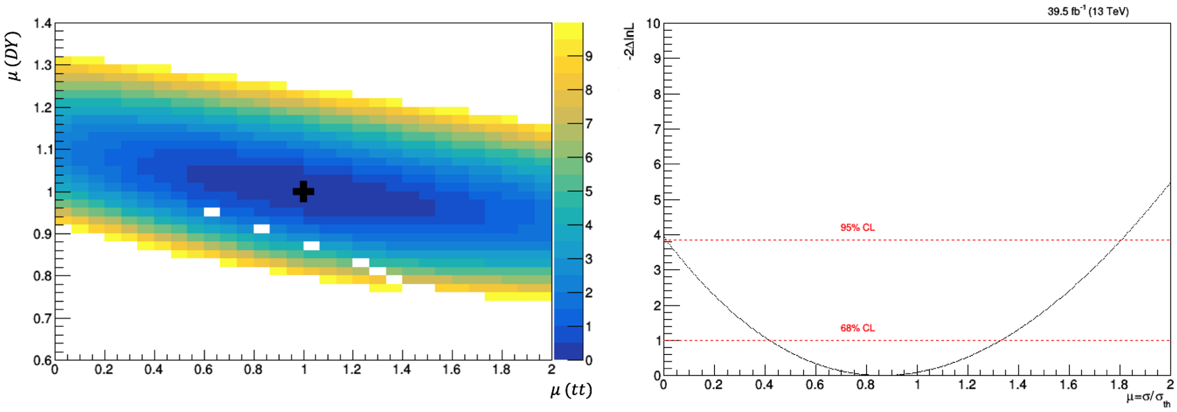

Figure 7.3: (a) Contour of the likelihood for the scale factor for inclusive $t\bar{t}$ and DY processes. The point marks the fitted values. (b) Likelihood scan results for the signal at expectation level for a $\sigma = 0.8$ pb scenario, excluding the DY control region. The line intersects the likelihood at the boundaries of the 68% CI.

at the results. Although they are not strikingly different, and the 95% confidence bands strongly overlap, one can see that the median limit set using the BDT is about 20% lower than the one obtained with the classical approach. Moreover, the uncertainties are significantly reduced, thus validating the usefulness of this MVA technique.

For this last approach, the observed limit is within the expected. However, that is not true for the cut-and-count method, as noted before. A deviation higher than 2σ is statistically possible, and it might be the case that the observed deviations are merely a statistical effect. It can also happen that there are relevant sources of systematic uncertainty that were not taken into account in this analysis. Namely, there are uncertainties which will affect the variable distributions differentially, thus changing their shape and the fits. For example, for QCD $t\bar{t}$, an uncertainty study is performed in [61], where a measurement of $M_{t\bar{t}}$ is performed in the dilepton channel. $M_{t\bar{t}}$ is an important variable in our analysis, particularly in the BDT approach. The article shows that the uncertainties on this variable affect the measurement differentially on the $M_{t\bar{t}}$ spectrum, as is illustrated in the plot of figure 7.4.

It would, therefore, certainly be worth it to look in more detail into the various sources of systematic uncertainty, in the future. Some of the main uncertainties are related to jet energy scale, imperfect modelling of lepton identification, b-tagging efficiency, and theoretical sources related to the precision with which events are generated.

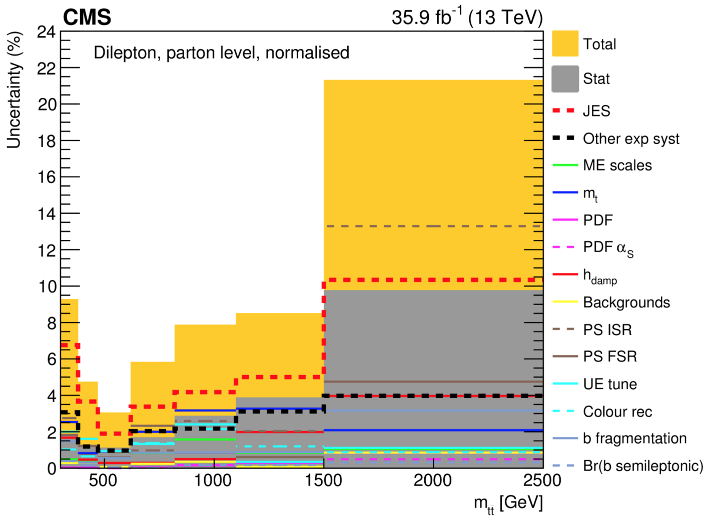

Figure 7.4: Statistical and systematic uncertainties in the measurement of $M_{t\bar{t}}$, from [61], as a function of the value of $M_{t\bar{t}}$.

Chapter 8

Conclusions

8.1 Achievements

The goal of the work behind this master thesis was to develop an analysis to search for exclusive production of top quark pairs. This was successfully achieved. A set of selection criteria was developed, based on the exclusive dilepton search, as well as the existing $\mathrm{t\bar{t}}$ analyses and measurements.

The performance of the PPS detector was studied, and its acceptance and fake ratio were computed using data and simulated signal samples. Furthermore, the selection using both CMS central and PPS forward information was optimised. Correlations between the central and forward kinematics were established for signal simulation. An existing algorithm to reconstruct $\mathrm{t\bar{t}}$ kinematics in the dilepton decay channel was used, and a regression technique was used to improve its resolution by $\sim$ 20%.

A BDT classifier was built by using the central and forward kinematic variables, in order to efficiently separate signal from background.

Using statistical concepts and a fitting software, I was able to estimate two upper limits for the cross-section of the exclusive $\mathrm{t\bar{t}}$ production, one based on a simple event selection (expected $\sigma < 1.1^{+1.1}_{-0.5}$ pb @ 95% confidence level, observed 14.5 pb), and the other on a BDT classifier output (expected $\sigma < 0.9^{+0.7}_{-0.4}$ fb @ 95% confidence level, observed 1.4 pb). I compared the two and verified that the BDT approach brings approximately 20% improvement, with respect to the classical approach, thus showing the power of multivariate analysis techniques in high-energy physics.

These limits represent the first experimental result on this particular search and may allow the comparison with existing theoretical predictions, which was not possible until now. Furthermore, it is the first upper limit measurement using PPS information. This result has been also documented in an internal CMS analysis note with the goal of completing the analysis towards publication.

8.2 Future Work

Despite the mentioned achievements, there is still a long way to go in this analysis. First of all, it would be important to study whether or not the LHC, with the full statistics that will be available in the next few years, is expected to have sensitivity to this process. This, of course, depends on the existence of anomalous couplings between the top quark and the photon. An interesting future work would be to perform phenomenological studies in order to estimate the sensitivity of this process to such anomalous couplings.

Apart from that, and on the experimental side, improvements could be made to the analysis strategy. The main difficulty of this analysis is the existence of an overwhelming background, caused by pileup. Several ways to circumvent this problem can be studied. One of them is by trying different cutoffs on the PPS track multiplicity. When several tracks are considered, the systematic error committed in the track association must be studied. Another possible improvement could be achieved by running the analysis on data collected in low pileup environment - there are some LHC runs where the average number of vertices is significantly smaller, thus necessarily reducing the number of PPS tracks, without the need to introduce a cutoff. The use of PPS timing information may also be critical to reduce this combinatorial background.

In the future, as more data will be available with updated proton reconstruction recipes, it will also be interesting to include all the available data in the analysis, in order to increase the statistics and, as a consequence, the sensitivity to the signal process. It would also be essential to generate a larger sample of simulated signal events, which would allow for better training of MVA classifiers, and would allow the use of different types of classifiers.

Another crucial point would be to study and include in the analysis a number of uncertainties that are not currently being considered, as discussed in the Results section. For inclusive $t\bar{t}$, it would be interesting to test different effects such as radiation scales, factorisation/renormalisation, underlying event, etc.; and other experimental effects such as the uncertainties on jet energy resolution and scale and ξ resolution and scale.

Another possible approach for improving the separation between signal and background would be to resort to more sophisticated MVA techniques. A LIP colleague, the PhD student Giles Strong, has developed a package that allows the application of Deep Neural Networks (DNN) to high-energy physics analyses. Using this package, called *lumin* [62], is an option to consider in the future.

Bibliography

[1] ATLAS collaboration. "Observation of a new particle in the search for the Standard Model Higgs boson with the ATLAS detector at the LHC". *Phys. Lett. B*, 716:1–29, 2012. doi: 10.1016/j.physletb.2012.08.020.

[2] CMS collaboration. "Observation of a new boson at a mass of 125 GeV with the CMS experiment at the LHC". *Phys. Lett. B*, 716:30–61, 2012. doi: 10.1016/j.physletb.2012.08.021.

[3] CDF collaboration. "Observation of top quark production in $\bar{p}p$ collisions". *Phys. Rev. Lett.*, 74:2626–2631, 1995. doi: 10.1103/PhysRevLett.74.2626.

[4] M. Tanabashi et al. (Particle Data Group). "Review of Particle Physics". *Phys. Rev. D*, 98(3):030001, 2018. doi: 10.1103/PhysRevD.98.030001.

[5] S. Fayazbakhsh, S. T. Monfared, and M. Mohammadi Najafabadi. "Top Quark Anomalous Electromagnetic Couplings in Photon-Photon Scattering at the LHC". *Phys. Rev. D*, 92(1):014006, 2015. doi: 10.1103/PhysRevD.92.014006.

[6] L. A. Harland-Lang, V. A. Khoze, and M. G. Ryskin. "Exclusive LHC physics with heavy ions: SuperChic 3". *Eur. Phys. J. C Part. Fields.*, 79(1):39, 2018. doi: 10.1140/epjc/s10052-018-6530-5.

[7] J. de Favereau de Jeneret, V. Lemaitre, Y. Liu, S. Ovyn, T. Pierzchala, K. Piotrzkowski, X. Rouby, N. Schul, and M. Vander Donckt. "High energy photon interactions at the LHC". *arXiv 0908.2020*, 2009.

[8] M. Luszczak, L. Forthomme, W. Schäfer, and A. Szczurek. "Production of $t\bar{t}$ pairs via $\gamma\gamma$ fusion with photon transverse momenta and proton dissociation". *arXiv 1810.12432*, 2018.

[9] P. Bussey, T. Coughlin, J. Forshaw, and A. Pilkington. "Central exclusive production of longlived gluinos at the LHC". *JHEP*, 11:027, 2006. doi: 10.1088/1126-6708/2006/11/027.

[10] S. Heinemeyer, V. Khoze, M. Ryskin, M. Tasevsky, and G. Weiglein. "Central Exclusive Production of BSM Higgs bosons at the LHC". In *Proceedings, 38th International Symposium on Multiparticle Dynamics (ISMD 2008): Hamburg, Germany, September 15-20, 2008*, pages 338–343, 2009. doi: 10.3204/DESY-PROC-2009-01/60.

[11] S. Taheri Monfared and S. Fayazbakhsh. "Probing Anomalous Top Quark Couplings in Diffractive Events at the LHC". *Acta Phys. Polon. Supp.*, 7(3):579, 2014. doi: 10.5506/APhysPolBSupp.7.579.

[12] K. Piotrzkowski and N. Schul. ”Two-photon exclusive production of supersymmetric pairs at the LHC”. *AIP Conf. Proc.*, 1200:434–437, 2010. doi: 10.1063/1.3327609.

[13] M. Thomson. *Modern Particle Physics*. 1st edition, 2013.

[14] A. O. Bouzas and F. Larios. ”Top quark electromagnetic dipole moments”. *J. Phys. Conf. Ser.*, 651 (1):012014, 2015. doi: 10.1088/1742-6596/651/1/012014.

[15] Facts and figures about the LHC. URL `https://home.cern/resources/faqs/facts-and-figures-about-lhc.` , accessed on August 29th, 2019.

[16] T. Petterson, T. Sven and P. Lefèvre (LHC Study Group). ”The Large Hadron Collider: Conceptual design”. 1995.

[17] ATLAS collaboration. ”The ATLAS Experiment at the CERN Large Hadron Collider”. *JINST*, 3: S08003, 2008. doi: 10.1088/1748-0221/3/08/S08003.

[18] LHCb collaboration. ”LHCb technical proposal”. 1998.

[19] ALICE collaboration. ”The ALICE experiment at the CERN LHC”. *JINST*, 3:S08002, 2008. doi: 10.1088/1748-0221/3/08/S08002.

[20] High-Luminosity LHC Project Schedule. URL `https://project-hl-lhc-industry.web.cern.ch/content/project-schedule.` , accessed on September 9th, 2019.

[21] CMS collaboration. ”The CMS experiment at the CERN LHC”. *JINST 3*, 2008. doi: 10.1088/1748-0221/3/08/S08004.

[22] Cern Document Server: CMS slice image view. URL `http://cds.cern.ch/record/2204863.` , accessed on August 29th, 2019.

[23] CMS collaboration. Identification of heavy-flavour jets with the CMS detector in pp collisions at 13 TeV. *JINST*, 13(05):P05011, 2018. doi: 10.1088/1748-0221/13/05/P05011.

[24] CMS collaboration. ”The Performance of the CMS Muon Detector in Proton-Proton Collisions at $\sqrt{s}$ = 7 TeV at the LHC”. *JINST*, 8:P11002, 2013. doi: 10.1088/1748-0221/8/11/P11002.

[25] CMS and TOTEM collaborations. ”CMS-TOTEM Precision Proton Spectrometer”. 2014.

[26] F. Ravera. ”3D silicon pixel detectors for the CT-PPS tracking system”, 2017. URL `http://cds.cern.ch/record/2682003`. PhD Thesis, Presented 16 Jun 2017.

[27] TOTEM collaboration. ”Performance of the TOTEM Detectors at the LHC”. *Int. J. Mod. Phys.*, A28: 1330046, 2013. doi: 10.1142/S0217751X13300469.

[28] M. Deile, F. Caspers, T. Kroyer, M. Oriunno, E. Radermacher, A. Soter, and F. Roncarolo. ”Beam Coupling Impedance Measurement and Mitigation for a TOTEM Roman Pot”. *Conf. Proc.*, C0806233:TUPP029, 2008. arXiv:0806.4974.

[29] CMS and TOTEM PPS collaboration. "Efficiency of Si-strips sensors used in Precision Proton Spectrometer". Technical Report CMS DP-2018/056, 2018.

[30] CMS and TOTEM collaborations. "CTPPS plots: 2017 performance update and 2018 start of data taking". Technical Report CMS DP-2018/021, 2018.

[31] F. Nemes. "LHC optics determination with proton tracks measured in the CT-PPS detectors in 2016, before TS2". Technical report, 2017.

[32] CMS collaboration. "First Measurement of the Cross Section for Top-Quark Pair Production in Proton-Proton Collisions at $\sqrt{s} = 7$ TeV". *Phys. Lett.*, B695:424–443, 2011. doi: 10.1016/j.physletb.2010.11.058.

[33] CMS collaboration. "Measurement of the $t\bar{t}$ production cross section, the top quark mass, and the strong coupling constant using dilepton events in pp collisions at $\sqrt{s} = 13$ TeV". *Eur. Phys. J. C*, 79: 368, 2018.

[34] M. Czakon, P. Fiedler, and A. Mitov. Total Top-Quark Pair-Production Cross Section at Hadron Colliders Through $O(\frac{4}{S})$. *Phys. Rev. Lett.*, 110:252004, 2013. doi: 10.1103/PhysRevLett.110.252004.

[35] CMS and TOTEM collaborations. "Observation of proton-tagged, central (semi)exclusive production of high-mass lepton pairs in pp collisions at 13 TeV with the CMS-TOTEM precision proton spectrometer". *JHEP*, 07:153, 2018. doi: 10.1007/JHEP07(2018)153.

[36] J. Kaspar. "Alignment of CT-PPS detectors in 2016, before TS2". Technical report, 2017.

[37] J. Alwall et al. "The automated computation of tree-level and next-to-leading order differential cross sections, and their matching to parton shower simulations". *JHEP*, 07:079, 2014. doi: 10.1007/JHEP07(2014)079.

[38] C. Oleari. "The POWHEG-BOX". *Nucl. Phys. Proc. Suppl.*, 205-206:36–41, 2010. doi: 10.1016/j.nuclphysbps.2010.08.016.

[39] Sjöstrand, Torbjörn et al. "an introduction to pythia 8.2". *Computer physics communications*, 191: 159–177, 2015.

[40] ATLAS and CMS collaborations. "NNLO+NNLL top-quark-pair cross sections". twiki, 2019. URL `https://twiki.cern.ch/twiki/bin/view/LHCPhysics/TtbarNNLO#Introduction`.

[41] M. Czakon and A. Mitov. "Top++: A Program for the Calculation of the Top-Pair Cross-Section at Hadron Colliders". *Comput. Phys. Commun.*, 185:2930, 2014. doi: 10.1016/j.cpc.2014.06.021.

[42] N. Kidonakis. Two-loop soft anomalous dimensions for single top quark associated production with a W- or H-. *Phys. Rev.*, D82:054018, 2010. doi: 10.1103/PhysRevD.82.054018.

[43] H. Y.-S. T. Tomislav Seva. "Standard Model Cross Sections for CMS at 13 TeV". twiki, 2019. URL `https://twiki.cern.ch/twiki/bin/viewauth/CMS/StandardModelCrossSectionsat13TeV`.

[44] M. Boonekamp, A. Dechambre, V. Juranek, O. Kepka, M. Rangel, C. Royon, and R. Staszewski. ”FPMC: A Generator for forward physics”. *arXiv 1102.2531*, 2011.

[45] M. Bahr et al. ”Herwig++ Physics and Manual”. *Eur. Phys. J. C*, 58:639–707, 2008. doi: 10.1140/epjc/s10052-008-0798-9.

[46] A. Manohar, P. Nason, G. P. Salam, and G. Zanderighi. ”How bright is the proton? A precise determination of the photon parton distribution function”. *Phys. Rev. Lett.*, 117(24):242002, 2016. doi: 10.1103/PhysRevLett.117.242002.

[47] A. Hoecker et al. ”TMVA - Toolkit for Multivariate Data Analysis”, 2007.

[48] ”Procedure for the LHC Higgs boson search combination in Summer 2011”. Technical Report CMS-NOTE-2011-005. ATL-PHYS-PUB-2011-11, 2011. URL https://cds.cern.ch/record/1379837.

[49] G. Cowan, K. Cranmer, E. Gross, and O. Vitells. ”Asymptotic formulae for likelihood-based tests of new physics”. *Eur. Phys. J.*, C71:1554, 2011. doi: 10.1140/epjc/s10052-011-1554-0,10.1140/epjc/s10052-013-2501-z. [Erratum: Eur. Phys. J.C73,2501(2013)].

[50] A. Hinzmann et al. (JME group). ”Jet identification in high pile-up environment”. twiki, 2017. URL https://twiki.cern.ch/twiki/bin/view/CMS/PileupJetID.

[51] CMS collaboration. ”Identification of heavy-flavour jets with the CMS detector in pp collisions at 13 TeV”. *JINST*, 13(05):P05011, 2018. doi: 10.1088/1748-0221/13/05/P05011.

[52] D. Bertolini, P. Harris, M. Low, and N. Tran. ”Pileup Per Particle Identification”. *JHEP*, 10:059, 2014. doi: 10.1007/JHEP10(2014)059.

[53] CMS collaboration. ”Performance of missing transverse momentum in pp collisions at $\sqrt{s} = 13$ TeV using the CMS detector”. Technical Report CMS-PAS-JME-17-001, 2018. URL http://cds.cern.ch/record/2628600.

[54] B. A. Betchart, R. Demina, and A. Harel. ”Analytic solutions for neutrino momenta in decay of top quarks”. *Nuclear Instruments and Methods in Physics Research A*, 736:169–178, 2013. doi: 10.1016/j.nima.2013.10.039.

[55] CMS Collaboration. ”CMS luminosity measurement for the 2017 data-taking period at $\sqrt{s} = 13$ TeV”. 2018.

[56] CMS Collaboration. ”Muon identification and isolation efficiencies with 2017 and 2018 data”. 2018. URL https://cds.cern.ch/record/2629364.

[57] CMS Collaboration. ”Muon Tracking Efficiency using Tag and Probe method for 2017 dataset”. 2019. URL https://cds.cern.ch/record/2666648.

[58] CMS Collaboration. ”Electron and Photon performance in CMS with the full 2017 data sample and additional 2016 highlights for the CALOR 2018 Conference”. May 2018. URL https://cds.cern.ch/record/2320638.

[59] CMS Collaboration. ”Electron trigger performance in CMS with the full 2017 data sample.”. 2018. URL https://cds.cern.ch/record/2626028.

[60] CMS Collaboration. ”Electron and Photon performance in CMS with the data sample collected in 2016-17-18 at 13 TeV for the ICHEP 2018 Conference”. 2018. URL https://cds.cern.ch/record/2629363.

[61] CMS collaboration. ”Measurements of $t\bar{t}$ differential cross sections in proton-proton collisions at $\sqrt{s}$ = 13 TeV using events containing two leptons”. *JHEP*, 02:149, 2019. doi: 10.1007/JHEP02(2019)149.

[62] G. C. Strong. ”LUMIN”. 2019. doi: 10.5281/zenodo.2601857. available on https://github.com/GilesStrong/lumin/.

Appendix A

List of triggers used in the analysis

Table A.1 summarises the high-level triggers that were applied, for the purpose of this analysis, to the data collected by the CMS detector in 2017. As explained in the text, only events with at least two reconstructed leptons (electrons and/or muons) satisfying these characteristics were considered. These triggers select leptons above a certain transverse momentum threshold and properly isolated from other reconstructed particles in the collision.

	Trigger name
Electron trigger	HLT_Ele35_WPTight_Gsf_v
Muon triggers	HLT_IsoMu24_v HLT_IsoMu24_2p1_v HLT_IsoMu27_v
2 Muon triggers	HLT_Mu17_TrkIsoVVL_Mu8_TrkIsoVVL_DZ HLT_Mu17_TrkIsoVVL_Mu8_TrkIsoVVL_DZ_Mass8_v HLT_Mu17_TrkIsoVVL_Mu8_TrkIsoVVL_DZ_Mass3p8_v
2 Electron triggers	HLT_Ele23_Ele12_CaloIdL_TrackIdL_IsoVL_v HLT_Ele23_Ele12_CaloIdL_TrackIdL_IsoVL_DZ_v
Electron-muon triggers	HLT_Mu23_TrkIsoVVL_Ele12_CaloIdL_TrackIdL_IsoVL_v HLT_Mu23_TrkIsoVVL_Ele12_CaloIdL_TrackIdL_IsoVL_DZ_v HLT_Mu12_TrkIsoVVL_Ele23_CaloIdL_TrackIdL_IsoVL_v HLT_Mu12_TrkIsoVVL_Ele23_CaloIdL_TrackIdL_IsoVL_DZ_v HLT_Mu8_TrkIsoVVL_Ele23_CaloIdL_TrackIdL_IsoVL_v HLT_Mu8_TrkIsoVVL_Ele23_CaloIdL_TrackIdL_IsoVL_DZ_v

Table A.1: Triggers used in the selection of the events.

Appendix B

Extra plots

In this appendix, some extra kinematic distributions are shown. The distributions in figures B.1 and B.1 are all obtained for the $e\mu$ channel, after selecting 2 leptons, at least one b-tagged jet and $M_{lb} < 160$ GeV. In figure B.1 (left) one can see the multiplicity of light jets. For the signal, this number is expected to be lower than for the $\mathrm{t\bar{t}}$ background, as lower extra activity in the event is expected, as explained in the text. In figure B.1 (right), the missing transverse energy is shown. The distributions have similar shape for the signal and for the $\mathrm{t\bar{t}}$backgrounds, due to the presence of 2 neutrinos. For the other backgrounds, however, lower missing transverse energy is expected. In figure B.1, the M_{lb} variable is shown. For all these distributions, a good data/MC agreement is found.

Figure B.3 shows the shape of the 13 most discriminating variables which were chosen for training the BDTs, for the signal and for the $\mathrm{t\bar{t}}$ background. The differences in the shapes were used to train the classifier. Variables labelled 1 and 2 are related to the information from the forward detector (PPS), therefore it is expected to be random (shaped by the acceptance) for the background, and corresponding to the invariant mass and rapidity of the $\mathrm{t\bar{t}}$ for the signal. The variable number 3, the $M_{\mathrm{t\bar{t}}}$ after applying the regression technique discussed in chapter 6, is expected to be higher for the signal (completely back-to-back tops, no extra activity in the event) than for the background. Similar arguments can be used to explain the different distributions for the remaining variables. Some kinematic variables (e.g. ϕ and η of the second most energetic b-tagged jet) were chosen simply because they maximised the performance of the classifier, with no further physics motivation.

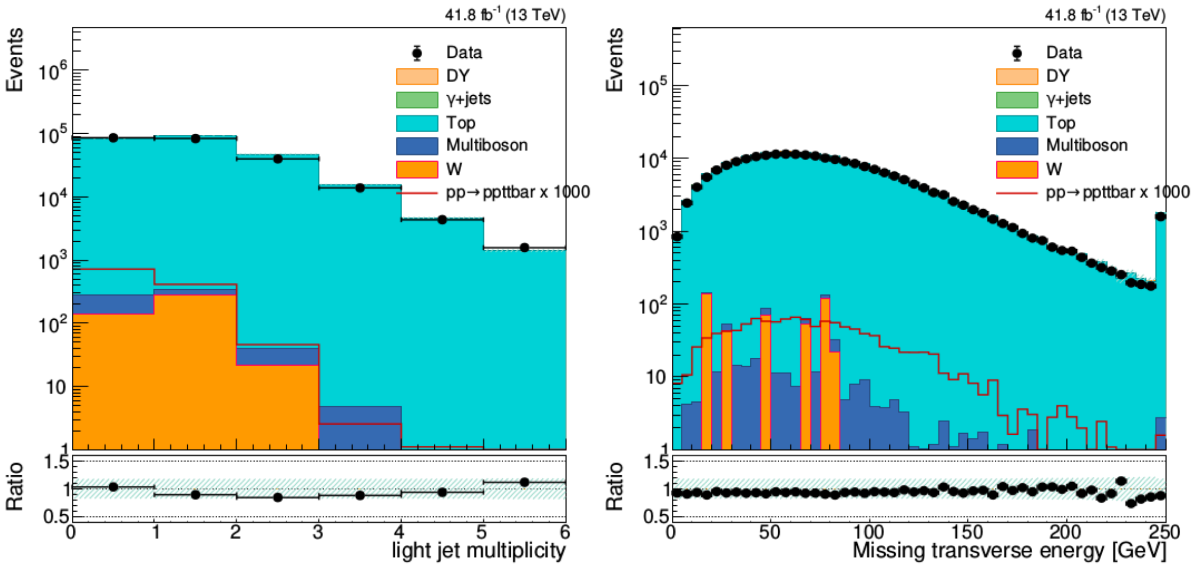

Figure B.1: Distribution of the number of light (not b-tagged) jets (left) and the missing transverse energy (right), after selecting 2 leptons and ≥1 b and requiring $M_{lb} < 160$ GeV, for the $e\mu$ channel.

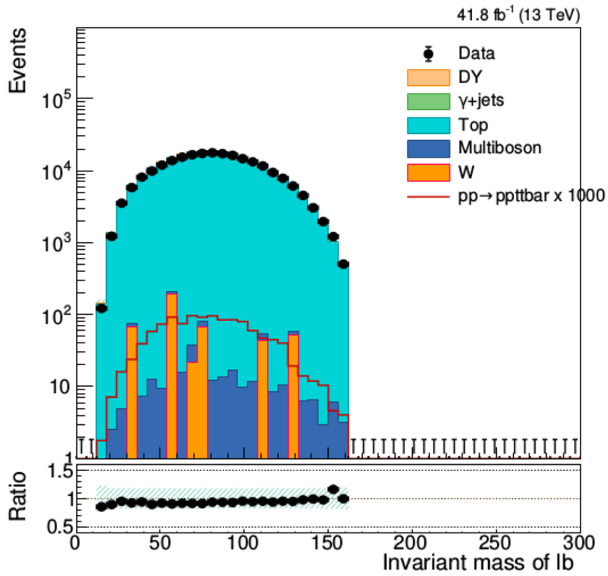

Figure B.2: Distribution of the M_{lb} (mass of one of the lepton b-jet associations), after selecting 2 leptons and ≥1 b and requiring $M_{lb} < 160$ GeV, for the $e\mu$ channel.

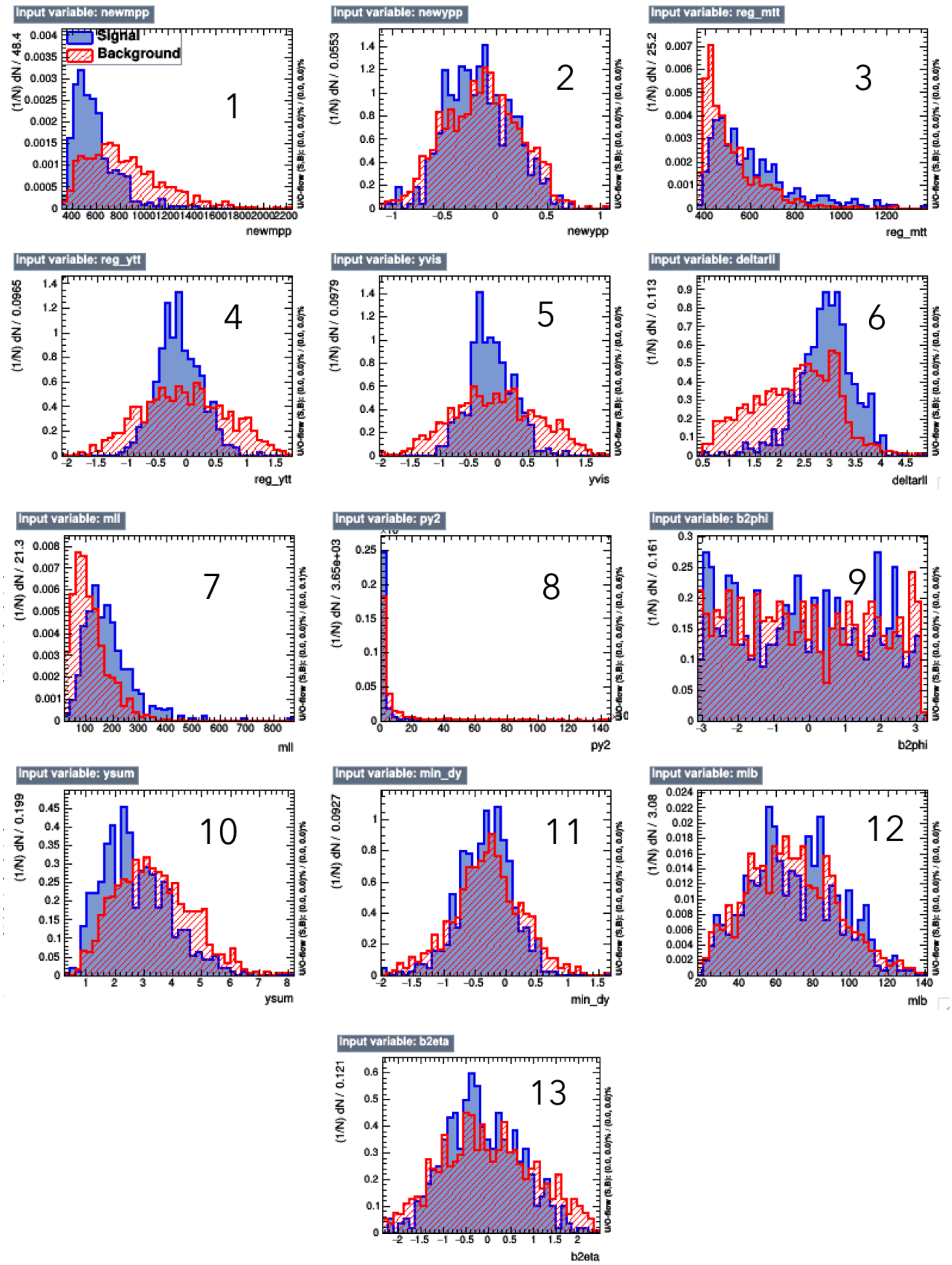

Figure B.3: Distributions for signal (blue) and background (red), of the 13 variables which were found to most discriminating between signal and inclusive $t\bar{t}$ background, for the training sample used in the BDT classifier.

Appendix C

PPS optical corrections

A set of *a posteriori* optical corrections were applied to the data and the simulated signal samples, to account for the most up-to-date proton reconstruction recipe. Figure shows the proton fractional momentum loss (ξ) before applying the corrections as a function of the xi after applying the corrections. On the left, this is shown for arm 45 of CMS, and on the right, for arm 56. The different colors represent the 4 different LHC crossing angles. It is evident from the figures that the correction factors move the results towards lower xi values.

Figure C.2 shows the distribution of M_{RP} obtained before and after applying the corrections. It shows that after applying the corrections, we increase the acceptance in the $300 < M_{RP} < 600$ GeV region by ~60%.

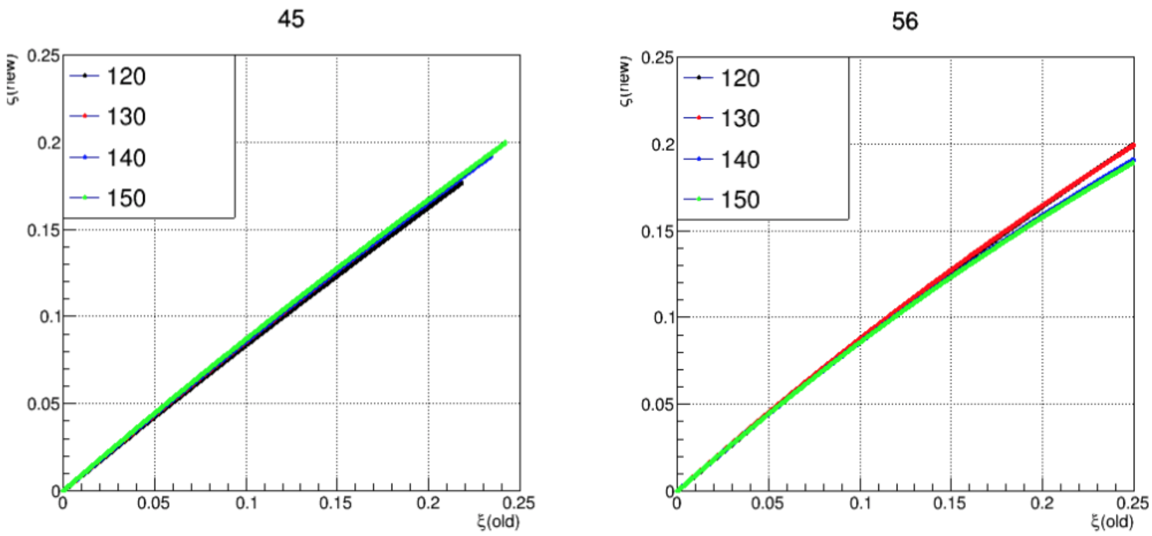

Figure C.1: Plots showing the difference between the ξ values before and after applying the most recent optical corrections, for the different lHC crossing angles considered. ”45” refers to LHC sector 45, or the negative arm as it is described in this thesis, while ”56” refers to sector 56 or the positive arm.

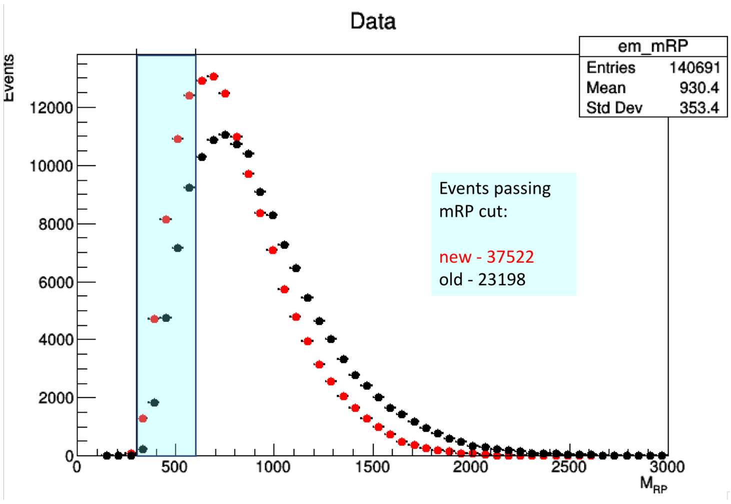

Figure C.2: Distribution of the pp mass as reconstructed from PPS tracks, in data, before (black) and after (red) applying the optical corrections. The light blue area shows the exclusive $t\bar{t}$ region chosen for the analysis. It is visible that the number of events within this region is increased by 60% when moving to the new alignments. This is a large difference, and that is why the whole analysis was rerun to include the corrections.